2012-05-03

An Experimental Study of All-Solid-State Mediator Supercapacitor and Fundamental Study of Interfaces in Polymer Electrolyte Fuel Cell

Juanjuan Zhou
University of Miami, j.zhou9@umiami.edu

UNIVERSITY OF MIAMI

AN EXPERIMENTAL STUDY OF ALL-SOLID-STATE MEDIATOR SUPERCAPACITOR AND FUNDAMENTAL STUDY OF INTERFACES IN POLYMER ELECTROLYTE FUEL CELL

By

Juanjuan Zhou

A DISSERTATION

Submitted to the Faculty
of the University of Miami
in partial fulfillment of the requirements for
the degree of Doctor of Philosophy

Coral Gables, Florida

May 2012

UNIVERSITY OF MIAMI

A dissertation submitted in partial fulfillment of
the requirements for the degree of
Doctor of Philosophy

AN EXPERIMENTAL STUDY OF ALL-SOLID-STATE MEDIATOR SUPERCAPACITOR AND FUNDAMENTAL STUDY OF INTERFACES IN POLYMER ELECTROLYTE FUEL CELL

Juanjuan Zhou

Approved:

_____ Xiangyang Zhou, Ph.D. Associate Professor of Mechanical and Engineering	_____ Terri A. Scandura, Ph.D. Dean of the Graduate School
_____ Hongtan Liu, Ph.D. Professor of Mechanical and Aerospace Engineering	_____ Na Li, Ph.D. Assistant Professor of Mechanical and Aerospace Engineering
_____ Weiyong Gu, Ph.D. Professor of Biomedical Engineering	_____ Chengzhong Li, Ph.D. Associate Professor of Biomedical Engineering at Florida International University

ZHOU, JUANJUAN (Ph.D., Mechanical and Aerospace Engineering)

An Experimental Study of All-Solid-State Mediator Supercapacitor and Fundamental Study of Interfaces in Polymer Electrolyte Fuel Cell (May 2012)

Abstract of a dissertation at the University of Miami.

Dissertation supervised by Professor Xiangyang Zhou.
No. of pages in text. (190)

The present PhD dissertation reflects research efforts on two different topics: 1) development and study of all-solid-state mediator supercapacitors (SCs) and 2) atomistic modeling and scanning tunneling microscopy (STM) study of interfaces in Nafion based polymer electrolyte fuel cells (PEFCs).

The present research on all-solid-state mediator SCs was focused on two systems: 1) NaI/I_2 mediators, poly(ethylene oxide)/$LiClO_4$ electrolyte, and Nafion separator; and 2) NaI/I_2 or $K_3Fe(CN)_6/K_4Fe(CN)_6$ mediators, poly(ethylene oxide)/$LiClO_4$ electrolyte, and polyvinylidene fluoride (PVDF)/lithium trifluoromethanesulfonate (LiTFS) separator. The results for the Nafion based mediator SCs are as follows.

The cyclic voltammetry results showed that the specific capacitance of the SCs without and with redox mediators were 45 and 210 F g^{-1} within a voltage window of 0.0-1.0 V and at the scanning rate of 25 mV s^{-1}, respectively, showing a significant enhancement effect for the mediators. The *in situ* XAS measurements indicate that the reversible redox states during charge/discharge process are I_2 (oxidation) and I_3^- (reduction).

PVDF/LiTFS membrane was prepared to replace the Nafion membrane as the separator. With the application of the water-free membrane, the specific energy increased from 20.8 to 49.1 Wh kg^{-1} within the range of specific energy for batteries. In addition, it

was found that the performance of the NaI/I_2 mediator SC increased when the mediator concentration increased from 5% to 20%, but decreased slightly when increased from 20% to 30%. This is considered to be a very important characteristic of the mediator SC in contrast to all other types of SCs that can be utilized for their optimization.

In the second part of this dissertation, both theoretical modeling and STM imaging were employed to investigate the structure and the properties of the electrode/electrolyte interfaces. In the theoretical study part, an approach of hybrid atomistic simulation was adopted. First, molecular dynamics show that an ordered contact layer is formed on $Pt/(H_2O+H_3O^+)$ and Pt/H_2SO_4 interface. However, the Pt/Nafion interface is partially ordered. Secondly, *ab initio* simulation can visualize bond formation and breakdown, representing charge transfer at interface. Thirdly, quantum statistical calculations correctly predict the trends of the electrochemical current density.

In the STM imaging study, Nafion film with a thickness of several hundred nanometers was deposited on highly oriented pyrolytic graphite (HOPG) pieces and polycrystalline platinum sheets. STM images indicated that the interface structures resembled to, but were larger than, the surface structures of the blank substrates. Results showed that the ordering structures of the HOPG/Nafion interface were destroyed right after the applied potential was changed, and a new type of ordering was generated. The existing electron tunneling phenomenon theory cannot be used to explain the experiment results. Therefore, a new theory based on principles of quantum mechanics and solid-state physics was developed.

ACKNOWLEDGEMENT

Although only my name is on the cover of this dissertation, this dissertation would never be accomplished without the contribution of a great number of people.

First and foremost I extend my deepest and sincerest gratitude to my supervisor, Dr. Xiangyang Zhou, who has supported me throughout this thesis. Dr. Zhou introduced me to the mysterious material world with his knowledge, passion, and patience. Without his help, time, guidance, my experience over these years would not have been so amazing and productive.

I am very grateful to Dr. Hongtan Liu, one of my Ph.D. committee members, for all the lively discussions and constructive feedback about my research during the group meetings. I would also like to acknowledge Dr. Na Li, Dr. Chengzhong Li, and Dr. Weiyong Gu for their participation as committee members and dedication and invaluable comments about this thesis.

I came to understand the concept of "team spirit" with the help and company of the entire group: Dr. Yijing Yin, Dr. Zedong Wang, Hao Huang, Jinshu Cai, Sirui Cai, and Xuyang Zhang. They are not only colleagues, but also good friends I will keep for a lifetime.

Outside the laboratory in University of Miami, I extend many special thanks to Dr. Azzam N. Mansour from the Naval Research Center at Carderock Division, who conducted the *in situ* X-ray absorption spectroscopy measurements, and Dr. Dwyane

McDaniel from Florida International University, who provided access to scanning tunneling microscopy instruments. Their support brought this research to a new level.

Last but not least, I would like to thank my parents for all their support and encouragement; without them I couldn't have come this far. I owe everything to the most loving and loved person in the world: My husband Chen Zhang. Thank you.

TABLE OF CONTENTS

LIST OF FIGURES

LIST OF TABLES

CHAPTER 1 INTRODUCTION

1.1 Solid-state mediator supercapacitor

1.1.1 Supercapacitors

Supercapacitors (SCs) are high-specific power and long cycle-life systems, and due to their fast charge storage/delivery capability, outperform advanced batteries in applications having high peak power demand. SCs have been widely applied to various technologies, capable of providing peak power and power conditioning, and have shown potential to be used as standalone energy-storage device. Applications of SCs include military power systems, electric vehicles (EVs), hybrid electric vehicles (HEVs), uninterruptible power supplies (UPS), DC power systems, and mobile devices.

Traditionally, there are three types of supercapacitors: electrical double layer capacitor (EDLC), pseudocapacitor, and hybrid capacitor. The charge/discharge processes in EDLCs may be represented by the following equations [1,2]:

on the positive electrode:

$$E_S + A^- \leftrightarrow E_S^+ // A^- + e^-. \tag{1.1}$$

on the negative electrode:

$$E_S + K^+ + e^- \leftrightarrow E_S^- // K^+. \tag{1.2}$$

and the overall reaction

$$E_S + E_S + K^+ + A^- \leftrightarrow E_S^- // K^+ + E_S^+ // A^- \tag{1.3}$$

where E_s represents the electrode surface area; // is EDL where the charge is stored on its either side; and K^+ and A^- are cations and anions of electrolyte, respectively. During both a charge and discharge process, the charge density at interface and the electrolyte concentration change.

The pseudocapacitors store electric charge mainly at the expense of Faradaic reversible redox reactions of active materials in the electrodes and with the EDL capacitance. Several types of Faradaic processes occur in the electrodes of pseudocapacitors. Firstly, reversible processes, for example, adsorption of hydrogen on the surface of platinum or gold. Secondly, redox reactions of transition metal oxides, for example, RuO_2 and MnO_2, as well as a variety of oxide mixtures. Thirdly, reversible processes of electrochemical doping-dedoping in electrodes based on conductive polymers [3,4]. Fourthly, the electrodes can be made from Keggin-type hetero-polyacids that are particles of a molecular scale with a maximized contact area between the electrolyte and active materials [5].

In the case of an electrode coated with RuO_2, the redox process in the potential range 0.1-0.3 V (vs. a standard hydrogen electrode in the same solution) occurs reversibly [6]. The processes of intercalation and diffusion of protons, which occur in the ruthenium oxide layer during the redox reaction, alter the oxidation state of ruthenium ions in the oxide film [1]. The electrochemical reactions that proceed in such pseudocapacitors are represented in the following manner (in the case of RuO_2).

on the positive electrode:

$$HRuO_2 \leftrightarrow H_{1-\delta}RuO_2 + \delta H^+ + \delta e^- \quad (1.4)$$

on the negative electrode,

$$HRuO_2 + \delta H^+ + \delta e^- \leftrightarrow H_{1+\delta}RuO_2 \quad (1.5)$$

and the overall reaction

$$HRuO_2 + HRuO_2 \leftrightarrow H_{1-\delta}RuO_2 + H_{1+\delta}RuO_2 \quad (1.6)$$

Here, $0<\delta<2$, while RuO_2 and $HRuO_2$ represent the positive and negative electrodes in a completely charged state. The protons travel from one electrode to the other through a separator during charge and discharge. The movement of electrons occurs at the same time through the current source or the external load. The number of ions that take part in the EDL generation process is usually smaller than the number of protons being exchanged between the two electrodes. Hence, the capacitance or specific energy of pseudocapacitors is much greater than that of EDLCs. For EDLC, the capacitance reported is usually <100 F g^{-1} with aqueous electrolytes, or <50 F g^{-1} with solid-state electrolyte. For RuO_2, the valence of Ru can change from +2 to +4. A capacitance of 768 F g^{-1} can be achieved with amorphous form of $RuO_2 \cdot nH_2O$ whose internal surface can be effectively accessible by protons in the liquid electrolyte. However, Ru is a precious metal. Mass production and widespread applications of Ru based supercapacitors are hindered by its high price.

The hybrid SCs or asymmetrical SCs are based on electrodes of different types. For example, one electrode is made of a metal oxide (pseudocapacitor) and the other is based on an activated carbonaceous material (EDLC). The main factor that motivates the development of EDLCs was the need for rechargeable energy devices that would have

much higher specific power and better cycle life than batteries. By their specific energy, EDLCs occupy intermediate position between electrolytic capacitors and batteries in a Ragone plot of electrochemical power sources [7]. However, in many military and commercial applications, it is desired to go across boundary of the EDLCs to enable even greater values of energies of SCs, specifically, up to 20-25 Wh kg^{-1}. A great advantage of hybrid SCs is that they have both large specific power and energy. Hybrid SCs may replace batteries in the applications that require high power and high cycle life. Quest for SCs with both large specific power and high specific energy is the main goal of current studies.

1.1.2 Limits of the state-of-the-art technology for all-solid-state supercapacitors

Energy E stored in an EDLC is proportional to its capacitance, C, as well as to the voltage U applied in the second power [8]:

$$E = \frac{1}{2} C U^2, \tag{1.7}$$

while the maximum power P_{max} (energy delivered during time t) is independent of the capacity:

$$P_{max} = \frac{E}{t} = \frac{U^2}{4R_s}. \tag{1.8}$$

The resistance R_s which appears in Equation 1.8 is mainly due to the resistance of the electrolyte contained both in the carbon material as well as in the separator. For the pseudocapacitors, the maximum power is controlled by the kinetics of electrochemical

reactions, internal resistance, and mass transfer rate. The higher the kinetics, the conductance, and mass transfer rate, the higher the maximum power.

Because the resistance of the electrode material is much smaller than that of the electrolyte material, the series resistance, R_s, of EDLC with porous electrodes fully impregnated with electrolyte is given by [2]:

$$R_s = R_s^{electrode} + R_s^{separator} = \frac{1}{\sigma}\left[\frac{2l_{electrode}}{3\pi(\lambda/2)^2 N} + \frac{l_{separator}}{A_{separator}}\right] \tag{1.9}$$

where σ is conductivity of the electrolyte, $\lambda/2$ is the average pore radius, N is the number of pores in the unit area, $l_{electrode}$ is the thickness of the electrodes, $l_{separator}$ and $A_{separator}$ are respectively the thickness and area of the separator.

It is well known that for same active materials, SCs with a liquid electrolyte outperform SCs with a solid-state electrolyte. Generally speaking, a solid-state electrolyte is less conductive than a liquid electrolyte. In addition, the fluidity of a solid-state electrolyte is much lower than that of a liquid electrolyte. Thus, the solid-state electrolyte is unable to fill up all pores in the active materials or the number of pores filled with the solid-state electrolyte in the unit area is less than that for a liquid electrolyte. According to Equation 1.9, the series resistance is greater for solid-state electrolyte SCs. In addition, establishment of electroneutrality is required for charge/discharge. However, in solid-state electrolyte, limited contact area between the electrolyte and active materials cause limited accessibility of ions to the active sites, resulting in low utilization of active materials. In an effort to resolve these problems with all-solid-state SCs, a new concept of mediator SCs is introduced.

1.1.3 Description of the concept and rationale of research

1.1.3.1 Mediator supercapacitor

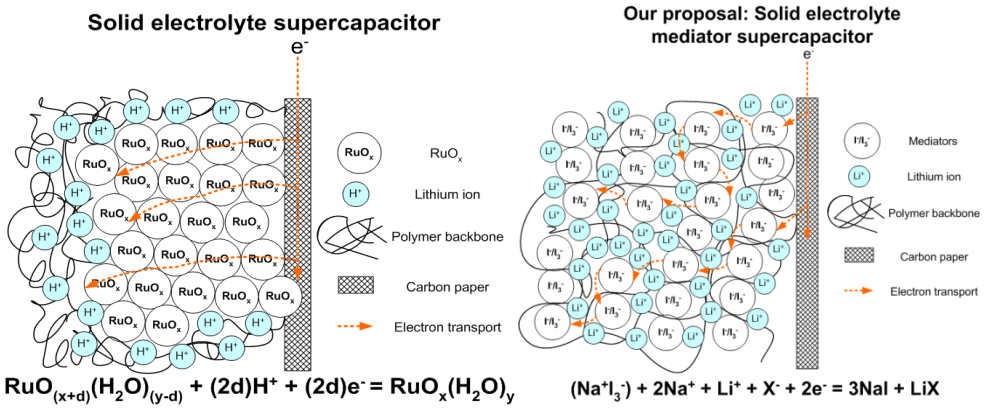

Figure 1.1 Comparison between the SCs with un-mediated (left), and mediated (right) solid-state electrolytes during a charge process.

The proposed concept is illustrated in Figure 1.1. Figure 1.1 is a schematic of a SC electrode during a charge process. On the left, the negative electrode is made from high surface area RuO_2 as the active material. The solid-state electrolyte cannot get into the pores of the active material. Thus, the active sites inside of the RuO_2 cluster cannot be charged due to lack of ion accessibility to these sites to balance the charge. On the right, mediators as the active material are dispersed homogenously into the solid-state electrolyte. As a result, all molecules of the active material can be charged because they are surrounded by ions in the solid-state electrolyte. The negative charge centers of the mediators will form "molecular capacitors" with the cations in the electrolyte. This maximizes the contact area between the electrolyte and active components to unprecedented level. The total capacitance of both electrodes can be increased by many folds. Similar analysis can also be applied to the positive electrodes. This new concept of SC is referred as mediator SC.

1.1.3.2 Electrolyte materials

According to the analysis in previous section, porous carbon electrodes and porous redox oxide electrodes with mediators in the electrolyte could enable unprecedented high capacitance, power, and energy. One of the keys for realization of the concept is to select ideal electrolyte materials that have a high ionic conductivity, electrochemical stability, and solubility for mediators. Polymer electrolytes (poly (ethylene oxide), polyvinylidene fluoride, Nafion etc.) have been used to fabricate SCs. Because of a wide application of Nafion and other sulfonated polymers in polymer electrolyte fuel cell, they are readily available. However, a major problem for Nafion as the polymer electrolyte is that it contains water that electrolyzes at a voltage greater than 1.2 V. Therefore, other polymer electrolytes including poly (ethylene oxide) (PEO) and polyvinylidene fluoride (PVDF) will be used.

1.1.3.3 Mediators

The redox pairs in the form of molecules should be dissolvable in the polymer electrolytes. The redox pairs that will be chosen for the study and their standard reversible electrode potentials are listed as follows:

I_2/I^- (I_3^-/I^-) E_0=0.54 V (SHE)

$Fe(CN)_6^{-4}/Fe(CN)_6^{-3}$ E_0=0.36 V (SHE)

Ferrocene [$(Fe(C_5H_5)_2$] and ferricinum [$Fe(C_5H_5)_2^+$] E_0=0.77 V(SHE)

The mediators that may be in the forms of inorganic or organic salts will be dissolved in a solution. The key is to identify a solvent that can dissolve the mediators and polymer electrolytes. I_2/I^- pairs have been studied thoroughly because of their application in dye-

sensitized solar cells (DSSCs). In the case of NaI and I_2, they can be dissolved in acetone and mixed with polymers to make polymer electrolyte solution [9]. The $Fe(CN)_6^{-4}/Fe(CN)_6^{-3}$ mediators in the forms of $K_4Fe(CN)_6/K_3Fe(CN)_6$ can be readily dissolved in water and organic solvents. Ferrocene [$(Fe(II)(C_5H_5)_2$] and ferricinum [$Fe(III)(C_5H_5)_2^+$] are readily dissolvable in many simple organic solvents (e.g. ethanol and isopropanol) [10]. Of course, there are many other redox pairs not included in the list. Another requirement for the mediators is that their reversible electrode potentials are within the electrochemical widow of the electrolyte.

1.1.3.4 Conduction of mediator in polymer electrolyte

The conductivity of the mediator-containing polymer electrolyte is expected to be much greater than that of the polymer electrolytes. For diffusion of mediators or redox pairs in electrolytes, two elementary processes are in operation: 1) the conventional migration of the species, and 2) the electron exchange reaction which causes an apparent displacement. The second process is also called transfer diffusion. The mechanism can be expressed by:

$$AX+A \leftrightarrow A+AX \tag{1.10}$$

where A is the reduced state of a species, AX is the oxidized state of the species, X is a molecule, ion, radical, or energy quantum. The net effect is that A and AX exchange their positions and translate a step to the left and right respectively. Figure 1.2 illustrates the transfer diffusion of Fe(III)/Fe(II) and I_3^-/I^-.

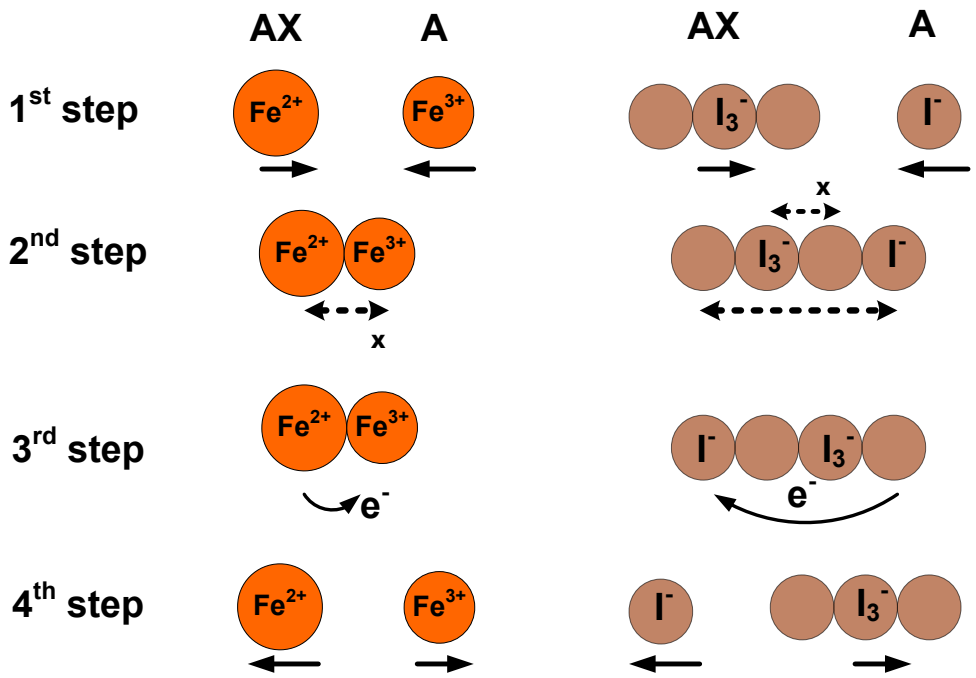

Figure 1.2 Transfer processes for Fe(III)/Fe(II) and I_3^-/I^-: step 1, approach of the reactants; step 2, the moment of collision; step 3, electron transfer; step 4, the separation of products.

The apparent conductivity of the mediators in an electrolyte (water or organic solvents) is given by:

$$\sigma = \left(\frac{2e^2}{kT} D_{AX}\right) c_A + \left(\frac{e^2 \delta_{AX}^2 k_{ex}}{3kT}\right) c_A^2 \qquad (1.11)$$

where D_{AX} is the diffusivity for conventional or physical diffusion, k is the reaction rate, δ_{AX}^2 is the inter-mediator distance for electron transfer reaction, c_A is the concentration of A, the mediator. In liquid solutions, the transfer diffusion related conductivity of I_3^-/I^- can be 0.05-0.1 S cm^{-1} when the concentration is 1 mol L^{-1}.

1.1.3.5 XAS study of the chemical state of mediators in polymer electrolytes

The charge storage mechanism of mediators in both liquid and solid-state electrolytes was not investigated in detail. A mechanism is proposed as follows (Nafion electrolyte):

$$Fe(II)(C_5H_5)_2 + (\text{sulfonated group})^- \leftrightarrow Fe(III)(C_5H_5)_2^+//(\text{sulfonated group})^- + e^- \quad (1.12)$$

$$3HI + (\text{sulfonated group})^- \leftrightarrow (\text{sulfonated group})\text{-}H + I_3^-//H^+ + H^+ + 2e^- \quad (1.13)$$

where // is referred to "molecular capacitor". However, the actual oxidation/reduction state or the valence change during electrochemical polarization may be different. The understanding of the electrochemical mechanism associated with the pseudo-capacitive characteristics is a key to realize SCs with optimized performance, long cycle life, low self-discharge etc. To probe the oxidation state change during the electrochemical process became a crucial topic. As have been reported in the literature, *ex situ* and *in situ* X-ray absorption spectroscopy (XAS) are capable to evaluate the electronic and structural properties of the redox species during electrochemical polarization. XAS is a powerful tool for probing the mechanism of the redox reactions.

1.1.4 Objectives of the Research

The objectives of the proposed research are: 1) fabrication and demonstration of an all-solid-state mediator SC with high specific power and energy; 2) probing the charge/discharge mechanisms with *in situ* XAS; and 3) optimization of the all-solid-state mediator SC. The benchmark materials are PEO/Li salt as polymer electrolyte, $K_4Fe(CN)_6/K_3Fe(CN)_6$or I_2/NaI as the mediators in the electrolyte, Nafion membrane as the separator, and high surface area carbon nanofoam as current collector. Since the

potential cannot be over 1.2 V for Nafion, PVDF/Li salt membrane was prepared to replace Nafion membrane in the mediator SCs.

1.2 Atomistic modeling and EC STM imaging of the interface between catalyst and electrolyte in polymer electrolyte fuel cells

1.2.1 Background

Polymer electrolyte fuel cells (PEFCs) hold great promise for providing clean, high energy density, and high efficient power [11,12]. The availability of Nafion electrolyte and Pt based catalysts and addition of ionomer into the catalyst layer are the milestones of the early advancements of the PEFC. However, commercialization of PEFCs has not been realized due to their inherent disadvantages, including the high costs of Pt and Nafion and insufficient performance of Pt catalysts in conjunction with the Nafion electrolyte [13-15]. Searching for alternative catalysts and electrolytes have been major focuses of PEFC research in the recent decades. In spite of three decades of efforts on developing alternative catalysts and electrolytes, the most common choices for catalysts and polymer electrolytes are still Pt and Nafion, respectively.

One of the major barriers for PEFC technology is the very slow reaction kinetics for the oxygen electroreduction reaction (OER, $O_2 + 4H^+ + 4e^- \leftrightarrow 2H_2O$) at the cathode. The exchange current density on Pt/C catalyst in conjunction with Nafion electrolyte is reported to be 8.0×10^{-7} A cm^{-2} for OER at the cathode (ca. 10^{-3} A cm^{-2} for hydrogen oxidation at the anode) on the basis of area of the catalyst layer [16]. This is equivalent to 2.0×10^{-9} A cm^{-2} on the basis of true active surface area of Pt crystallites. However, in 0.5 mol L^{-1} H_2SO_4, Pt crystallites show an exchange current density between 5.0×10^{-7} and 6.0×10^{-6} A cm^{-2} on the basis of true active area of Pt [17]. Thus, the exchange current

density for the Pt/Nafion system is 2-3 orders of magnitude lower than that for the Pt/liquid electrolyte system. In another study, although sulfonated poly(arylene ether sulfone) (PAES) was found less conductive than Nafion, the Pt/PAES system enables an exchange current density 10 times greater than Pt/Nafion system [18].

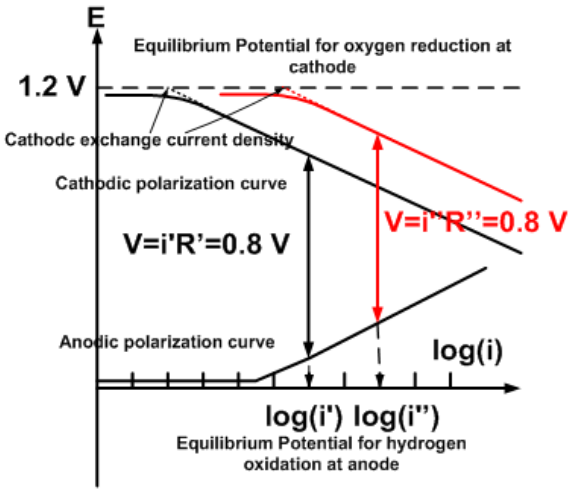

Figure 1.3 Schematic polarization curves for fuel cell anode and cathode.

There are, however, many other cases where the polymer electrolytes have similar conductivity to Nafion but resulted in much less exchange current density. These experimental facts indicate that the interface between a catalyst electrode and an electrolyte has a great impact on the electrochemical kinetics. In other words, the inherent reaction kinetics is largely determined by the catalyst/electrolyte couple, rather than the catalyst and electrolyte separately. Thus, it is critical to improve the fundamental understanding of these interfaces. As shown in Figure 1.3, if the cathodic exchange current density is increased by 3 orders of magnitude (from black to red) via improving the interface, the output current can also be increased dramatically (from i' to i'') while keeping the output voltage V a constant.

1.2.2 State-of-the-art descriptions of electric double layer and charge transfer at the interface between electrode and liquid electrolyte

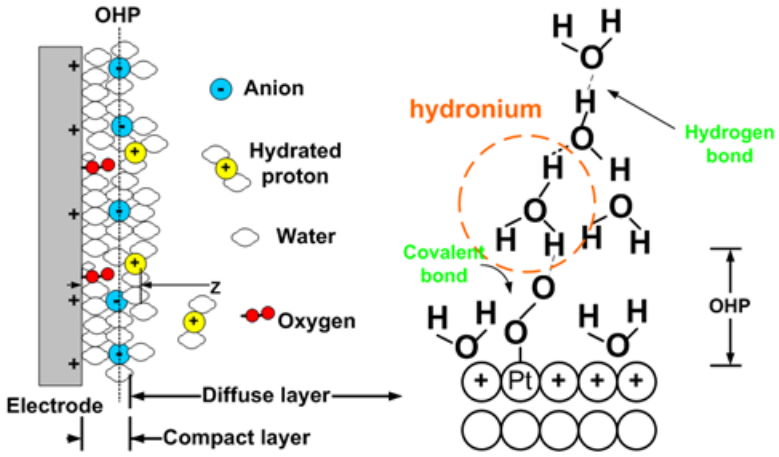

Figure 1.4 Left: schematic illustration of EDL at solid/liquid interface. Right: Configuration of reactants in OER in ELD at Pt/acidic solution interface.

Historically, the description of an EDL is established as a distinct characteristic of solid/liquid electrolyte interface although it is assumed that an EDL should exist at any immiscible interfaces including electrocatalyst/polymer electrolyte interfaces (Figure 1.4) [19-22]. Ions in “diffuse layer” or beyond are about two solvent-molecule diameters (a few angstroms) away from the electrode surface because both the ions and the electrode surface are solvated [Figure 1.4(left)]. Ions in the “contact layer” inward the "inner Helmholtz plane (IHP)" have shed their solvation layer (these are usually the weakly solvated, large anions) and penetrated the solvent layer on the electrode; these, so called contact adsorbed ions are sitting directly on the electrode surface. Striking characteristics of such an EDL at a metallic electrode/aqueous liquid electrolyte interface include: 1) a very strong electric field in the compact layer (~2.5×10^{7} V cm^{-1} for a potential drop of only 1 V across the interface); 2) a relatively smaller dielectric constant (~5-7 vs. 78 in

bulk of an aqueous solution); 3) a high concentration of charges in the forms of ions and dipoles (20-30 μC cm^{-2} or 0.11-0.17 e per surface atom) forming a barrier for Faradaic reaction; 4) electrons of the metal spillover the metal surface into the compact layer giving rise to a possibility of electron tunneling or electron transfer at the interface [Figure 1.4(right)]. However, a generally accepted picture of the interface between Pt and Nafion hasn't been revealed yet.

1.2.3 Interface between Pt and Nafion electrolyte

Nafion's unique ionic properties are a result of incorporating perfluorovinyl ether groups terminated with sulfonated groups onto a tetrafluoroethylene (Teflon) backbone [26]. Solvation of the sulfonated group $-SO_3H$ by polar water molecules produce movable positively charged hydrated protons including hydronium (H_3O^+), $H_5O_2^+$, and $H_7O_3^+$, and hydrated $-SO_3^-(H_2O)_n$ groups. Thus, there are hydrophilic domains with hydrated protons and $-SO_3^-(H_2O)_n$ side groups and hydrophobic domains with C-F groups. Proton conduction is enabled through the interconnected nano-size network of hydrophilic domains. Logically, at the interface between Pt and Nafion exists both a layer containing water, hydrated protons and/or $-SO_3^-(H_2O)_n$ groups and a layer containing hydrophobic C-F groups. A recent nuclear magnetic resonance spectroscopy (NMR) study indicates that a strong adsorption of -CF groups and weak adsorption of sulfonated groups on Pt or Pt/Ru or carbon support do exist [27]. Figure 1.5 illustrates the reaction steps in OER (left) and a postulated picture of interface structure (right). Oxygen may diffuse via two paths: 1) through the thin film of Nafion covering the catalysts; 2) through the pores or gaps in the film. Once oxygen arrives at an active site on the catalysts, it will react with protons in Nafion and electrons from Pt to form water. Thus, modeling of the OER at

catalyst/Nafion interface involves two critical aspects: 1) defining the structure including and beyond contact layers, and including adsorbed and non-adsorbed molecules; and 2) describing proton and electron transfer in the reaction clusters or centers.

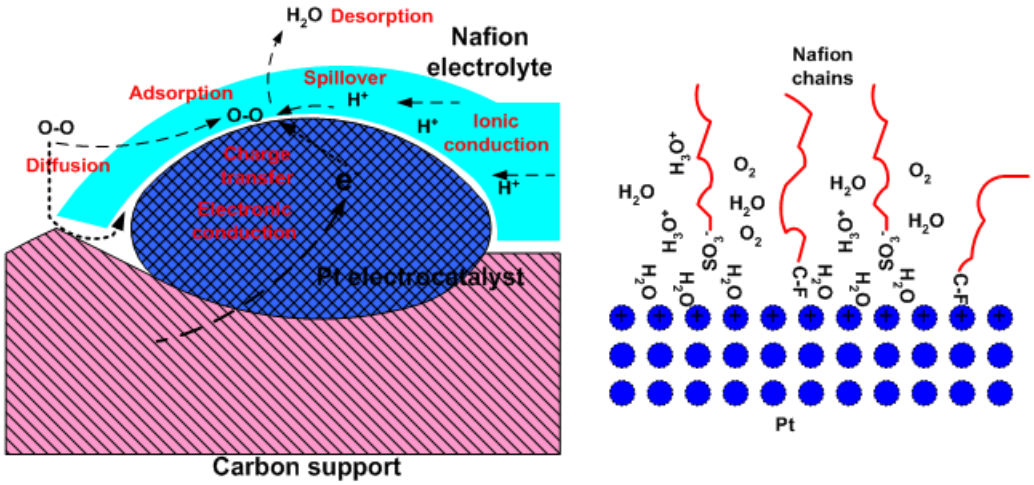

Figure 1.5 Reaction steps in oxygen reduction at the electrocatalsyst in a PEFC (left) and a postulated molecular scale structure of the interface (right).

1.2.4 Multiscale modeling hierarchy

A great effort has been made by ultra-computer developers to magnify the capacity of the hardware. *Ab initio* modeling/simulation of a cluster of multi-million atoms is now being attempted with one of the most powerful computers [23]. Even if similar attempts are successful, they must be very limited in terms of number of simulations and ranges of parameters. It is predicted that a Petaflop computer (with a processing speed of 10^{15} float point operations per second) will be developed in 2012. This computer will be able to execute MD simulations for a cluster of 10^{12} atoms (about a micrometer in size) or perhaps *ab initio* simulations for a cluster of 10^{8} atoms. The increase of computer capacity roughly follows Moore's law that predicts that the capacity of computer doubled

in every 24 months. However, according to a recent analysis by Thompson and Parthasarathy, there will be a limit for the increase of computer capacity if future computers are based on architectures similar to currently existing ones [24]. This limit is related to the minimum size (10 nm) of a complementary metal-oxide semiconductor (CMOS) device and is called CMOS limit. This means that roughly speaking, the capacity can be further increased by 100-1000 times. They are not optimistic with the realization of a computer based on molecular electronic storage devices because wiring of such devices would be a formidable task. It seems that modeling a molecular system with a macroscopic size (10^{24} atoms) in a timescale of 10^3 seconds cannot be achieved in a foreseeable future.

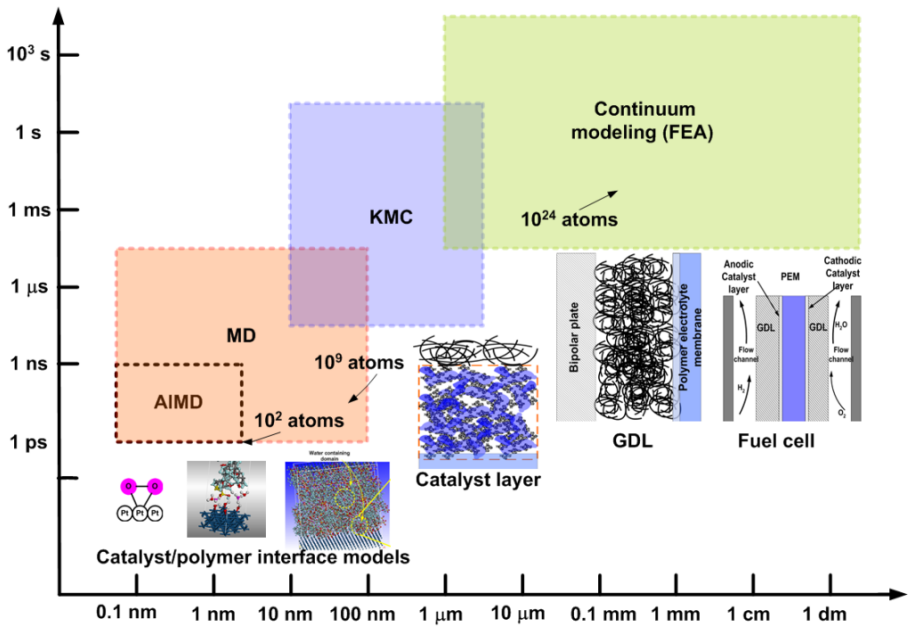

Figure 1.6 Multiscale modeling hierarchy. AIMD: *ab initio* molecular dynamics. MD: molecular dynamics. KMC: kinetic Monte Carlo modeling. FEA: finite element analysis.

Instead of enhancing the performance of computers, many theoreticians have tried to enhance the efficiency of computation by improving computational codes. One of the

approaches is to reduce the dependence of the computation for the present step on the computational results for previous steps along the system trajectory or increase the parallelism of the computation. The other effective approach is the use of concept of hierarchical coupling of paradigms on different scales [25]. This approach is so-called multiscale modeling. In an optimal situation, as shown in Figure 1.6, a modeling method for specific spatial scale and timescale ranges should share an overlapping range with a method at the higher scale end and another at the lower scale end. However, all of these multiscale approaches inevitably result in loss of certain atomic details and are not general or system specific.

1.2.5 Significance of the research

Although the molecular structure and charge distribution at the electrocatalyst/polymer electrolyte interface have been recognized as having a great impact and as being an effective control on the electrochemical reactions in PEFCs, there is inadequate success on this topic. The primary reason may be that defining the EDL structure at a solid/polymer interface is much more difficult than defining the EDL at a solid/liquid interface. Many state-of-the-art experimental techniques for defining the EDL at solid/liquid interfaces are unsuitable for the study of solid/polymer interfaces.

1.2.5.1 Atomistic modeling

State-of-the-art atomistic modeling includes 1) simulation of the atomic structure at interface [25,28] (not the electronic structure) using MD methods that do not evaluate wavefunctions and require much less computational effort, 2) *ab initio* modeling of solid/liquid interface without polymer [29,30], and 3) *ab initio* description of charge transfer in a model with a few atoms without polymer [31,32]. All charge transfer models

in the literature can evaluate the activation energy but hardly exchange current density. Moreover, results from these modeling studies are not comparable with experimental results because the *ab initio* modeling results for charge transfer only represent a few from billions of possibilities of ensemble in a real catalyst layer. In order to evaluate the exchange current density and the polarization curve that can be compared with experiments the basic requirement is to perform *ab initio* simulation of 10^8 atoms in a time scale of 1 millisecond at least. Now, a pioneering attempt is underway to perform simulation (with pseudopotential methods not classic *ab initio* methods) of 10^6 atoms using the most powerful computers [33]. Thus, high throughput *ab initio* modeling (excluding semi-empirical/pseudopotential methods) for realistic system in a realistic timescale is also not anticipated in a foreseeable future.

A fresh idea to the solution of the problem or dilemma is: we need to describe both the process in atomic details and a realistically large system in a large temporal scale at the same time. The steps of the simulation method are as follows:

1) To conduct large-scale MD simulations to evaluate in the diffuse layer of the EDL, where the transport processes are much slower than electron transfer.
2) To conduct small scale *ab initio* molecular dynamic methods to refine the structure in the contact layer.
3) To evaluate the electron transfer and the exchange current density using statistical quantum mechanics method by integrating the transfer Hamiltonian with wavefunctions generated by the *ab initio* methods.

By using the hybrid atomistic modeling, the small scale phenomena and structure at the interfaces and in the bulk can be described in detail while microscopic features can be extended to a large system with a size in the continuum domain shown in Figure 1.5. By comparing the results for the electrocatalyst/H_2SO_4 system with the results for the electrocatalyst/Nafion system, the effect of the polymer can be manifested. The models allow almost freely change the molecular units of materials for electrode and electrolyte and thus are able to predict the kinetics of oxygen reduction in other types of catalysts and polymer electrolytes.

1.2.5.2 Electrochemical scanning tunneling microscopy

Interface between electrode (a phase conducting electrons) and electrolyte (a phase conducting ions) dictates functions of electrochemical devices including fuel cells, supercapacitors, rechargeable batteries, and photovoltaic cells [34]. Specifically, in PEFCs, the interface between Pt nano-particulates and polymer electrolyte (most commonly Nafion ionomer) dictates the catalytic activity and activation polarization [35]. Traditionally, scanning tunneling microscopy (STM) is capable of *in situ* imaging conducting solid surface with an atomic resolution and detecting defects that dominate the catalytic activity in air or in vacuum [36,37]. While the interfaces, in fact the electrode surfaces, in liquid electrolytes can be imaged with an atomic resolution using an electrochemical scanning tunneling microscopy (EC STM), to date the interfaces between solid phases cannot be imaged using STM techniques. High resolution transmission electron microscopy (HRTEM) has been used to image the surfaces of Pt catalysts and carbon supports covered with Nafion ionomer [38,39]. However, HRTEM requires a high

vacuum. Application of potential to the sample in a HRTEM and hence *in situ* imaging the interfaces with a HRTEM are difficult.

Usually, electron tunneling occurs through a vacuum or air gap of a few angstroms between two electron conducting phases or conducting and semiconducting phases [37,38]. If the gap contains thin layer (~nanometer) molecules of non-conducting compounds, electron tunneling and visualization of atoms are barely possible. In the case when the gap contains a thick or bulk film (tens of nanometers) of non-electron-conducting substance, only very blur and low resolution images could be obtained [40-43]. The mechanism of imaging a thick non-electron-conducting substance was unclear. However, these results imply that the interface between the non-electron-conducting substances and the electron-conducting substance may be imaged with a STM.

1.2.6 Research Objectives

The objectives of this research are 1) to define and characterize the structure and charge distribution or EDL structures at nano-crystalline electrocatalyst/polymer electrolyte interface in contrast to the structure at nano-crystalline electrocatalyst/H_2SO_4, and 2) to evaluate the relationship between the interface structure characteristics and the electrochemical charge transfer kinetics in oxygen reduction on cathode. These efforts will reveal the fundamental differences between Pt/aqueous electrolyte and Pt/Nafion electrolyte and their impacts on the kinetics of oxygen reduction on Pt. The specific research tasks are as follows:

1) Establish classical molecular dynamic (MD) models for defining the interface structure and charge distribution in hundreds of molecular layers above the Pt surface in the Nafion electrolyte and in H_2SO_4 solution.

2) Establish *ab initio* atomistic models for defining atomic structures and electronic wavefunctions including those for adsorbed species in the contact layer. The focus is the most probable configurations of the reactants (hydrated protons and oxygen) and their proximity (water, C-F and hydrated sulfonated groups) as inputs for evaluating charge transfer kinetics in oxygen reduction at the interfaces.
3) Establish statistical quantum mechanical methods for computation of the reaction current density as a function of interface structures and electrode potential in the cases of the Pt/Nafion and Pt/H_2SO_4.
4) Characterize the size and morphology of the electrocatalyst with Nafion electrolyte (ionomer) using EC STM.

CHAPTER 2 LITERATURE REVIEW

2.1 Principle of supercapacitor

Supercapacitors (SCs) can be divided into electrical double layer capacitors (EDLC), pseudocapacitors, and a combination of those above two. The primary difference between EDLCs and pseudocapacitors is that the different charge storage mechanism. Generally speaking, the two different storage mechanisms usually exist at the same time. But one mechanism may be dominant over the other one. Table 2.1 lists comparisons between EDLC and pseudocapacitor [44].

Table 2.1 Comparisons between EDLC and pseudocapacitor [44].

	EDLC	Pseudocapacitor
1.	Non-Faradaic	Involves Faradaic process(es)
2	20-50 μF cm^{-2}	2000 μF $cm^{-2}$for single-state process; 200-500 μF cm^{-2} for multi-state, overlapping processes
3	Capacitance is fairly constant with potential, except through the potential of zero charge	Capacitance is fairly constant with potential for RuO_2; for single-state process, exhibits marked maximum
4	Highly reversible charge/discharge	Can exhibit several maxima for overlapping, multi-state processes, as for H adsorption on Pt; Quite reversible but has intrinsic electrode-kinetic rate limitation determined by R_f
5	Has restricted voltage range (contrast non-electrochemical electrostatic capacitor)	Has restricted voltage range
6	Exhibits mirror-image voltammograms	Exhibits mirror-image voltammograms

2.1.1 Electrical double layer capacitor

As seen in Figure 2.1, an EDLC is usually composed of two current collectors, porous electrodes with high surface area, a semi-permeable membrane, and liquid electrolytes.

The separator is placed between the negative and positive electrodes, which prevents the electric contact.

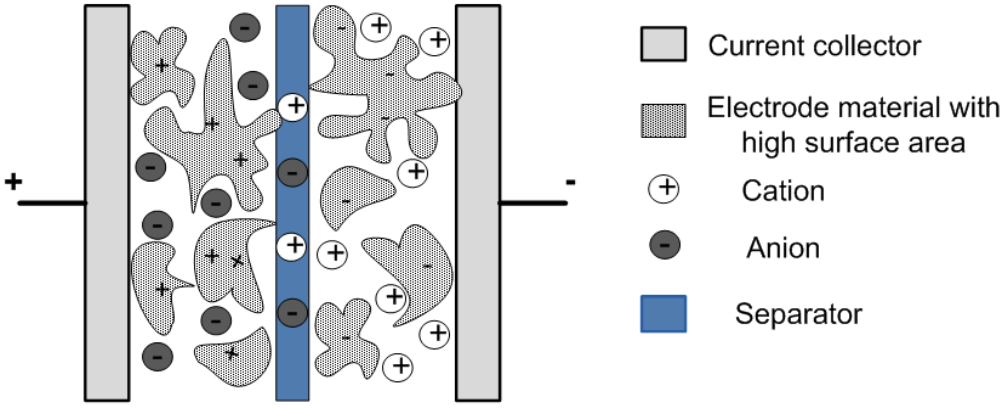

Figure 2.1 Schematic of an EDLC

During a charge process, two electrodes are charged with different charges respectively. For example, positive charges are accumulated in the positive electrode. To establish electroneutrality, the counter ions from the liquid electrolyte will approach the electrode surface as shown in Figure 2.1. There is no charge transfer between the electrolytes and the electrodes involved in the charge storage/discharge process. Thus, the charge/discharge process is also termed as “non-Faradaic”.

The EDLCs share a similar charge mechanism with traditional dielectric capacitor, which is charge separation. However, EDLCs can deliver a substantially high energy capacity than the traditional capacitors because of the following reasons: (1) the distance across which charge transfer takes place is very small, in the order of ~nm [22]; (2) electrode with large surface area are used so as to store more charges per unit weight.

There are several considerations people take into account to choose a specific material for the electrode material in an EDLC:

- High conductivity
- High surface area
- Good stability in terms of corrosion, high temperature
- Low cost

Carbon in its various forms has been widely used as the electrode materials for EDLCs because they have several properties as listed above. Furthermore, it also has advantages like different forms attainable, easy processability [45].

2.1.1.1 Carbon black

Carbon black (CB) refers to a group of industrial products involving thermal, furnace, channel, and acetylene blacks. They consist of elemental carbon in the form near spherical particles of colloidal size, coalesced into particle aggregates and agglomerates. Partial combustion or thermal decomposition of hydrocarbons is applied to obtain CB [46].

2.1.1.2 Carbon fibers

Carbon fiber is also known as graphite fiber or carbon graphite. The typical diameter of the activated carbon fibers are ~10 μm and the pore size is very narrow (<2 nm). The porosity of the activated carbon fibers is largely situated at the surfaces of the fibers, therefore good accessibility to active sites can be ensured.

A synergetic effect can be achieved because the EDL capacitance is combined with pseudocapacitance. When carbon materials are enriched with heteroatoms (N or O) containing functional groups, there will be an enhanced specific capacitance because of the Faradaic redox reactivity originated from those functional groups [47].

2.1.1.3 Carbon nanostructure

Carbon nanotubes (CNT) can be synthesized by the catalytic decomposition of certain hydrocarbons. In the literature reports, the performance of the as-received CNTs is always low. Therefore, methods to combine CNTs together with metal oxides or conducting polymers have been proposed in order to increase the performance.

A very high specific capacitance value, 1170 F g^{-1}, was reported for RuO_2/CNT nanocomoposite [48]. The RuO_2/CNT film electrode had a 3-D interconnected nanopore structure. To reduce the cost, other metal oxide/CNT nanocomposite electrodes were also extensively studied. Amade et al. have proposed a single sequential process of sputtering, annealing and plasma enhanced chemical vapor deposition to produce dense and uniform vertically aligned CNTs [49]. MnO_2 was then electrodeposited lining the surface of the vertically aligned CNTs. It was reported that the very aligned CNTs present several advantages with respect to the non-aligned CNTs, such as low contact resistance, large specific surface area, fast electron transfer kinetics, and low capacitive currents. Chemical precipitation was employed to produce the NiOOH/multi-walled CNT, which formed electrically conductive networks [50].

Dong et al. have synthesized polyaniline/multi-walled carbon nanotubes composites by an *in situ* chemical oxidative polymerization method [51]. The behaviors of the composite electrodes were studied in neutral system. In a study of polyaniline with tubular shape, it was found that polyaniline can maintain the original tubular morphology after heat treatment [52]. This kind of polyaniline-based CNTs were used as electrode materials for supercapacitors in KOH solution, and results show that they have high specific capacitance of 163 F g^{-1}, and good cycle stability. The authors also found that the

reason of good performance would be the presence of pyridine and quaternary nitrogen when appropriate content of nitrogen was introduced, resulting in improvement of electron mobility and the wettability of the electrode.

2.1.2 Pseudocapacitor

The charge storage capacity of a pseudocapacitor arises on electrodes when the application of a potential induces Faradaic current from reactions such as electrosorption or from the oxidation-reduction of the electroactive materials. The charge capacity of a pseudocapacitor is typically greater than that of an EDLC, although EDLCs have faster kinetics.

2.1.2.1 Metal oxides

Ruthenium oxide (RuO_2) based supercapacitors

RuO_2 as the electrode active material, either in its crystalline form or amorphous hydrous form, is able to deliver a large specific capacitance [53]. Among those transitional metal oxides SCs, RuO_2 has been the most successful one in term of a wide potential window, highly reversible redox reactions, remarkably high specific capacitance, long cycle life, and high electronic conductivity [45,54-58]. However, as a noble metal oxide, the high cost of RuO_2 limits its commercial application. To address the high cost problem and to maximize the performance at a minimized quantity of RuO_2, thin layers of RuO_2 have been deposited on carbon materials and conducting polymers. By doing so, the advantage of RuO_2 can still be maintained while the amount of Ru consumption is minimized. Table 2.2 summarizes the electrode properties and the electrochemical performance of the RuO_2 thin film based SCs.

Table 2.2 A summary of the RuO_2 based SCs.

	Electrode properties	SC cell configuration	Specific capacitance ($F\ g^{-1}$)	Reference
1	RuO_2 is heterogeneously nucleated, opening in the CNT are not blocked by RuO_2 deposit. RuO_2 on CNT with 3-D nanoporous structure	$RuO_2/H_2SO_4/Pt$ (0-1.0 V, 10-400 mV s^{-1})	965 (400 mV s^{-1})	[59]
2	Different morphologies with different deposition rates, cracked mud morphology	$RuO_2/H_2SO_4/Pt$ (0-1.0 V, 25 mV s^{-1})	760 (0.34 mg cm^{-2}) 505 (1 mg cm^{-2})	[60]
3	As deposited hydrous and amorphous, crystallization at high temp annealing, porous layers with fine particles, 50-100 nm diameter, different morphologies with different substrates, amorphous RuO_2 on CNT with 3-D nanoporous structure.	$RuO_2/H_2SO_4/Pt$ (0-1.0 V)	1170 (10 mV s^{-1}) on CNT substrate	[61]
4	Different morphologies with different pH values of bath, average particle size 0.4-0.5 μm.	$RuO_2/H_2SO_4/Pt$ (0-1.0 V)	220-380 (different pH)	[62,63]
5	Microstructure contains flows with grooves and voids, amorphous	$RuO_2/H_2SO_4/Pt$ (0-1.0 V)	625 (5 mV s^{-1})	[64]
6	Amorphous, porous and compact morphology	$RuO_2/H_2SO_4/Pt$ (-0.1-0.6 V)	650	[65]
7	RuO_2 deposited on Ti planar sheet to form particulate aggregates and RuO_2 can be feasibly incorporated into TiO_2nanotubes with an open pore mouth structure.	$RuO_2/H_2SO_4/Pt$ (0-1.0 V)	241 for RuO_2/Ti, 640 for RuO_2-TiO_2/Ti	[66]
8	Porous, hydrous, amorphous, flake-like morphology	$RuO_2/H_2SO_4/Pt$ (-0.1-0.7 V)	276	[67]
9	Porous, hydrous, amorphous and compact morphology	$RuO_2/H_2SO_4/Pt$ (-0.1-0.6 V)	1190	[68]
10	67.3 $m^2\ g^{-1}$ surface area, 48.5 Å mean pore diameter, particle size depends on Sn content.	$RuO_2/H_2SO_4/Pt$	690	[69]

The following reaction can be used to describe the energy storage mechanism of SC with RuO_2 as the active material.

$$RuO_2 + dH^+ + de^- \leftrightarrow RuO_{2-d}(OH)_d \quad \text{with } 0<d<2 \tag{2.1}$$

There are four steps involved in determining the capacitive performance of ruthenium oxides: (i) electron hopping within $RuO_x \cdot H_2O$ particles; (ii) electron hopping between particles; (iii) electron hopping between electrode materials and current collectors; and (iv) the proton diffusion within $RuO_x \cdot H_2O$ particles [70].

Manganese oxide (MnO_2) based supercapacitors

In recent years, manganese oxide (MnO_2) has received great attentions for its potential as an alternative material to RuO_2. MnO_2 is abundant on the earth, environmentally friendly, and readily available at a much lower price than RuO_2 [71].

Like ruthenium, manganese has several oxidation states, namely, Mn(0), Mn(II), Mn(III), Mn(IV), Mn(V), Mn(VI), and Mn(VII) [72]. However, good reversibility cannot be obtained between all the oxide states. The most often studied phases are MnO_2 with an oxidation state of 4+, Mn_2O_3 with an oxidation state of 3+, or a mixture of the two phases [73]. The following methods were employed to prepare the manganese oxides with controlled morphologies and structures, nanocasting [33], thermal decomposition [74], sol-gel method [75], sputtering deposition [76], and co-precipitation method [77]. Table 2.3 summarizes the electrode properties and the electrochemical performance of the MnO_2 thin film based SCs.

The charge storage mechanism for manganese oxides based SCs on surface adsorption of electrolyte cations and proton incorporation of Mn ions oxidation/reduction is described with the following reaction [84]:

$$MnO_\alpha(OC)_\beta + \delta C^+ + \delta e^- \leftrightarrow MnO_{\alpha-\delta}(OC)_{\beta+\delta} \quad (2.2)$$

Table 2.3 A summary of the MnO_2 thin film based SCs.

	Electrode properties	SC cell configuration	Specific capacitance ($F\ g^{-1}$)	Reference
1	Poor crystallinity, crystalline size 6 nm, Porous structure	MnO_2/NaCl/Pt	199 (50 mV s^{-1}), 224 (10 mV s^{-1})	[78]
2	Amorphous by XRD, Different morphologies for different methods, Nanostructured hydrous MnO_2, Non-stoichiometric by XPS	MnO_2/Na_2SO_4/ Pt	230 (25 mV s^{-1})	[79]
3	Higher nucleation rate with Triton X-100, Spherical grains, crystalline by XRD, greater surface area with Triton X-100	MnO_2/Na_2SO_4/ Pt	355 (20 mV s^{-1})	[80]
4	Amorphous, with composites corresponds to alpha-MnO_2, clusters, rough morphology, 40-70 nm particle size	MnO_2/Na_2SO_4/ Pt	410 (10 mV s^{-1})	[81]
5	Amorphous and hydrous MnO_2, by XRD	MnO_2/Na_2SO_4/ Pt	265-320 from GCD	[82]
6	Amorphous, annealing from 473 to 873 K showed nanocrystalline nature, surface with different morphologies.	MnO_2/KCl/Pt	330	[83]

Cobalt oxide (Co_3O_4) based supercapacitors

In addition to manganese oxides, cobalt oxides are also considered as good alternative materials to replace ruthenium oxides in SC applications. Co_3O_4 nanotubes were prepared via the anodic aluminum oxide template method [85]. The BET surface area for the $Co_3O_4$was found to be 218 $m^2\ g^{-1}$, and the specific capacitance was 574 $F\ g^{-1}$ at a charge/discharge current density of 0.1 $A\ g^{-1}$. The mechanism of the charge/discharge for Co_3O_4 was described by $Co_3O_4 + OH^- + H_2O \leftrightarrow 3CoOOH + e^-$. Kandalkar et al. prepared cobalt oxide thin film from cobalt chloride precursors by successive ionic layer adsorption and reaction method on copper substrate [86]. Cobalt oxide thin film showed maximum specific and interfacial capacitances of 127.58 $F\ g^{-1}$ and 0.37 $F\ cm^{-2}$,

respectively. A hierarchically porous Co_3O_4film with mesoporous walls was prepared via a liquid crystal template electrodeposition method [87]. The hierarchically porous architecture and its finer pores were able to enhance the mass transfer and increase the specific surface area. In addition to the high specific capacitance, Wang et al. reported that $Co(OH)_2$ also have good efficiency, long-term performance, and good corrosion resistance [88,89].

Nickel oxide (NiO) based supercapacitors

As shown in the reaction 2.3, $Ni(OH)_2$ can be oxidized to NiOOH during a charge process. This process is famous for its application in the secondary battery. However, the relatively low conductivity of the $Ni(OH)_2$ electrode has a negative effect to the power performance. The multi-walled carbon nanotube with high electrical conductivity and a mesoporous structure were employed as a conducting material because of their inherent conductive networks [90]. The electrochemical results showed that the maximum specific capacitance can reach 432 F g^{-1} for 10 wt% loading of $Ni(OH)_2$ composite at a scanning rate of 10 mV s^{-1}. Micaceous nanoflakes Ni which have dispersed sandwich and shaggy cauliflower shape were prepared through hydrothermal synthesis technique [91]. The shaggy cauliflower-like nanoflake structure within NiO was able to supply effective surface area for Faradaic redox of NiO, resulting in a high specific capacitance of 137.7 F g^{-1}. Inamdar et al. used the chemical bath deposition technique to synthesize a porous NiO thin film from an aqueous nickel nitrate solution [92]. No noticeable degradation of the NiO microstructure can be found after 1,500 cycles of charge/discharge, indicating a good stability.

$$Ni(OH)_2 \leftrightarrow NiOOH + H^+ + e^- \quad (2.3)$$

Other types of metal oxides based supercapacitors

The following table has summarized other types of metal oxides based SCs, including Tin oxide (SnO_2), Indium oxide (In_2O_3), Bismuth oxide (Bi_2O_3), Vanadium oxide (V_2O_5), and Iron oxide (Fe_3O_4).

Table 2.4 A summary of the metal oxide based SCs.

	Electrode materials and properties	Possible mechanism	Specific capacitance ($F\ g^{-1}$)	Reference
1	SnO_x cathodically deposited onto graphite electrode.	Surface adsorption of electrolyte cations C^+: $(SnO_x)_{surface} + C^+ + e^- \leftrightarrow (SnO_x^- C^+)_{surface}$	298 (10 mV s^{-1})	[93]
2	Electrode deposition of SnO_2 on stainless electrode		285 (10 mV s^{-1})	[94]
3	Electrochemically synthesized hydrophilic and nanocrystalline SnO_x film on ITO substrate	Intercalation of H^+ or C^+ followed by deintercalation upon oxidation: $SnO_x + H^+ + e^- \leftrightarrow SnO_xH$ $SnO_x + C^+ + e^- \leftrightarrow SnO_xC$	43.07 in NaOH	[95]
4	Electrodeposition of nanorods of In_2O_3		190 (10 mV s^{-1})	[96]
5	Chemical deposition of nanosphere and nanorod In_2O_3on ITO substrate		104.9 for nanorod In_2O_3, 7.6 for nanosphere In_2O_3	[97]
6	Electrodeposition of Bi_2O_3 thin films on copper substrate from aqueous alkaline nitrate bath	$Bi^{3+} + OH^- \leftrightarrow Bi(OH)_2^+$ $2Bi(OH)_2^+ + 2OH^- \leftrightarrow Bi_2O_3 + 3H_2O$	98	[98]
7	Electrochemically deposition of pervoskite nanocrystalline porous bismuth iron oxide ($BiFeO_3$) thin film electrode from alkaline bath		81	[99]
8	V_2O_5 gel/carbon composites was prepared by chemical reaction		26 kW kg^{-1} and 80 Wh kg^{-1}	[100]
9	Calcining V_2O_5 aerogel in the furnace to get Vanadium nitride (VN) powder	A combination of an EDL Formation and the Faradaic redox reactions that occur on	161 (30 mV s^{-1})	[101]

		the surface of these partially oxidized nitrides.		
10	Fe_2O_3 thin films were prepared by chemical successive ionic layer adsorption and reaction method	The decrease in capacitance has been attributed to the presence of inner active sites that cannot sustain the redox transitions completely at higher scanning rates.	178 (5 mV s^{-1})	[102]
11	α-$LiFeO_2$ in nanosized or micrometric form		50 for nanosized α-$LiFeO_2$ (10 mV s^{-1})	[103]
12	Electroplated magnetite (Fe_3O_4)	In Na_2SO_3, the capacitive current of magnetite electrode originates from the combination of EDLC and the pseudocapacitance that involves successive reduction of the specifically adsorbed sulfite anions, from SO_3^{2-} through, e.g., S^{2-}, and vice versa.	170 in Na_2SO_3	[104]

2.1.2.2 Conducting polymer

Another major type of electrode material for a pseudocapacitor is the conducting polymer (CP). CPs are rendered conductive through a conjugated bond system along the polymer backbone [105]. The conductivities of popular CPs are listed in Table 2.5. In addition to high conductivity, CPs enable fast charge/discharge kinetics and fast doping and de-doping processes [106]. The simplified charge/discharge mechanisms of *p*-doped and *n*-doped CPs can be described as the following reactions:

$$Cp \leftrightarrow Cp^{n+}(A^-)_n + ne^- \qquad (p\text{-dope}) \tag{2.4}$$

$$Cp + ne^- \leftrightarrow (C^+)_n Cp^{n-} \qquad (n\text{-dope}) \tag{2.5}$$

where Cp is conducting polymer, A^- is anion, and C^+ is cation.

Table 2.5 Typical conductivities of various CPs [105].

Polymer name	Conductivity / S cm^{-1}	Reference
Polyaniline	0.1-5	[107]
Polypyrrole	10-50	[108]
poly(3,4-ethylenedioxythiophene)	300-500	[109]
Polythiophene	300-400	[109]

Polyaniline

As shown in Figure 2.2, polyaniline (PANI) consists of phenyl diamine and quinine diimine repeating units. The reasons that PANI can be a promising candidate for fabricating SCs with high electroactivity, high doping level, excellent stability, environmental stability, easy processability, and controllable electrical conductivity [110-112].

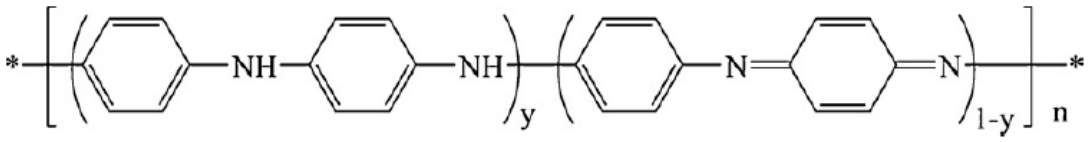

Figure 2.2 Chemical structure of intrinsic polyaniline, *y* is between o and 1, *n* is integer.

According to multiple reports, PANI SCs have a wide capacity range from 44 to 270 mAh g^{-1}. The wide range comes from the factors including different synthetic routes, polymer morphology, the amount and type of binders and additives, and the thickness of the electrodes. Among the conducting polymer SCs, those based on PANI have the most variable specific capacitance, indicating all those factors listed above have a huge impact on the performance.

Similarly as the carbon based materials and the metal oxides, CPs in their nano-size form have high surface area and high porosity. Therefore the synthesis and application of nano-sized PANI such as nanotubes and nanowire have been extensively studies. Dhawale et al. have presented a one-step, template-free and seedless method for growing nano-structured PANI electrodes [113]. The PANI has a nano-grained structure with an average diameter of 20-30 nm. Specific capacitance value of 740 F g^{-1} was obtained for PANI nanotube structures (measured at charge/discharge rate of 3 A g^{-1}) with 13% loss in specific capacitance over 1,100 cycles. Titanium nanotube template was employed by Mujawar et al. in synthesizing hollow open ended PANI nanotubes [114]. The open ended nano-structured polymers can provide intrinsically high surface area, leading to high charge/discharge capacities and short diffusion distances for ion transport. PANI can also be co-electrodeposited with MnO_x as hybrid films in a nano-fibrous structure [115]. The addition MnO_x of could change the morphology and the pseudocapacitive properties of PANI. Hybrid film obtained from the solution of 0.1 mol L^{-1} aniline and 120×10^{-3} mol L^{-1} Mn^{2+} showed a specific capacitance of 588 F g^{-1} measured at 1.0 mA cm^{-2} in 1 mol L^{-1} $NaNO_3$, increasing 44% from that of similarly prepared PANI (408 F g^{-1}). The film maintained more than 90% percent of its capacitance after 1,000 charge/discharge cycles at 2.4 mA cm^{-2}.

Polypyrrole

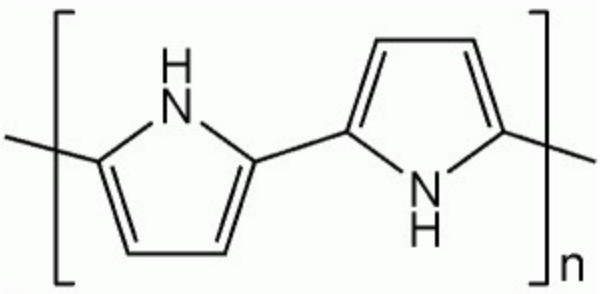

Figure 2.3 Chemical structure of polypyrrole.

As illustrated in Figure 2.3, PPy is a polymer formed from a number of pyrrole ring structures. PPy offers a greater degree of flexibility in electrochemical processing than most other conducting polymers [108]. However, due to the fact that PPy cannot be *n*-doped, they can only be used as cathode materials.

Several methods have been proposed to improve PPy chain structures for application in SCs, including the development of columnar morphology, self-doping by attachment of ions, and use of aryl sulfonates to promote cross linking and hydrophilicity [116]. Among them, enhancing the electrical conductivity and increasing the hydrophilicity of the polymer structure for larger area is the key issue for application in SCs [117]. Pulsed polymerization was used by Sharma et al. to synthesize PPy films [118]. Supercapacitor device made by pulse PPy films exhibited high specific capacitance of 400 F g^{-1} with a high energy density of 250 Wh kg^{-1} in comparison to the DC polymerized PPy (~225 F g^{-1}) in aqueous electrolyte. The stability of the pulsed polymerized electrodes for 10,000 charge/discharge cycles at 5 mA cm^{-2} supports the applicability of the pulsed polymerization process for the electrodes. PPy/carbon aerogel were frequently found in use as photovoltaic materials, but they can also be used as electrode material for SCs

[119]. Results showed that in addition to EDL capacitance, the PPy/carbon areogel SCs possess pseudocapacitance. The specific capacitance of the 35% PPy/carbon areogel composite electrode in 6 mol L^{-1} KOH is approximately 433 F g^{-1}. The dense growth of PPy leads to high capacitance per unit volume (400-500 F cm^{-3}) [120]. However, one disadvantage of the high density is that it causes limited access to the interior sites of the polymer by the dopant ions, which will reduce the utilization of the material.

Single-charged anions such as Cl^-, ClO_4^-, and SO_3^- were normally used to be doped PPy. But if anions with more than one charge such as SO_4^{2-} doped the PPy, physical cross-linking of the polymer occurs [121]. SCs with such cross-linked materials have high diffusivity, high capacitance, minimum volumetric change, and strong cation exchange.

Thiophene-based conducting polymers

Thiophene-based conducting polymers have attracted attention because of their high charge carrier mobility and environmental stability [122]. A number of *n*-dopable thiophene based conducting polymers can be found in Table 2.6. Polythiophene are commonly synthesized by chemical [123], electrochemical [124], ultrasonic assisted electrochemical [125], photochemical [126], and template synthesis methods [127].

Table 2.6 Properties of derivatives of polythiophene in p-doped state [128].

Active material	Potential limit (V) vs. Ag|AgCl	Specific charge (C g^{-1})	Specific capacitance (F g^{-1})
P-PFPT	0.3-0.9	146	244
P-MPFPT	0.3-0.9	127	212
PThCNVEDT	0-0.8	173	216
P-MeT	-0.16-1.18	-	220
PEDOT	-0.5-0.9	144	103
Carbon	-1.5-2.1	82	133

Oxidants and surfactants were used to enhance the thermal, electrical and electrochemical properties of polymers [129]. Senthilkumar et al. synthesized polythiophene by iron (III) catalyzed oxidative polymerization method in aqueous medium using various surfactants [130]. Polythiophene prepared using anionic surfactants was spherical-like, and the specific capacitance was 117 F g^{-1}.

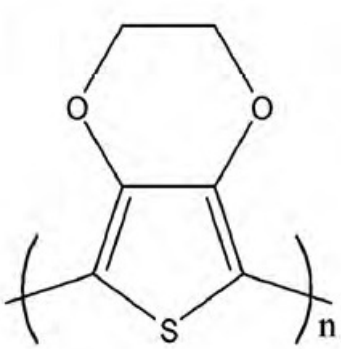

Figure 2.4 Structure of poly(3,4-ethylenedioxythiophnen).

One popular thiophene derivative is poly(3,4-ethylenedioxythiophnen) (PEDOT). The structure of PEDOT can be seen in Figure 2.4. PEDOT has a low band-gap of 1-3 eV, is highly conducting in the *p*-doped state, has good thermal and chemical stability, and high charge mobility [105]. Furthermore, PEDOT has low redox potential and fast redox reactions. The charge reactions of PEDOT were reported to be faster than the discharge reactions during the electrochemical charge/discharge [131].

PEDOT/carbon composite as electrodes for SCs was found to have high energy and power density [132,133]. PEDOT/carbon composite can be synthesized *in situ* on carbon materials by electrochemical or chemical-polymerization from the monomer. The electrodes prepared by this method have higher conductivity than those prepared by mechanically blending methods.

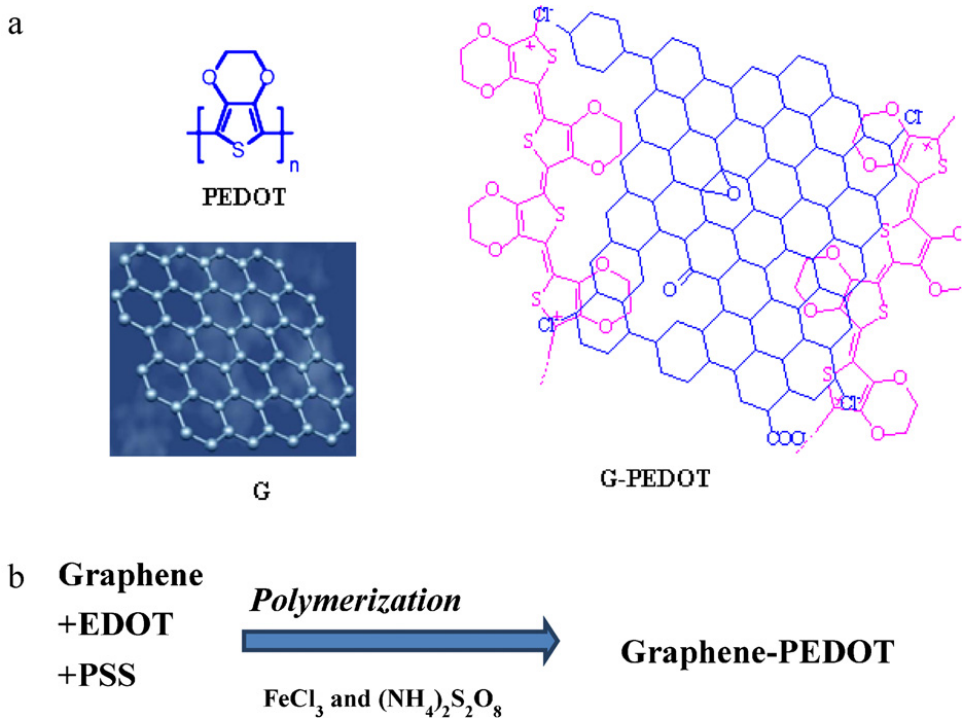

Figure 2.5 (a) Schematic structures of graphene, PEDOT and G-PEDOT (Scheme 1); (b) Schematic of synthesis of G-PEDOT (Scheme 2).

Alvi et al. have prepared Graphene-PEDOT (shown in Figure 2.5) electrodes for SC application [134]. The Graphene-PEDOT electrode has shown a large current in charging due to high charge mobility and immense conductivity. The average specific capacitance was reported to be 350 F g^{-1}.

2.1.3 All-solid-state supercapacitor

All forms of supercapacitors list in Sections 2.1.1 and 2.1.2 are liquid electrolyte based supercapacitors. Although all-solid-state supercapacitors have many obvious advantages over liquid electrolyte based supercapacitors including no leaking, no corrosion, easy packaging, wide temperature range, light weight, and shape flexibility, efforts on developing all-solid-state supercapacitors were rare and not successful suffering from low specific power and energy. The accounts for these efforts present in literature are

summarized in Table 2.7. The maximum specific power and energy was only 0.25 kW kg^{-1} and 9 Wh kg^{-1} respectively.

Table 2.7 A summary of the performance of the existing all-solid-state supercapacitors.

Supercapacitor device	Specific capacitance (F g^{-1})	Specific power (kW kg^{-1})	Specific energy (Wh kg^{-1})	Reference
Ppy(DS)/PMMA+$LiClO_4$+EC/Ppy(DS)	20-60	0.2	3	[135]
$H_3PMo_{12}O_{40}\cdot nH_2O$/Nafion/$HRuO_2\cdot nH_2O$	112	0.2	3	[136]
$HRuO_2\cdot nH_2O$/Nafion/ $HRuO_2\cdot nH_2O$	170		5.5	[137]
PANI/FEP-g-AA-SO_3H/PANI	98	0.25	5.0	[138]
Activated carbon/Nafion+PVDF/Activated carbon	90-130		3.8-5.4	[139]
PANI/EC+LiF/PANI	90	0.15	3.8	[140]
RuO_2/LiPON/RuO_2/Pt	0.02			[141]
PANI/phosphotungsten acid/PANI	260	0.16	9.0	[142]
Pyrrole/Nafion/Pyrrole	35	0.0037	3.4	[143]

2.2 Experimental methods for SC studies

2.2.1 Electrochemical measurements

2.2.1.1 Cyclic voltammetry

Cyclic voltammetry (CV) is a quick screening procedure for identifying potential capacitor materials [22]. In CV tests, the voltage is swept between two values at a constant scanning rate ($s = \pm dV/dt$). The resulting current (I) is recorded as a function of time. For an ideal EDLC, the shape of the CV is rectangular, indicating that the current is independent of the potential. The capacitance is determined as $C = I/s$. However, for those non-ideal EDLCs and pseudocapacitors, the rectangular shape is distorted. In these cases, the current, $I(t)$,is a function of time, and the capacitance is determined as $C = \int I(t)dt$. CV has become a major method for evaluating performance of SCs because it is convenient for determining the cycle life [144]. In addition, through an

analysis of the shapes of the voltammograms as a function of *s*, the information on internal resistance effects and the consequent dissipative losses can be revealed.

2.2.1.2 Galvanostatic charge/discharge

Galvanostatic charge/discharge (GCD) is also known as constant current charge/discharge. In GCD experiments, the device is charged and then discharged at constant currents in a preset potential range. The following combinations are also applied according to different experiment needs [22]:

1. Charge at a constant current followed by immediate discharge across various load resistors. These tests are used to analyze the electrochemical performance such as specific capacitance, specific power, and specific energy.
2. Charge at a constant current followed by an open circuit holding period while recording the open circuit voltage of the device. Self-discharge can be studied with this method.
3. Charge at various rates and discharge across a fixed load resistor.

The capacitance, power, and energy can be calculated through integration of the voltage time transients according to:

$$C = \frac{I\Delta t}{\Delta V} \tag{2.6}$$

$$E = I \int V(t)dt \tag{2.7}$$

$$P = \frac{E}{\Delta t} = \frac{I \int V(t)dt}{\Delta t} \tag{2.8}$$

where I is constant current, $V(t)$ is voltage as a function of time, and Δt is the time interval for charge or discharge.

2.2.1.3 Electrochemical impedance spectroscopy

Electrochemical impedance spectroscopy (EIS) is normally used by corrosion specialists and electrochemical device researchers. It is a powerful and nondestructive method that can be used to differentiate different processes and evaluate the kinetics of the systems under investigated [145]. In the evaluation of an SC, the frequency-response characteristics of an SC and its equivalent series resistance are very important [22].

EIS data can be displayed in either Bode plot or Nyquist plot. In the Bode plot, the real and imaginary parts of the impedance can also be plotted against frequency on a log-log scale. In the Nyquist plot, the imaginary part is plotted against the real part of the impedance. The interpretation of the EIS data depends on a model of equivalent circuit. Identifying an appropriate equivalent circuit to fit the EIS data can be a difficult task.

2.2.2 Instrumental characterization methods

Scanning electron microscope (SEM) and X-ray diffraction (XRD) have been employed to characterize the electrode materials.

2.2.2.1 Scanning electron microscope

SEM images a sample by scanning it with a high-energy beam of electrons in a raster scan pattern. The SEM is able to show very detailed 3-dimensional images at much higher magnifications than those from a light microscope. Samples, at least the surface of the samples, for SEM examinations, have to be electrically conductive and grounded to prevent the accumulation of electrostatic charge at the surface. For nonconductive

samples, certain pretreatment such as coating with a very thin layer of gold has to be done to prevent charge accumulation at the surface.

SEM is commonly used in studying the micro- or nano-structures of the active materials of various SCs in the nano scale [146]. SEM is also able to provide information on the dispersion of the active materials in the supporting materials [147].

2.2.2.2 X-ray diffraction

XRD is a versatile, non-destructive method that reveals detailed information about the chemical composition, crystallographic and micro structure of all types of natural and manufactured materials. The following needs can be fulfilled by XRD: 1) measure the average spacing between layers or rows of atoms; 2) determine the orientation of a single crystal or grain; 3) find the crystal structure of an unknown material; 4) measure the size, shape and internal stress of small crystalline regions [148].

For polymer electrolytes and polymer membranes, the information about the molecular structure and atom arrangement can be obtained from XRD. In this way, the atomic models for these polymer electrolytes or membranes can be established [149].

2.2.3 *In situ* study using X-ray absorption spectroscopy

To gain deep fundamental understanding of the electrochemical reactions at the electrode/electrolyte interface and between mediators requires not only electrochemical measurements including CV, EIS, and dynamic polarization, but also *in situ* and *ex situ* physiochemical analyses. With respect to this, *in situ* methods are generally preferred to *ex situ* methods because the *ex situ* methods can only detail the consequence of a prior

polarization but not the state at the polarization. However, to my knowledge, research on *in situ* analysis of supercapacitors has been very limited.

X-ray absorption spectroscopy (XAS) is a powerful technique that provides element-specific short range structural information. It can be applied to structurally ordered, disordered, aggregated, and dispersed substances/species. It is well-known that one of the major advantages of XAS is that it can be readily performed under polarization conditions.

X-ray absorption edges were first observed by DeBroglie in 1916 [150]. Advances in the following years were reported by Van Nordstrand [151] in exploiting edges and by Sayers, Stern and Lytle [152] who demonstrated that the fine structure could be understood by Fourier transformation. A typical XAS experimental system such as X-10C at National Synchrotron Light Source (NSLS) in Brookhaven National Laboratory is shown in Figure 2.6. The synchrotron X-ray beam passes through slits, a crystalline monochromator for tuning the photon energy (0.1-100 keV), and a mirror to reach the sample. The beam intensities before and after the sample are measured.

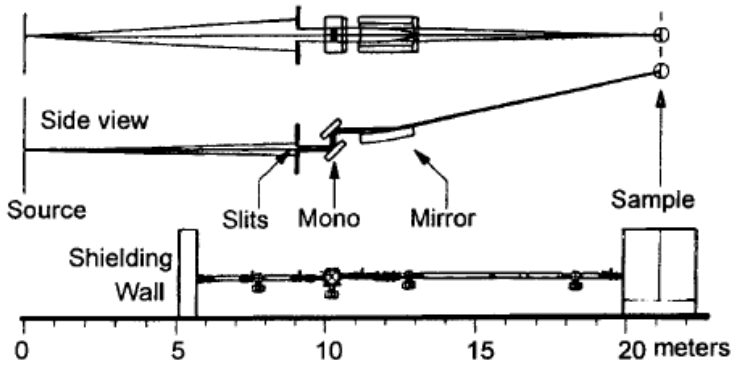

Figure 2.6 Experimental setup for XAS study of a sample.

The principle of XAS is schematically illustrated in Figure 2.7. A narrow parallel monochromatic X-ray beam of intensity I_0 passing through a sample of thickness x will get a reduced intensity I according to the expression:

$$\mu(E) = \frac{1}{x}\ln\left(\frac{I_0}{I}\right) \tag{2.9}$$

where $\mu(E)$ is the linear absorption coefficient, which depends on E, the X-ray photon energy, the types of atoms, and the density ρ of the material. Figure 2.8 illustrates schematically a XAS. At certain energies where the absorption increases drastically, and gives rise to an absorption edge at $E=E_0$. Each such edge occurs when the energy of the incident photons is just sufficient to cause excitation of a core electron of the absorbing atom to a continuum state, i.e. to produce a photoelectron. Thus, the energies of the absorbed radiation at these edges correspond to the binding energies of electrons in the K, L, M, etc, shells of the absorbing elements. The absorption edges are labeled in the order of increasing energy, K, LI, LII, LIII, MI,…., corresponding to the excitation of an electron from the 1s (2S½), 2s (2S½), 2p (2P½), 2p (2P3/2), 3s (2S½), … orbitals (states), respectively.

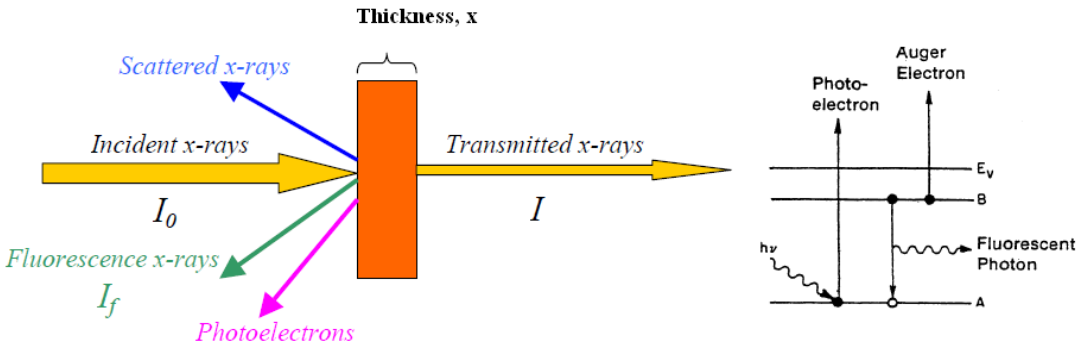

Figure 2.7 Schematic illustration of the principle of XAS.

An XAS is generally divided into 4 sections: 1) pre-edge ($E < E_0$); 2) x-ray absorption near edge structure (XANES), where the energy of the incident x-ray beam is $E = E_0 \pm 10$ eV; 3) near edge x-ray absorption fine structure (NEXAFS), in the region between 10 up to 50 eV above the edge; and 4) extended x-ray absorption fine structure (EXAFS), which starts approximately from 50 eV and continues up to 1,000 eV above the edge.

Probably the first XAS studies of supercapacitors based on pseudocapacitance was the work by Chang et al. [153]. Their experimental results clearly demonstrate that the reduction/oxidation state of the active material, MnO_x, in a liquid electrolyte supercapacitor is a linear function of polarization of the supercapacitor. Chang's group also studied the charge storage mechanism of electrodeposited MnO_x in various aprotic ionic liquids (ILs) [154]. The analytical results show that thiocyanate (SCN^-) anion can reversibly insert/desert into/from the tunnels between the [MnO_6] octahedral subunits depending on the applied potential. This insertion/desertion process compensates or neutralizes the space charge originating from Mn^{3+}/Mn^{4+} redox transition in the electrode upon charge/discharge. This actually gives rise to a fast charge/discharge or an ideal pseudocapacitive behavior of the MnO_x electrode.

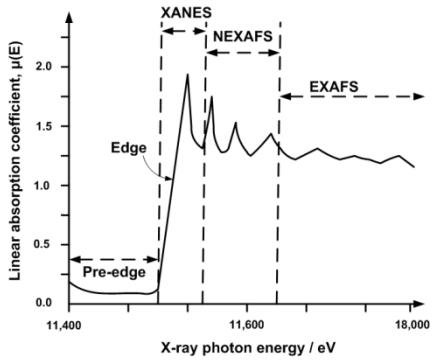

Figure 2.8 Schematic illustration of the ranges of a XAS.

Watanabe et al. [155] designed an electrochemical cell for *in situ* XAS study of electrochemical power systems including supercapacitors. Specifically, they used XAS to monitor the chemical state of Co or Co^{2+} insertion in a conducting polymer, PPy. The EXAFS they obtained reflects the average radial distribution function around Co atoms. At -0.60 V, the peak at around 1.3 Å is related to a Co-O distance. This peak could also be associated to a Co-N distance due to the similarity of the backscattering amplitudes and phase shifts of both elements. At -0.80 V, there is a small contribution of the light elements (O/N) and Co-Co distances show up. At this potential, one observes distances characteristic of next-nearest neighbors (higher than 3 Å), indicating medium range order of the atomic shells. Finally, at -1.20V, there are only Co-Co distances indicating that Co is completely reduced.

There have been more reports on *in situ* XAS study of Li ion batteries. Chan et al. studied $LiMn_2O_4$ for Li-ion battery and correlated the Mn-O and Mn-Mn bonding lengths with the applied potential [156]. Nam et al. studied $LiFe_{1/4}Mn_{1/4}Co_{1/4}Ni_{1/4}PO_4$ cathode using *in situ* XAS. They found that the three plateaus shown in the charge curve can be ascribed to redox specific reactions: Fe^{2+}/Fe^{3+}, Mn^{2+}/Mn^{3+}, and Co^{2+}/Co^{3+}. However, Balasubramanian et al. studied a $LiNi_{0.85}Co_{0.15}O_2$ cathode in a Li-ion battery [157]. They found the redox state did not correlate with the charge/discharge states. Deb et al. $Li_{1.05}Ni_{0.35}Co_{0.25}Mn_{0.4}O_2$ cathode material coated with $LiCoO_2$ [158]. The XAS data revealed that the distances between the metal and oxygen and between the metal atoms varied with the charge/discharge states almost reversibly. In summary, *in situ* XAS can provide the information regarding to redox state, bonding, and molecular structure of the electrode in the supercapacitors and Li-ion batteries.

2.2.4 Electrochemical scanning tunneling microscopy

Unlike other techniques for imaging materials in atomic scale, the principle of STM is remarkably simple as shown in Figure 2.9. A bias voltage is applied between a sharp metal tip and a conducting sample to be investigated (usually metals and semiconductors) [159]. Then, bringing tip and sample surface within a separation of only a few angstroms unit, a tunneling current can flow due to the quantum mechanical tunneling effect before 'mechanical point contact' between the tip and sample. If the tunneling current is maintained was a constant when the tip is scanning over the surface by means of a feedback loop, separation between the tip and sample surface will be tightly controlled as a constant due to the fact that the current is very sensitive to the separation. Thus, by monitoring the position normal to the surface, a 3-D image of the surface can be obtained. This scanning principle results in a unique microscopy:

1) STM is free from image distortion due to aberration of a lens system that exists for other microscopy methods.
2) The spatial resolution is not diffraction-limited. The spatial resolution is even smaller than the wavelength of electron. Under certain conditions, STM can reveal features within one atom or the electron orbitals.
3) Due to a low energy (in eV level in comparison to MeV level for SEM, TEM, SIMS, etc.) the method is absolutely non-destructive.
4) STM can be operated well in vacuum, air, and liquid. If the liquid is an electrolyte and the electrochemical potential of the sample can be controlled with a potentiostat, the STM is also called electrochemical STM or EC STM.

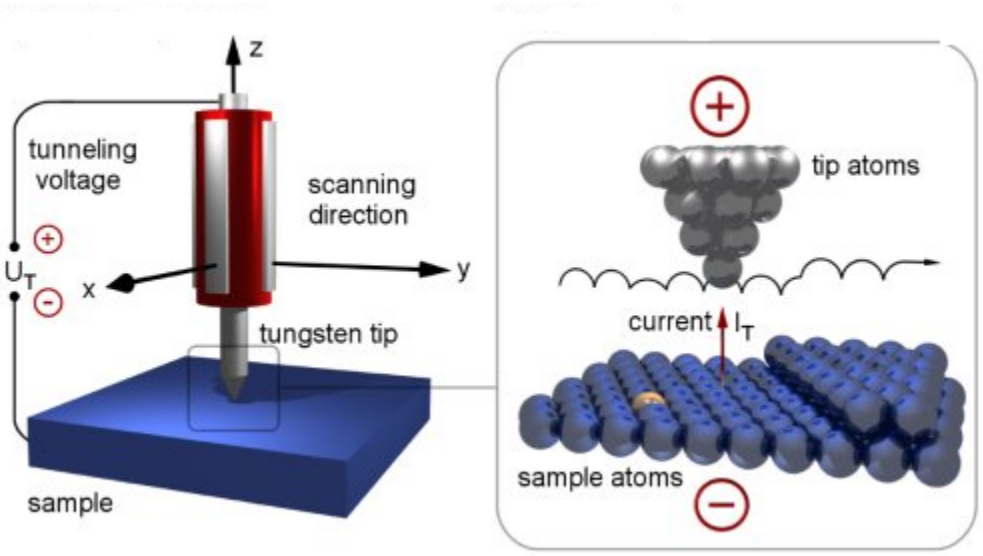

Figure 2.9 Schematic illustration of the operational principle of a STM.

Electron Tunneling

In classical physics an electron cannot penetrate into or across a potential barrier if its energy E is smaller than the potential Φ within the barrier. A quantum treatment predicts an exponential decaying solution for the electron wavefunction in the barrier (Figure 2.10). For a rectangular barrier the wavefunction is [159]:

$$\Psi(d) = \Psi(0)e^{-\kappa d} \qquad where\ \kappa = \frac{\sqrt{2m(\Phi - E)}}{\hbar} \tag{2.10}$$

The probability of finding an electron behind the barrier of the width d is

$$W(d) = |\Psi(d)|^2 = |\Psi(0)|^2 e^{-2\kappa d} \tag{2.11}$$

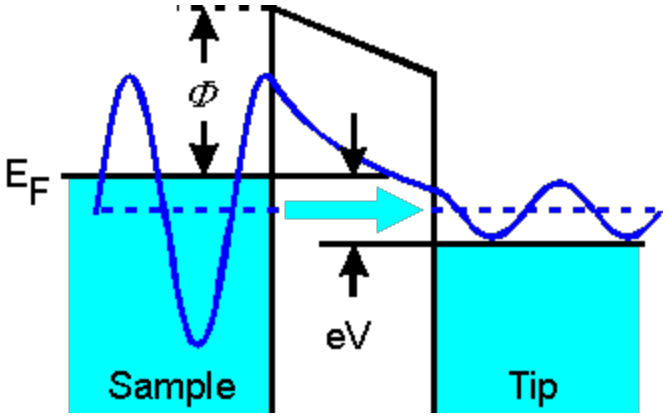

Figure 2.10 Mechanism of electron tunneling.

In STM a small bias voltage V is applied so that due to the electric field the tunneling of electrons results in a tunneling current I. The height of the barrier can roughly be approximated by the average workfunction of sample and tip.

$$\Phi = \frac{1}{2}(\Phi_{sample} + \Phi_{tip}) \tag{2.12}$$

If the voltage is much smaller than the workfunction eV <<Φ, the inverse decay length for all tunneling electrons can be simplified to

$$\kappa \approx \frac{\sqrt{2m\Phi}}{\hbar} \tag{2.13}$$

The current is proportional to the probability of electrons to tunnel through the barrier:

$$I \propto \sum_{E_n=E_F-eV}^{E_F} |\Psi_n(0)|^2 e^{-2\kappa d} \tag{2.14}$$

By using the definition of the local density of states for $\mathcal{E} \to 0$

$$\rho(z,E) \equiv \frac{1}{\varepsilon}\sum_{E_n=E-\varepsilon}^{E} |\Psi_n(z)|^2 \tag{2.15}$$

The tunneling current can be expressed by

$$I \propto V\rho_{sa}(0, E_F)e^{-2\kappa d} \approx V\rho_{sa}(0, E_F)e^{-1.025\sqrt{\Phi}d} \quad where\ [d] = \text{Å};\ [\Phi] = eV \qquad (2.16)$$

With 5 eV as typical example for a workfunction value a change of 1 Å in distance causes a change of nearly one order of magnitude in current. This facilitates the high vertical resolution.

EC STM vs. SECM in probing electrochemical interfaces in liquid electrolyte

The broad application of scanning probe techniques such as electrochemical scanning tunneling microscopy (EC STM) have contributed significantly to a microscopic (atomistic) understanding of reactivity of solid/liquid electrodes [159-160]. The most detailed pictures could be obtained for ion-transfer and phase formation reactions at single crystal noble metal electrodes [161]. The main reason is that EC STM is able to localize electrochemical reactivity only if this is accompanied by changes in sample topography, e.g. by concurrent deposition, adsorption or dissolution reactions. Parallel to the advance of EC STM, scanning electrochemical microscopy (SECM) was developed as a new tool for localized electrochemistry [162-165]. It shares the scanning principle with EC STM but it can be distinguished from EC STM by an entirely different mode of action. Hence SECM can provide complementary information. Currently strong efforts are under way to increase the resolution of SECM and to access the nanometer size regime because many electrochemical phenomena are localized at much smaller structures [166-169]. Important applications include initiation of pitting corrosion [166], mass transport though membranes [169], and fuel cell optimization, where catalytic reactions proceed at noble metal clusters [167,170]. In order to allow SECM

measurements in the nanometer dimension, a number of technical challenges have to be overcome. Firstly, suitable nanometer-sized electrodes must be prepared that have insulating shielding preferably of known geometry. The probes must be positioned and scanned above the sample with a sample distance of some 10 nm, i.e. much larger than the tunneling distance but smaller than some electrode radii of the probe, while avoiding mechanical contact between sample and probe. Secondly, in order to observe electrochemical reactivity at individual nanometer-sized features, such features have to be prepared on the sample surface with such a large distance that SECM can resolve the signals of individual features. In order to achieve the last point it is advantageous to make use of various probe-induced mechanisms to modify solid/liquid interfaces [160,162,165].

Previous approaches used commercial STM instruments to adjust the sample with extremely small tilt with respect to the horizontal scanning plane and to acquire a reference point for the sample position. The probe was then retracted and scanned in a fixed plane over the sample using the generation/collection mode which can work at larger probe sample separations than the feedback mode [166-167]. However, it is very difficult to exclude the possibility of mechanical contact between the probe and protruding regions of the sample. The problem of protruding features was circumvented in the approach of Meier et al. who positioned the probe in the EC STM mode over a protruding sample and retracted the tip from there [170]. The electrochemical data were recorded in the generation/collection mode at fixed probe position. Combined topographical and electrochemical imaging was performed on samples that were not immersed in a bulk solution but wetted through pores [169]. Noncontact imaging was also performed in generation/collection and feedback modes at sub-merged samples [168].

Although EC STM can be used to study the interfaces between an electronic conductor and electrolyte, all studies as far as I know were conducted in bulk of liquid electrolytes. There has been no study on the interface between an electronic conductor and bulk polymer electrolyte. The reasons are very simple: 1) if the STM probe that as sharp as having one atom at the tip touches a solid, it will lose its high spatial resolution and 2) traditional understanding is that tunneling current (in the level of nA) can be detectable only when the STM tip is a few angstroms from the surface of the electronic conductor. Thus, if the electrolyte film on top of an electronic conductor is thicker than a few nanometers, traditional understanding is that this sample cannot be studied using a STM, not even mention if the electrolyte film is hundreds of nanometer thick.

2.5 Fundamentals of Atomistic Modeling

2.5.1 *Ab initio* modeling of materials

2.5.1.1 Adiabatic approximation

The basis of *ab initio* modeling of materials is the time-independent Schrödinger equation in which the state of a molecular system is described with a wavefunction:

$$H(\{\vec{r}\},\{\vec{R}\})\Psi(\{\vec{r}\},\{\vec{R}\}) = E(\{\vec{R}\})\Psi(\{\vec{r}\},\{\vec{R}\}) \tag{2.17}$$

where $H(\{\vec{r}\},\{\vec{R}\})$ is a Hamailtonian of a many-ion-many-electron system with n electrons and N nuclei, $\Psi(\{\vec{r}\},\{\vec{R}\})$ is the wavefunction, $E(\{\vec{R}\})$ is energy, $\{\vec{r}\}$ are the position vectors of electrons, and $\{\vec{R}\}$ are the position vectors of ions [171]. The first step towards simplification and solutions of the Schrödinger equation is the adiabatic or Born-Oppenheimer (BO) approximation that separates slow nuclear motion from fast electronic

motion. In order to do this, one has to assume that irrespective of the instantaneous configuration of the ions, the electrons are at every moment in their ground state. The system is described by two effective Hamiltonians, shown in Equation 2.18 and Equation 2.19:

$$H_{elec} = \sum_{i=1}^{n}\left[-\frac{\hbar}{2m}\frac{\partial^2}{\partial \vec{r}_i^{\,2}} + \sum_{l=1}^{N} V_{el-ion}(\vec{r}_i, \vec{R}_l)\right] + \frac{1}{2}\sum_{i}^{n}\sum_{j\neq i}^{n}\frac{e^2}{\left|\vec{r}_i - \vec{r}_j\right|} \tag{2.18}$$

for electrons and

$$H_{ion} = \sum_{I=1}^{N}\left[-\frac{\hbar}{2M_I}\frac{\partial^2}{\partial \vec{R}_I^{\,2}}\right] + \frac{1}{2}\sum_{I=1}^{N}\sum_{J\neq I}^{N} V_{ion-ion}(\left|\vec{R}_I - \vec{R}_J\right|) + E_{tot}(\left\{\vec{R}_I\right\}) \tag{2.19}$$

for ions, where $\vec{r}_i$ is the position vector for the i[th] electron, $\vec{R}_I$ is the position vector for the i[th] ion, m is the mass of electron, M_I is the mass of the i[th] ion, e is electronic charge, V_{el-ion} is potential for the direct electron-ion interaction, $V_{ion-ion}$ is potential for the direct ion-ion interaction, and E_{tot} is the electronic total energy as a function of the ionic coordinates $\{R_I\}$.

2.5.1.2 Hatree-Fock approximation and single electron Hamiltonian

Under the Hartree-Fock (HF) approximation, the function of 3n variables for the solutions of the electronic Hamiltonian is reduced to n functions, which are referenced as molecular orbitals (MOs), each dependent on only three variables. The HF theory is to approximate the many-electron wavefunction by an antisymmetrized product of one-electron wavefunctions and to determine these wavefunctions by a variational condition applied to the expected value of the Hamiltonian in the resulting one-electron equations,

$$\left(\sum_{i=1}^{n}\left[-\frac{\hbar}{2m}\frac{\partial^2}{\partial\vec{r}_i^{\,2}}+\sum_{l=1}^{N}V_{el-ion}(\vec{r}_i,\vec{R}_l)\right]+\frac{1}{2}\sum_{i}^{n}\sum_{j\neq i}^{n}\frac{e^2}{|\vec{r}_i-\vec{r}_j|}\right)\psi_i(\vec{r})-\sum_j\delta_{S_iS_j}\int\frac{\psi_j^*(\vec{r}')\psi_i(\vec{r}')}{|\vec{r}-\vec{r}'|}d\vec{r}'\psi_j(\vec{r})=\varepsilon_i\psi_i(\vec{r})$$

(2.20)

where the pair-wise electron-electron repulsion is replaced by the interaction of the ith electron with the average electrostatic field created by the charge distribution of all other electrons and an additional exchange term keeping electrons of like spin ($S_i = S_j$) away from each other to account for the Pauli principle.

2.5.1.3 Density function theory

Directly solving the HF equations is difficult and time consuming. For analyzing many quantum chemical problems, a density function theory (DFT) is often employed. DFT methods are based on the famous theorem by Hohenberg and Kohn who demonstrated that the total energy of a many-electron system in an external potential is a unique functional of the electron density and that this functional has its minimum at the ground-state density [172]. Expressing the electron density $n(r)$ as a sum over one-electron densities $|\psi(\vec{r}_i)|^2$ and using the one-electron wavefunctions as the variational parameters leads to the Kohn-Sham one-electron equations as follows:

$$\left[-\frac{\hbar}{2m}\frac{\partial^2}{\partial\vec{r}^{\,2}}+\sum_{l=1}^{N}V_{el-ion}(\vec{r}_i,\vec{R}_l)+e^2\int\frac{n(\vec{r}')}{|\vec{r}-\vec{r}'|}d\vec{r}'+V_{XC}(\vec{r})\right]\psi_i(\vec{r})=\varepsilon_i\psi_i(\vec{r}) \tag{2.21}$$

$$n(\vec{r})=\sum_{i}^{n}|\psi_i(\vec{r})|^2,\quad V_{XC}(\vec{r})=\frac{\delta E_{XC}[n(\vec{r})]}{\delta n(\vec{r})} \tag{2.22}$$

where the exchange-correlation potential has been expressed as the functional derivative of the exchange-correlation energy. While Equation 2.21 is exact within DFT, the energy functional $E_{XC}\left[n(\vec{r})\right]$ is usually unknown [173].

2.5.1.4 *Ab initio* quantum chemistry computation

The most important feature of the *ab initio* quantum chemistry computation is the capability of describing the breaking and formation of chemical bonds, chemical reactions, or electron transfer. Although a few modern quantum mechanics methods including generalized valence bond (GVB) and Gaussian dual space density function theory (GDS-DFT) are available, the calculation are often too slow for studying polymers and catalysts [174-177].

2.5.1.5 *Ab initio* Molecular Dynamics

Another challenge for quantum mechanics theories is to compute the dynamic properties or to model the physicochemical processes of a system by solving the equations of motion based on the adiabatic Hamiltonian of the ionic subsystem (Equation 2.19).

In 1985, Car and Parrinello introduced a very useful concept that the optimization with respect to the ionic and electronic degrees of freedom need not be done separately. In this concept or theory, one can use a coupled set of pseudo-Newtonian equations of motion for the ionic coordinates $\{R_I\}$ and the electronic orbitals $\{\psi_i\}$ as follows to determine the motion and electronic states:

$$M_I \ddot{\vec{R}}_I(t) = -\frac{\partial E(\{\vec{R}_I\},\{\psi_i\})}{\partial \vec{R}_I(t)} \tag{2.23}$$

and

$$m\ddot{\psi}_i(t) = -\frac{\partial E(\{\vec{R}_I\},\{\psi_i\})}{\partial \psi_i^*(t)} + \sum_{i,j} \Lambda_{ij}(\langle \psi_j | \psi_i \rangle - \delta_{ij}) \qquad (2.24)$$

where the Lagrange multipliers Λ_{ij} are used to ensure conservation of orthonormality of the $\{\psi_i\}$ during the dynamical evolution of the system [178].

2.5.2. Classical molecular dynamic modeling

Quantum molecular dynamics (MD) simulations can usually treat 10^3-10^5 atoms in a real time of a few nanoseconds. In a MD method, a molecular system is described with the Newton's laws. However, although the total energy of the system is not a functional of electronic wavefunctions and is expressed explicitly as a function of the nuclear or ionic positions as $U(\vec{R}_1, \vec{R}_2, ..., \vec{R}_N)$, it is usually evaluated using the *ab initio* methods. Thus, the atoms are treated as classical particles moving on the Born-Oppenheimer potential energy surface (PES) where $U(\vec{R}_1, \vec{R}_2, ..., \vec{R}_N)$ equals to a constant, and the quantum mechanical motion governed by the Schrödinger equation is replaced by Newton's second law:

$$\vec{F}_i = m_i a_i \qquad (2.25)$$

where m_i is the mass of the ith atom, a_i is the acceleration of the ith atom, and $\vec{F}_i$ the resultant force acting on the ith atom. The force is calculated from the interatomic potential energy according to Equation 2.26,

$$\vec{F}_i = -\frac{\partial U}{\partial \vec{R}_i} = -\nabla_i U \tag{2.26}$$

Two primary aspects to the practical implementation of molecular dynamics are: (i) the numerical integration of the equations of motion along with the boundary conditions and any constraints on the system and (ii) the choice of the interatomic potential. For a single-component system, the potential energy can be written as an expansion in terms of *n*-body potentials:

$$U(\{\vec{R}_i\}) = \frac{1}{2!}\sum_{i \neq j} U_2(\{\vec{R}_{ij}\}) + \frac{1}{3!}\sum_{i \neq j \neq k} U_3(\{\vec{R}_{ij}\},\{\vec{R}_{ik}\},\{\vec{R}_{jk}\}) + \ldots \tag{2.27}$$

where $\vec{R}_{ij} = \vec{R}_i - \vec{R}_j$ are inter-atomic separations and U_2 represents interactions between pairs of atoms, U_3 depends on the relative orientations of triplets of atoms, etc. The choice of potential is determined by the bond type, the desired accuracy, transferability and the computational resources [179]. Quantum mechanical calculations can give a guide to obtain an ideal molecular force field. For example, Goddard et al developed DREIDING force field [180]. They claimed that the force field can be used to predict structures and dynamics of organic, biological, and several main-group inorganic molecules.

For all MD force fields, the parameters are determined by quantum chemical calculations or by fitting to thermo-physical and phase coexistence data. There are two major limitations for MD simulation methods. Although the computational effort required for MD simulations is much less than that for *ab initio* simulations, the processes of interest such as atomic diffusion and conduction are multiscale phenomena

that span a spatial scale range from nanometers to millimeters and time scale range from 10^{-15}-10^{-13} s of molecular vibration period to 10^{-6}-10^{-3} s, a minimum time required for conventional diffusivity measurements in studying PEFCs. Unless the results of a MD simulation can be comparable with the experimental results measured in a macroscopic system and in a timescale during which the phenomenon of interest occurs, it is not convinced that the MD method is useful for studying PEFCs or for atomistic computer design of new materials for PEFCs. The second major limitation is that classic MD methods cannot describe bond breaking and formation and chemical reactions.

2.5.3 Advancement of MD methods

2.5.3.1 Empirical Valence Bond Models

Valence bond (VB) theories or empirical valence bond (EVB) methods have been developed in order to solve this problem with bond potential functions that (i) allow the change of the valence bond network over time and (ii) are simple enough to be used efficiently in an otherwise classical MD simulation code. In an EVB scheme, the chemical bond in a dissociating molecule is described as the superposition of two states: a less-polar bonded state and an ionic dissociated state. One of the descriptions is given by Walbran and Kornyshev in modeling of the water dissociation process [175,181].

2.5.3.2 MD modeling with reactive force field

Goddard et al. developed and validated the reactive force field (ReaxFF) to describe complex reactions (including catalysis) nearly as accurately as QM in some cases but at computational effort comparable to classical molecular dynamics [176,182]. Similar to

empirical nonreactive force fields, the reactive force field divides the system energy up into various partial energy contributions,

$$E_{system} = E_{bond} + E_{over} + E_{under} + E_{val} + E_{pen} + E_{tors} + E_{conj} + E_{vdWaals} + E_{Coulomb} \quad (2.28)$$

A fundamental assumption of ReaxFF is that the bond order BO'_{ij} between a pair of atoms can be obtained directly from the interatomic distance r_{ij} as given in Equation 2.30.

$$BO'_{ij} = \exp\left[p_{bo,1}\left(\frac{r_{ij}}{r_o}\right)^{pbo,2}\right] + \exp\left[p_{bo,3}\left(\frac{r^{\pi}_{ij}}{r_o}\right)^{pbo,4}\right] + \exp\left[p_{bo,5}\left(\frac{r^{\pi\pi}_{ij}}{r_o}\right)^{pbo,6}\right] \quad (2.29)$$

The bond order is the exponent of a summation of three terms. The first term is the contribution of σ bond characterized with $p_{\mathrm{bo},1}$ and $p_{\mathrm{bo},2}$. It is unity when r_{ij} is below 1.5 Å but negligible when r_{ij} is above 2.5 Å. The second term is the contribution of the first π bond characterized with $p_{\mathrm{bo},3}$ and $p_{\mathrm{bo},4}$. It is unity when r_{ij} is below 1.2 Å and negligible when r_{ij} is above 1.75 Å. The third term is the contribution of the second π bond characterized with $p_{\mathrm{bo}.5}$ and $p_{\mathrm{bo},6}$. It is unity when r_{ij} is below 1.0 Å and negligible when r_{ij} is above 1.4 Å. The partial energy contributions related to bonds, E_{bond}, E_{over}, E_{under}, E_{val}, E_{pen}, E_{tors}, and E_{conj} are all functions of bond order BO'_{ij}. All valence terms (bonds, angles, torsions) go to zero, as the bonds are broken (BO'_{ij}=0). Thus, in the ReaxFF modeling methods the force field the description of bond formation/breaking is smooth as a function of bond order. The bond orders are determined only by the

interatomic distances and are updated for every iteration. This allows automatically recognize and handle changes in connectivity as reactions proceed.

2.6 Atomistic modeling and molecular dynamics studies of an interface structure in the PEFC

Seeking a breakthrough in electrocatalysis of oxygen electroreduction reaction (OER) in cathodic catalyst layer is one of the major issues in the current PEFC research. The exchange current density for oxygen reduction is about 6 orders of magnitude lower than that for hydrogen oxidation. The slow rate and associated high overpotential at the cathode of PEFC limits their specific power output (kW kg^{-1}) and overall efficiency. Generally speaking, if the voltage of a single cell is maintained at 0.8 V, a significant efficiency loss (30%) is due to the cathode overpotential although a high platinum loading (e.g. 0.5 mg cm^{-2}) that may contributes a high device cost is used. If the exchange current density for OER is increased significantly by 2-3 orders of magnitude, the specific power can be increased by many times at the same output voltage and efficiency. Thus, the ratio of performance to the cost is increased by that many times. It is commonly accepted that the transport processes, the adsorption/desorption, and reaction path in the specific interface structure between the polymer electrolyte and catalysts dictate the electrochemical activity of the catalyst layer. This underlies the fact that the electrochemical activity of the OER at cathode for the Pt/Nafion electrolyte interface is 3 orders of magnitude lower than that of a Pt/H_2SO_4 interface [183-184]. Specifically, the exchange current density on Pt/C catalyst in conjunction with Nafion electrolyte is reported 8.0×10^{-7} A cm^{-2} for oxygen reduction at the cathode (ca. 10^{-3} A cm^{-2} for hydrogen oxidation at the anode) on the basis of the area of the catalyst layer [185]. This

is equivalent to 2.0×10^{-9} A cm^{-2} on the basis of true active area of Pt crystallites. However, in 0.5 mol L^{-1} H_2SO_4 and with specific adsorption, Pt crystallites show an exchange current density between 5.0×10^{-7} and 6.0×10^{-6} A cm^{-2} on the basis of true active area of Pt [186]. Thus, the exchange current density at the Pt/Nafion interface is 2-3 orders of magnitude lower than that at the Pt/liquid electrolyte interface. Therefore, if the Pt/polymer electrolyte interface is as effective as the Pt/H_2SO_4 interface, the specific power of PEFC may be increased by many times. Lack of understanding of the catalyst layer may underlie the fact that 30 years' great efforts on development of the catalysts and polymer electrolytes have not resulted in a desired progress. Better understanding on the catalyst/polymer electrolyte interface structures and its implication for OER may be the key for a breakthrough. In the last 10 years, a growing number of *ab initio* studies of OER on transition metals and alloys have been reported. These theoretical studies shed light on the understanding of microscopic mechanisms. However, at the present time, *ab initio* modeling is unable to provide convincing descriptions for the interface structure and detailed reaction steps due to the limitation with over-simplified models and extremely short timescale. Although MD methods can be used to establish an interface between the polymer electrolyte and catalysts with a realistic size, the results are not convincing because classical MD methods are not supposed to describe interactions between polymer electrolyte and catalysts involving bond breaking and formation. ReaxFF based MD studies may enable us to determine the fundamental processes at realistic electrode-electrolyte interfaces. However, no result has been published yet [182].

2.6.1 The interface structure

It is believed that the greatest challenge to understanding and optimizing PEFC performance is to comprehend the processes taking place at the interface between the hydrated polymer electrolyte (Nafion) and the cathode (carbon-supported Pt nanoparticles). It is essential to understand how the protons and electrons are transferred across the cathode/membrane interface, particularly, how this is affected by the distribution of water at this interface. However, in earlier simulations on the electrochemical reactions no electrolyte molecules were involved [187-191]. It is amazing that these earlier simulation results based on the so-called "vapor-phase" models have been used as basis for development of catalysts in PEFCs. The apparent oxygen reduction reaction rate is governed by a series of physicochemical processes that occurs at the buried electrode interface. First of all, diffusion of oxygen supplies reactants via two paths: 1) through the polymer electrolyte and 2) through the exposed region on the catalyst. Although most authors believe that the first path dominates, the possibility of the second path cannot be eliminated. Other issues regarding to diffusion of oxygen include: the effect of the support and catalysts on the diffusion of oxygen, the roles of the water layer, polymer clusters, and specific adsorbates at the interfacial area, and impact of the electrical field at the interface. Adsorption/desorption is often considered as the rate determining step (rds) of OER. Adsorption can dramatically alter the structure and electrical field distribution and hence impact the entire OER process. Electron and proton transfer at the interface is directly related to the electrical field or EDL and must be heavily affected by the interface structure or specifically the adsorption of polymer functional groups, distribution and orientation of water, and adsorption of oxygen. Finally,

formation and rejection of water is the last step of the reaction. Modeling of the electroreduction of oxygen first requires a precise description of the interface structure.

Indeed, the EDL structure has been one of the major topics of electrochemistry in liquid electrolytes. Numerous studies on atomistic modeling of the electrode/water interface have been reflected in a bulk of literatures. In earlier years, empirical force field models were created [192-196]. Latterly, *ab initio* simulation derived metal-water and metal-ion pair potential based MD models appeared. Quantum mechanics models were created with periodic boundary conditions and with empirical electrical field of a continuum positive charge "jellium" [197-201]. Pseudopotentials for the electrode were used to define the interface structure [202-205]. *Ab initio* valence electron cluster models are often specified as interface model but only include a few atoms [206-213]. Many theoretical analyses obtained a picture that the metal-water interface is highly organized and there is a peak of water density near the electrode at room temperature [192-198,202-205]. This ordered structure is often referred as "icelike" or a prevalent hydrogen-bond ring structure. This has also been detected experimentally using X-ray reflectivity by Toney [214]. It has also been demonstrated, however, that although the time averaged structure is icelike, at any individual moment the water arrangements at the surface are completely random. Understanding of the structure of water layer is relevant for modeling PEFC because presence of water on catalysts does greatly impact the performance of PEFC. However, it is also important to understand the impact of the polymer clusters on the EDL and OER process. Unfortunately, the number of publications on the EDL structure of catalysts/polymer electrolyte is very limited. To date,

understanding of the EDL in PEFC largely relies on *ab initio* modeling for the EDL at the catalyst/water interface.

2.6.1.1 *Ab initio* modeling of interface structure in aqueous solutions

Unfortunately, there has hardly been any *ab initio* work on the structure of catalyst/polymer interface. On the other hand, there is a bulk of literature on the structures of catalyst/water interfaces. These studies are considered as being relevant for PEFCs because it commonly accepted that the water layers between the polymer and catalysts play a major role in OER. These studies were probably stimulated by the famous experimental findings by Toney et al. who investigated the interfacial structure of water molecules near charged metal surfaces using *in situ* X-ray scattering techniques [214]. The major findings are that water is ordered in three molecular layers above the metal surface and the orientation of interfacial water molecules depends on the sign of the charge density of the surfaces. In addition, they concluded that the area density of water next to a charged surface is very high compared to its bulk density. For example, the surface density of water molecules next to a positively charged silver electrode with a potential of 0.52 V relative to the potential of zero charge is about two times as great as that of bulk water [214]. Because of the ordering and high density of water, it was suggested that the dynamics of water molecules near charged surfaces would be very different from that of the bulk molecules.

Establishment of a correct electrical field as a function of electrode potential at the interface is a crucial and difficult issue for modeling the interface structure. Lozovoi et al. pioneered the use of a potential reference and a homogeneous countercharge and modeled field-evaporation effects [215]. Filhol and Neurock applied this idea to the

electrode/water systems via the creation of two potential references-a vacuum state and an aqueous state [216]. Briefly, a net surface charge density was introduced to the electrode via the variation of the number of electrons available to the self-consistent calculation, and overall cell neutrality condition was maintained by applying a homogeneous background charge for mimicking the presence of a diffuse ionic distribution close to the interface.

Taylor et al. further advanced the method by introducing explicitly a plane of ions with the countercharge rather than a homogeneous countercharge in the liquid phase [217]. The electrochemical potential of the interface was established by adding a charge on the Pt slab while adding a compensating charge in the electrolyte side of the interface (Figure 2.11). The potential at an arbitrary position z and Fermi potential of the electrode is given in reference to the potential at the center of the vacuum. The second reference is in the middle of a portion of electrolyte that is fixed far from the electrode while the rest of system is relaxed in response to the applied charge. The potential at all other position, z, including Fermi potential of the electrode is shifted according to the second reference point.

$$\phi_q(z) = \phi_q^{'}(z) - \phi_q^{'}(R) + \phi_0(R) \tag{2.30}$$

$$\phi_q(F) = \phi_q^{'}(F) - \phi_q^{'}(R) + \phi_0(R) \tag{2.31}$$

where the subscript q represents the amount of charge on the Pt electrode, $\phi_q(z)$ and $\phi_q(F)$ are the referenced potential at z and the referenced Fermi potential respectively, $\phi_q^{'}(z)$ and $\phi_q^{'}(F)$ are the un-referenced potential at z and the un-referenced Fermi

potential respectively, and $\phi_0(R)$ is the potential at the reference point in the portion of electrolyte in reference to the vacuum reference point (the first reference). The electrode potential vs. an SHE, U_q is given by

$$U_q = -4.8 - \phi_q(F) \tag{2.32}$$

At a given potential, the AIMD was run up to 30 ps for structure optimization. Electrochemical reactions were analyzed using DFT methods. Their results demonstrate that use of a homogeneous countercharge in aqueous solution is a good approximation but it is not in vapor phase. Although via other experimental and theoretical studies, water is in a so-called icelike ordered state, they did observe that the repulsion and rotation of water dipoles at the interface in a random way. This is one of many cases showing that atomistic simulation in "liquid phase" can reveal some of very important behaviors that cannot be directly obtained with the "vapor phase" models.

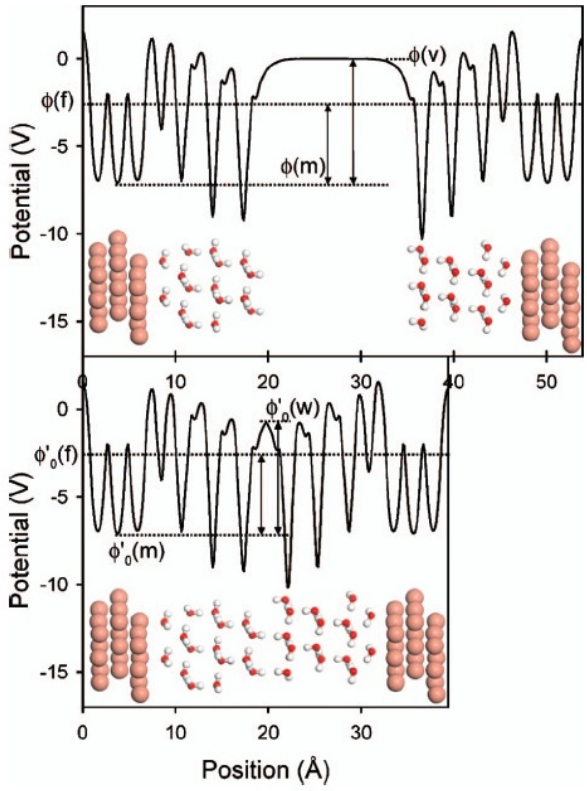

Figure 2.11 A schematic diagram illustrating the electrostatic potential profile as a function of position across the normal axis of the unit cell. The system shown here contains two symmetric Cu(1 1 1)/H_2O slab faces contained within the periodic simulation cell [217].

Following this approach, Janik et al. studied the electrochemical reactions using 20-30 water molecules for mimicking the water layer on a Pt slab under periodic boundary conditions but without accounting for the role of polymer. They evaluated the interface structure considering the adsorbed oxygen (Figure 2.12) [218]. Interesting findings also include that O_2 may tends to have a η_1-like structure with a tilt to the Pt surface; however, previous vapor-phase calculations found that O_2 only adopts this η_1 mode at full surface coverage. They also evaluated the adsorption energetics as a function of potential in the

standard hydrogen electrode (SHE). These energetics normally are not monotonic functions of potential.

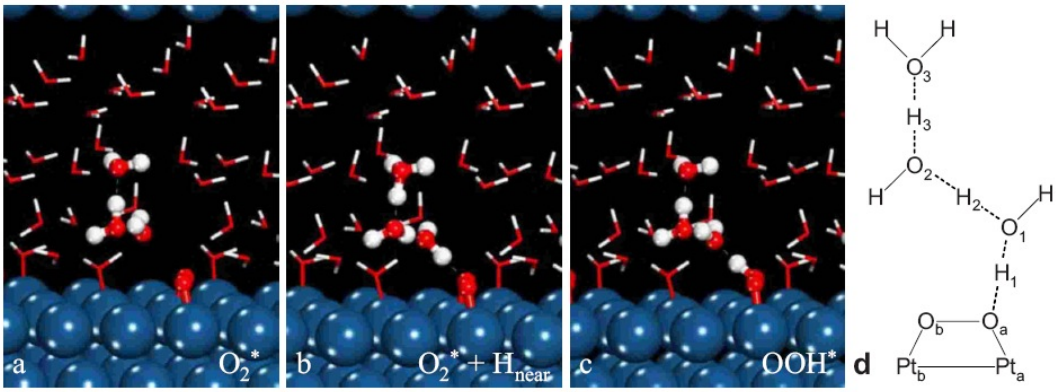

Figure 2.12 Optimized structures of the initial adsorbed molecular O_2 and the OOH* intermediates over aqueous solvated Pt(1 1 1) surface as determined by DFT [218].

Ab initio molecular dynamics (AIMD) simulation is a useful method in determining the interface structure without relying on any assumption. Izvekov et al. investigated adsorption of water on Cu(1 1 0) [204]. They claimed that the simulation results were in good agreement with the experimental results. It was found that there is a strong coupling of the water overlayer with the metal crystal electronic states. However, the surface-states charge density is undisturbed by the presence of water.

2.6.1.2 MD modeling of interface structure on catalysts in aqueous solution

Raghavan et al. described a form interaction potential between rigid water and a rigid platinum metal surface [219]. Using this potential they performed a MD simulation on water lamina restricted by two Pt(1 1 1) surfaces. At 300 K the contact water layer to the metal surface displays a solid-like behavior that was evidenced by patches of ice-like structure observed in the simulation. The next two layers of water display ordering

similar to ice-I. Beyond these three layers the structure and dynamics of water are bulk-like.

Spohr investigated the effects of the empirical electrostatic boundary conditions on the interface properties of water and on the adsorption of ions [220]. Spohr also conducted molecular dynamics simulations of water layers confined by two Pt(1 0 0) surfaces. The structure is revealed mainly with one-particle density profiles and solvent pair correlation functions. He found that the surface-induced structural heterogeneity ranged up to distances of 10 Å and that the central water layer is bulk-like.

The structure of water near charged surfaces was studied by Berkowitz et al., Kiseley et al., and Snnapati et al. [221-225]. These authors carried out MD simulations of both nonpolarizable SPC/E and polarizable PPC models of water near charged metal surfaces and found no dramatic increase of the water density and disruption of hydrogen bonding near the charged surfaces.

The dramatic increase of water density at a charged surface was observed by Toney et al. in their *in situ* X-ray scattering experiments has not yet been confirmed by simulation results [203,226]. In another MD simulation work, Kiselev et al. found that self-diffusion coefficient strongly decreases with increasing electric field [188]. However, no difference between the self-diffusion coefficients for motion parallel and perpendicular to the external field was observed.

Halley et al. employed a MD method for the simulation of metal/water interfaces [203]. They found that the occupancy of on-top binding sites for water in this model as applied to a (1 0 0) surface of ‘copper’ was very sensitive to potential. They suggested that this

may provide an explanation for some previously unexplained features of X-ray data on water structure and noble metal/water interfaces. They also noticed that the strong bonding of water on a metal surface may result in metastable charging of the interface in molecular dynamics timescales.

2.6.1.3 MD modeling of interface structure of catalyst/polymer electrolyte interface

To date, it is difficult to model the interface between catalyst and polymer electrolyte. MD methods allow simulation of a system with 10^3-10^5 atoms. Thus, MD simulations are suitable for describing a system with the realistic size of a metallic catalyst on carbon support in contact with a cluster of polymer electrolyte (Figure 1.5). The problem is, however, whether these simulations are correct.

Balbuena et al. involved polymer molecules in the MD modeling of the metal catalyst/Nafion interface [227]. Figure 2.13 shows all the sulfonated groups surrounding a metal cluster and their distances to the catalyst particle. They used this method to estimate the number of Pt atoms that are directly accessible by protons migrating through the water clusters formed in the hydrophilic sites of a Nafion cluster. The diffusion of protons to the reaction centers on top of Pt surface is a crucial step of OER. They found that within simulation timescales (maximum production time of 400 ps), once the polymer is attached to the carbon support or catalyst, its constituent atoms generally vibrate around their equilibrium positions and little further configuration changes are observed in the side chain.

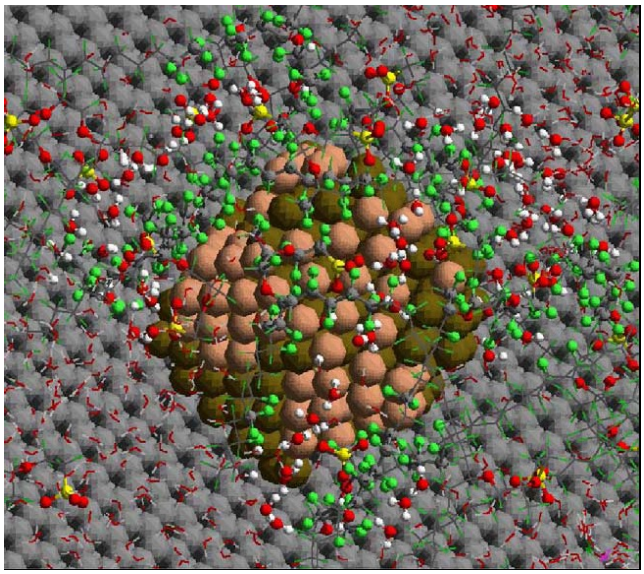

Figure 2.13 Interactions of Nafion's side chains and a Pt nanoparticle. Atoms that are in regions around the sulfonated groups have been enlarged to improve visualization. Color codes: H (white), red (O), F (green), C (gray), S (yellow), Pt (light brown) [227].

Balbuena et al. also conducted simulations at various water concentrations for various water contents (Figure 2.14). At low water contents (λ=5), small water clusters are almost not connected with each other (Figure 2.14(a)). At a very high water concentration (λ=45), water forms a continuous phase (Figure 2.14(c)). When λ is about 24, close to the amount in fully hydrated Nafion membranes at room temperature, the interface is defined by a semi-continuum water film (Figure 2.14(b)) where some water clusters with diameters of about 1 nm are interconnected by multiple water bridges. The average water density in this phase is estimated to be about 0.682 g cm^{-3}, a much lower value than that of the bulk water phase at 353 K.

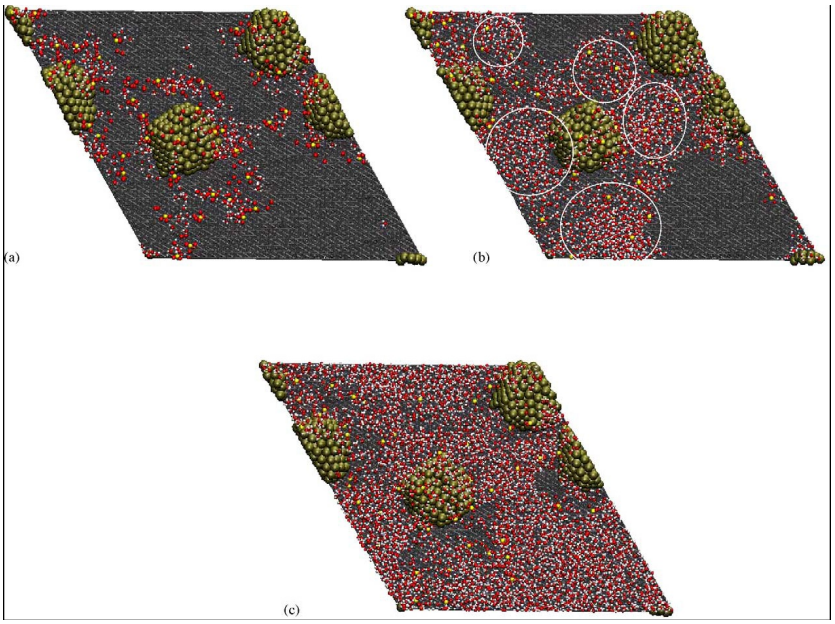

Figure 2.14 Distribution of water near the catalyst at different λ values: (a) λ = 5, (b) λ = 24, and (c) λ = 45. Nafion is not shown in order to clearly illustrate the water clusters. At λ = 24 the clusters (highlighted) are defined showing connectivity among them [227].

Recently, Goddard et al. have developed ReaxFF potentials covering the following aspects of PEFC chemistry in the form shown in [182,228]:

(1) Reactions at metal surfaces. They have developed ReaxFF for Pt/C/H/O, Ru/H/O and Ni/C/H/O interactions in order to enable a large-scale dynamical description of the chemical events at the fuel cell metal anode and cathode.

(2) Oxidation/reduction reactions. They have fitted ReaxFF against a wide range of metal oxidation states to ensure that ReaxFF describes redox reactions accurately.

(3) Hydrogen transport. The approach that they have used to predict proton transport through complex membranes such as Nafion is to use *ab initio* methods to determine the barriers for migration of hydrogen as a function of the donor–acceptor separation and

then to employ a statistical method that is based on the *ab initio* results. This method allows a proton jump among water clusters when the configuration around the proton is appropriate.

Although the interface models by the MD methods provide a picture of the atomic distribution of the interface, because of the limitation of the MD method, the details of the interface structure in the vicinity of the electrode is not accurate. The effect of polymer side groups and backbone on the interface structure, specifically the EDL is not addressed with sufficient confidence. The AIMD simulations have already demonstrated striking differences with those performed using classical pair potentials (MD force field).

2.6.2 Oxygen electroreduction reaction with an emphasis on charge transfer at metal/water interface

The research on charge transfer at metal/water interface is considered as a first stage towards a more realistic model including polymer and is considered as being relevant to the study of PEFC. In a description of quantum mechanics, charge transfer occurs when:

$$\Phi - eV = I - \Delta G_s \tag{2.33}$$

where Φ is the workfunction of the metal electrode, V is the potential difference between the electrode and electrolyte at OHP, I is the ionization potential of the reactant, ΔG_s is the change of its solvation (hydration) energy upon electron transfer or charge transfer. Equation 2.33 expresses that at the equilibrium state of the charge transfer reaction at the interface the Fermi's level in the electrode should matches the lowest unoccupied molecular orbital (LUMO) or highest occupied molecular orbital (HOMO) of the

reactants. In a general description of quantum statistical theory, the electrochemical current density, j, is given by literatures [229-230].

$$j = \sum_{\Omega} [C]\left(\frac{\omega_{eff}}{2\pi}\right)\exp(\sigma_t)\int_{z_{\min}}^{\infty} k_e(z,\Omega)\exp\left(-\frac{\Delta E_a(z,\Omega}{kT}\right)dz \qquad (2.34)$$

where Ω is the orientation degree of freedom, z is the reactant-metal surface distance, z_{min} is the minimum distance of the reactant to metal surface, [C] is the bulk reactant concentration, ω_{eff} is the effective frequency of classic vibration modes of reacting cluster, k_e is the electron transfer coefficient, σ_t is the electron tunneling factor, and ΔE_a is the activation energy. Thus, the electron transfer at the interface is dictated by the EDL structure described with the HOMO or LUMO levels, the wavefunctions (Ψ_i^{tr} and Ψ_f^{tr}), vibration of reacting molecules, the electron tunneling factor, and z_{min}. In the liquid electrolyte, z_{min} is similar to the OHP and only ~0.5 nanometers from the metal surface (Figure 1.4 (b)). The activation energy, ΔE_a, is a function of the potential drop across the EDL or overpotential and the detailed equilibrium and dynamic structures of EDL. Most of simulation studies in this topic are in fact purported to evaluate the activation energy but rarely to evaluate the electron transfer coefficient. Without a correct description of the electron transfer coefficient but only a good description of the activation energy, it would be difficult to predict the OER behavior of a given system without a fitting to experimental results. Thus, the *ab initio* models cannot be verified and the modeling methods are not reliable tools for designing and evaluating a new catalyst/polymer electrolyte system.

The OER is a multi-electron reaction which may include a number of elementary steps and involve different reaction intermediates. There are several pathways for O_2 electroreduction: (1) a "direct" four-electron reduction to H_2O (in low pH media) or to OH^- (in high pH media); (2) a two-electron pathway involving reduction to hydrogen peroxide; (3) a "series" pathway with two- and four-electron reduction; (4) a "parallel" pathway that is a combination of (1)-(3); (5) an "interactive" pathway in which the diffusion of species from (2) or (3) path into a "direct" path is possible. For Pt catalyst, four-electron reduction is believed to be the dominant one. However, the exact mechanisms are still unclear for all of these paths. Even for the first electron transfer step, there are two different views based on *ab initio* simulation results [231-232]. One of major problems for previous studies is that the models are too much simplified to reveal the effect of polymer. In fact, there has hardly been any simulation work on OER at the catalyst/polymer interface. Most of relevant studies use either vapor phase interface models or catalyst/water interface models. The electrode potential was usually not established explicitly in the way used by Taylor et al. and Janik et al. [233-234].

Anderson and his coworker carried out a series quantum chemistry studies of oxygen reduction reactions [208-213]. Anderson and Abu first studied reversible potential and activation energies for uncatalyzed oxygen reduction to water and the reverse oxidation reaction using the MP2/6-31G** method. The electrode was modeled by a non-interacting electron donor molecule with a chosen ionization potential (IP). The primary assumption is that when the reactant reaches a point on the reaction path where its electron affinity (EA) matched the donor IP, an electron transfer is initialized. The donor's IP or reactant's EA was related to the electrode potential by,

$$U = \text{IP}/\text{eV} - 4.6\ \text{eV} = \text{EA}/\text{eV} - 4.6\ \text{eV} \tag{2.35}$$

where "4.6" is the reference hydrogen electrode. They calculated the reaction energies of the following four-electron transfer reduction and two-electron transfer reduction:

$$O_2(g) + 4H^+(aq) + 4e^-(U) \leftrightarrow 2H_2O(aq) \tag{2.36}$$

$$O_2(g) + 2H^+(aq) + 2e^-(U) \leftrightarrow H_2O_2(aq) \tag{2.37}$$

With temperature, entropy and enthalpy correction, they obtained free energy change ΔG^0. The reversible electrochemical potential was calculated by the equation

$$U^0 = -\frac{\Delta G^0}{nF} \tag{2.38}$$

where n is the number of electrons transferred in the reaction, and F is the Faraday constant. The calculated reversible electrochemical potential was 1.18 V for four-electron transfer compared with 1.23 eV for the experimental number. For the two-electron transfer the electrochemical potential was 0.61 eV and the experimental number was 0.70 eV. They calculated the activation energy of the four one-electron transfer steps:

$$O_2(g) + H^+(aq) + e^-(U) \rightarrow HO_2\bullet(aq) \tag{2.39}$$

$$HO_2\bullet(aq) + H^+(aq) + e^-(U) \rightarrow H_2O_2(aq) \tag{2.40}$$

$$H_2O_2(aq) + H^+(aq) + e^-(U) \rightarrow HO\bullet(g) + H_2O(aq) \tag{2.41}$$

$$HO\bullet(g) + H+(aq) + e-(U) \rightarrow H_2O(aq) \tag{2.42}$$

The charge transfer reaction was modeled with a configuration shown in Figure 2.15.

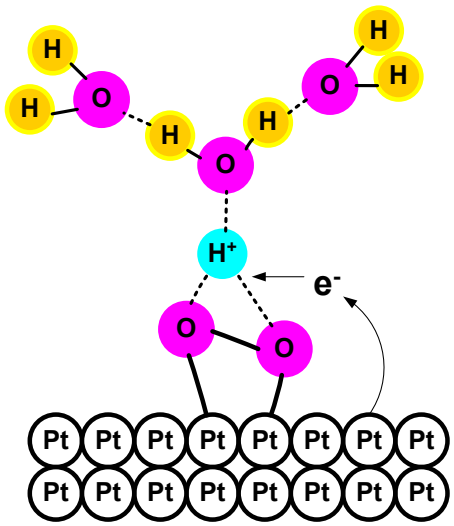

Figure 2.15 Structure model for charge transfer reaction at a Pt site.

One of the important issues is how to establish a correct electrical field in the reaction center. Because in reality, the electrolyte contains many ions, the contribution of all of them is estimated as a function of electrolyte ionic concentration by assuming that H_3O^+ at the reaction center experiences an average potential due to interactions with all the anions and cations in the electrolyte. Thus, Madelung sums of the potentials due to ions in a various regular arrays (crystal lattices) were calculated [212]. In these sums, the total infinite sum of interactions is equal to a single coulomb interaction. Anderson et al. assumed a rock-salt structure, for which the coulomb potential is given. The Madelung sum condenses all of the contributions to the potential at the reaction center to a single point charge as shown in Figure 2.16.

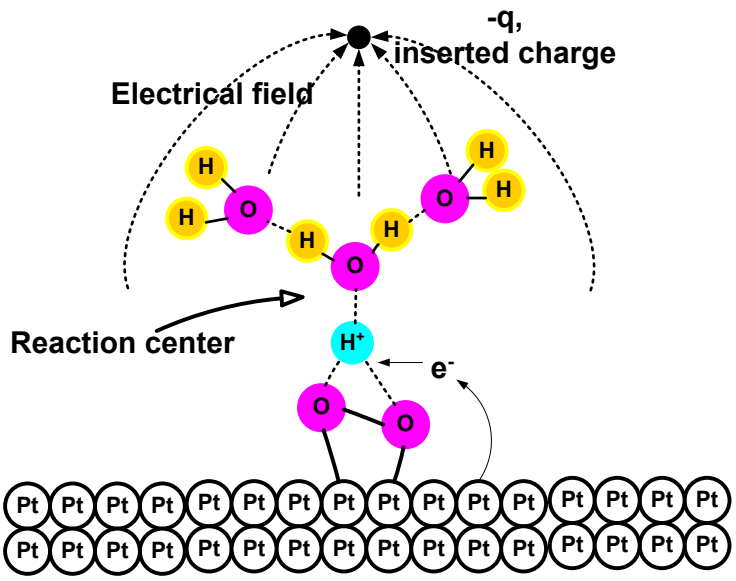

Figure 2.16 The Madelung sum of all the coulomb interactions of the electrolytes and their counterparts in base reduce to interactions between point charges as shown and the reaction center.

Using this interface model and the method for establishing an electrode potential, Anderson et al. evaluated the potential energy surface of each of the elementary reactions and identified the transition state [212]. The lowest energy of the system had electron affinity equal to 4.6 eV + eU (U, the potential of the electrode). They studied the elementary steps in the electrode potential range of 0-2V (vs. SHE) and noticed that H_2O_2 reduction (Equation 2.42) had the highest activation energy. These results were consistent with experimental observation of H_2O_2 generation over the weakly interacting electrodes like mercury and gold. The activation energies increased as the electrode potential increased. The activation energies for the four steps are in the order: third step (Equation 2.42) > first step (Equation 2.40) > second step (Equation 2.41) > fourth step (Equation 2.43).

Anderson et al. reported the effect of platinum on oxygen reduction using a similar MP2 method [235]. A single platinum atom was used for coordinating with O_2, $HO_2\cdot$, H_2O_2 and $HO\cdot$:

$$Pt\ O_2 + H^+(aq) + e^-(U) \rightarrow Pt\ OOH \quad (2.43)$$

$$Pt\ OOH + H^+(aq) + e^-(U) \rightarrow Pt\ (OHOH) \quad (2.44)$$

$$Pt\ OHOH + H^+(aq) + e^-(U) \rightarrow Pt\ OH + H_2O \quad (2.45)$$

$$Pt\ OH + H^+(aq) + e^-(U) \rightarrow Pt\ OH_2 \quad (2.46)$$

With this simple model, they found that binding the Pt atom to $HO_2\cdot$ and H_2O_2 stretched O-O bonds. Order of the effect was H_2O_2>O_2>$HO_2\cdot$. The Pt atom had a significant effect on the most difficult reduction step, the reduction of HOOH to $HO\cdot$ +H_2O (Equation 2.45).

Li and Balbuena conducted a study of the first electron transfer step (Equation 2.47) using the DFT method with a catalyst model of five Pt atoms [236].

$$Pt_5O_2(ads) + H^+(aq) + e^- \rightarrow Pt_5OOH \quad (2.47)$$

The solvation effect was modeled through hydration of a proton by three water molecules ($H_3O^+(H_2O)_2$). The effect of the electrode potential on the Pt/adsorbate/H_3O^+ complex was considered by assuming that the reactant complex ($Pt_5O_2\cdot H_3O$) was electrically neutral. In the model, the potential energy surface of the reaction is a function of the bond length of the adsorbed O_2 molecule, the shortest distance between the adsorbed oxygen and the water oxygen, and the shortest distance between the proton and the water oxygen. They revealed that the heat of the reaction (Equation 2.47) was 9.44

eV. They claimed that the proton transfer may not be involved in the rate-determining step and that a negative charge on the cluster/adsorbate complex results in a significant decrease in the activation energy.

Nørskov et al. studied the binding energy of the reactants and intermediates using a DFT method involving the following one-electron reaction in a dissociation mechanism as follows.

$$0.5O_2 + * \rightarrow O* \quad (2.48)$$

$$O* + H^+ + e^- \rightarrow HO* \quad (2.49)$$

$$HO* + H^+ + e^- \rightarrow H_2O + * \quad (2.50)$$

where "*" denotes a site on the surface [237]. They also investigated the following one-electron reactions in an association mechanism that involved the adsorbed molecular oxygen in the electron transfer as follows.

$$O_2 + * \rightarrow O_2* \quad (2.51)$$

$$O_2* + (H^+ + e^-) \rightarrow HO_2* \quad (2.52)$$

$$HO_2* + (H^+ + e^-) \rightarrow H_2O + O* \quad (2.53)$$

$$O* + (H^+ + e^-) \rightarrow HO* \quad (2.54)$$

$$HO* + (H^+ + e^-) \rightarrow H_2O + * \quad (2.55)$$

They calculated energies of different intermediate states. The results demonstrated that there was a correlation between oxygen reduction activity and the binding ability of O

and OH. They further claimed that at high potential adsorbed oxygen was very stable and that proton and electron transfer was impossible. In addition, they proposed that the origin of the overpotential for Pt was the O and OH adsorption and that both dissociative and associative reaction paths may contribute to the OER.

Jinnouchi and Okazaki performed AIMD studies of the first-electron transfer reaction with 1 H_3O^+, 9 H_2O, and 12 Pt atoms at 350 K as shown in Figure 2.17 [238]. The adsorbed water molecules and the hydronium ion hydrated the adsorbed oxygen atoms, and proton transfer through the constructed hydrogen bonds frequently occurred. When the conformation of these species satisfied certain conditions, the oxygen dissociation with the proton transfer reaction was induced and three OH were generated on the platinum surface (Figure 2.18). The authors concluded that the oxygen dissociation tendency is one of the dominant factors for the reactivity of the cathode catalyst. This work demonstrates the power of AIMD that does not require specific assumption in order to describe charge transfer.

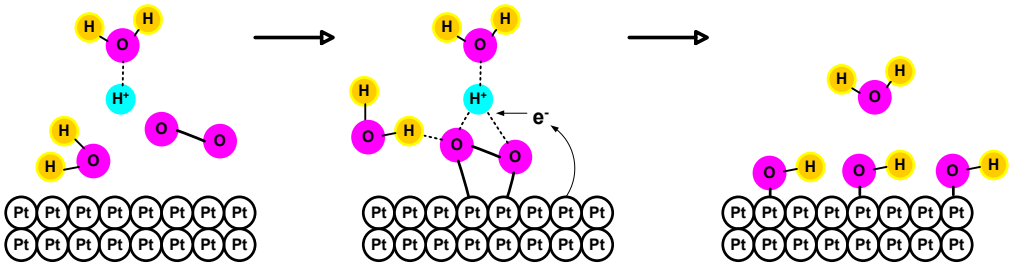

Figure 2.17 Mechanism of the first electron transfer in an oxygen reduction reaction.

Wang and Balbuena performed an AIMD study of this one electron reaction O_2+$H^+(H_2O)_3$/Pt(1 1 1) at 350 K [239]. They discovered that the proton transfer took place first and then chemisorption was observed. This first step induced the electron

transfer from the slab. Finally, the HO-O-Pt dissociated into H-O and O without a clear barrier. To study the effect of an electrical field, they modeled the system of O_2 + $H^+(H_2O)_3$/Pt(1 1 1) with an extra electron. The proton transfer intermediate was formed in the earliest stage. This finding is similar to results reported by Jinnouchi [238]. Wang and Balbluena suggested that the mechanism for the first electron transfer involved the three major steps with the following order: (1) proton transfer; (2) electron transfer; (3) dissociation and hydroxyl adsorption (Figure 2.18).

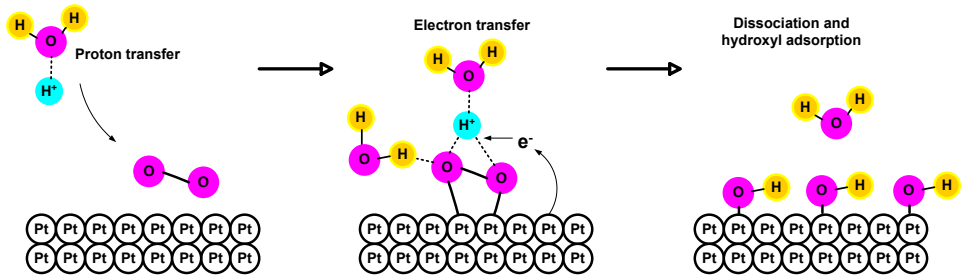

Figure 2.18 Proposed mechanism for the first electron transfer of OER.

Above simulations of the OER are based on models of a few atoms or a cluster of reaction center. Moreover, the electrode potential and the EDL are not explicitly established in the models or are established using ways of seemly oversimplification. Janik et al. conducted periodic density functional theoretical calculations with the double-reference method developed by Filhol and Neurock [216,218], to determine the potential dependence of the reaction energy and activation barrier for the reduction of O_2* to OOH* on the fully hydrated Pt(1 1 1) surface. Their method allows for tuning the electrode potential with a slab representation of the electrode surface. They found that electron transfer precedes the protonation of the adsorbed O_2 molecule. This occurs when the H^+ completely joins H_2O to form a H_3O^+ that is connected to the adsorbed O_2 molecule by hydrogen bonding through two additional water molecules. The observation

that the electron transfer precedes the proton transfer is different from that found by Wang and Balbuena [239]. The overall barrier to the first reduction step is the sum of the energies for the proton and for the electron to be incorporated within the reactive complex. They suggested that in order to simulate the OER process reliably it is necessary to include the extended electronic structure of the electrode, sufficient number of water molecules and the approaching proton in the DFT model system. With regard to this requirement, this study is more realistic than the other studies. Yet, even in this work, polymer atoms were not included apparently due to lack of suitable computational hardware or software or both at that time.

CHAPTER 3 ALL-SOLID-STATE MEDIATOR SUPERCAPACITOR WITH NAFION AS THE SEPARATOR

Nafion is a sulfonated tetrafluoroethylene based fluoropolymer-copolymer developed by DuPont Company. The unique property of Nafion as a proton conductor has attracted lots of attention in the PEFCs. In addition to high ionic conductivity, Nafion also has excellent thermal and mechanical stability. The structure of Nafion backbones is shown in Figure 3.1. Nafion in the form of membrane contains hydrophobic domains that are populated by -F groups and hydrophilic domains that are surrounded by sulfonated groups. It is believed that the dimension of the hydrophilic domains is about a few nanometers [26]. The protons in Nafion may be partially bonded to the sulfonated groups and partially free. The prevailed theory with respect to the transport of protons is the Grottheus mechanism. Essentially, the charge center of water/proton networks can move as a consequence of bond formation and breaking between protons and surrounding water molecules. Thus, existence of water is a necessity of proton conduction in Nafion. In fact, the conductivity of proton in Nafion strongly depends on the water content, λ, of Nafion, which is defined as number water molecules per sulfonated group. For instance, at 50% relative humidity, the water content is about 3 while at 100% relative humidity, water content is about 22. At water content of 22, the conductivity of Nafion is 0.1-0.2 S cm^{-1}, which is very high in comparison to other polymer electrolytes. For this reason, Nafion was used as the separator for the all-solid-state mediator supercapacitors.

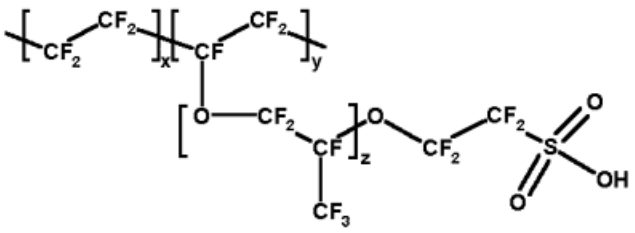

Figure 3.1 Molecular structure of Nafion.

3.1 Experimental

3.1.1 Preparation of PEO-based suspensions for electrode loadings

A mixture of PEO (M.W.=400,000, Sigma-Aldrich) and $LiClO_4$ (Fluka, ≥98%) was dissolved in acetonitrile (Sigma-Aldrich) and then was stirred at 60°C for about 4 hours until the mixture turned into a homogeneous translucent gel. The molar ratio of PEO monomer to $LiClO_4$ in the gel is 8:1. Mediators, including NaI (Alfa Aesar, 99.55%) and I_2 (Alfa Aesar, 99.8%) were then added into the PEO/$LiClO_4$ polymer gel. The gel was stirred for 1 hour until it turned translucent and homogenous. The gel was divided into two aliquots. One of them was stored aside for conductivity measurement, while the other one was mixed with carbon black (VULCAN XC72R) to form electrode suspension. The electrode suspension was sonicated for 1 hour before it was loaded on the current collector. Then the electrode was allowed vaporized at room temperature for 1 hour until the loading became dry. Supercapacitors consisting of electrodes with carbon black, but without mediators, were used as control references.

3.1.2 Preparation of supercapacitor assemblies

Figure 3.2 shows a schematic of the structure of the sandwich-like solid-state supercapacitor. In the middle is a Nafion® 117 membrane (Alfa Aesar), which served as

the separator. A piece of carbon nanofoam (Marketech International Inc.), which served as the current collector, was loaded with the electrode suspension. Two electrodes (2.0 cm^2) either loaded or not loaded with mediators and a Nafion membrane were pressed at about 4500 psi and 100-110 ^oC for 1 minute.

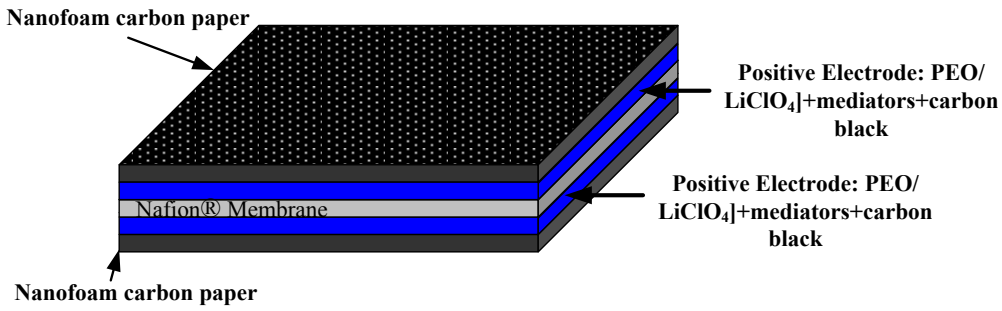

Figure 3.2 Schematic of a supercapacitor assembly.

3.1.3 Experimental characterization and evaluation

3.1.3.1 Conductivity measurement

PEO/$LiClO_4$ and PEO/$LiClO_4$/mediators were very soft gel-like materials. Therefore, membranes of these materials had to be casted on PTFE sheets, and allowed 1 hour for drying. The lateral or in-plane conductivity of the films were evaluated using a four-electrode AC impedance method which was described in details in a previous publication [240].

3.1.3.2 Performance evaluation of the supercapacitors

The performance of the supercapacitors was studied using CV (voltage range of 0.0-1.0 V, scanning rate of 25-200 mV s^{-1}) and GCD (charge/discharge current density of 5-

20 mA cm^{-2}) methods. All experiments were carried out at room temperature using a Gamry electrochemical measurement system.

In the self-discharge experiments, the supercapacitor was charged to 0.95 V, afterwards the open-circuit voltage was monitored as a function of time over a duration of 50,000 seconds.

3.1.4 X-ray absorption spectroscopy study

An all-solid-state mediator supercapacitor was fabricated using the methods described in Section 3.1.2. A piece of carbon nanofoam (2.0 cm^2) was loaded with PEO+$LiClO_4$+EC (18 mg), NaI (10 mg), I_2 (1 mg), and carbon black (1.4 mg) and was used as the working electrode. Another piece of carbon nanofoam loaded with PEO+$LiClO_4$+EC (29.4 mg) and carbon black (5.5 mg) was used as the counter electrode. A hydrated Nafion® 117 membrane served as the separator. The assembly (working electrode / Nafion membrane / counter electrode) was pressed at about 4500 psi and 100-110 ^oC for 1minute. The supercapacitor was then charged and discharged at constant current of 5 mA using a portable Gamry electrochemical system (Series G 750 Potentiostat / Galvanostat / ZRA). A schematic of the spectroelectrochemical cell used during the course of the XAS investigations is shown in Figure 3.3.

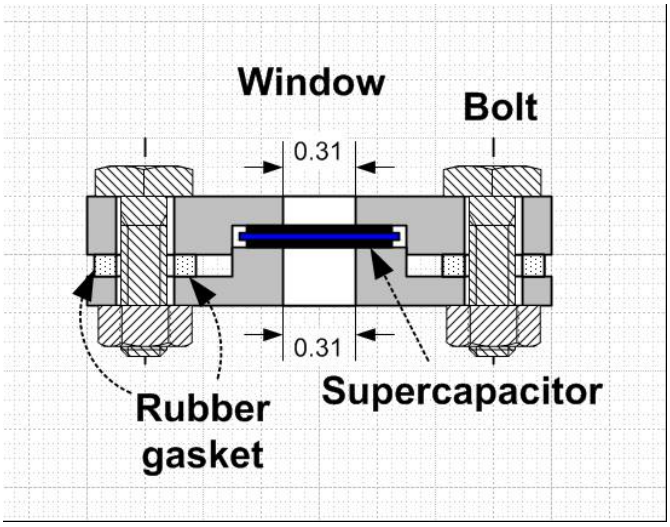

Figure 3.3 A schematic of the spectroelectrochemical cell used for the in situ XAS investigations of an all-solid-state SC. The dimensions are in inches.

The X-ray absorption fine structure (XAFS) experiments were conducted on the bending magnet station X-11A of the National Synchrotron Light Source with the electron storage ring operating at electron energy of 2.8 GeV and a stored current in the range of 200 to 300 mA [241]. The XAFS spectra were collected in transmission mode at room temperature using a variable exit double-crystal monochromator with two flat Si(311) crystals detuned by 20% to reduce the harmonic-content of the beam. The incident and transmitted beam intensities were monitored using 30 cm long ionization chambers with Ar flowing. A third 15 cm long ionization chamber with Ar flowing was used to monitor the transmitted intensity of a reference I_2 standard to ensure accurate calibration of the energy scale. The XAFS spectra at the I K-edge (33,169 eV) were collected under *in situ* conditions using specially designed spectroelectrochemical cell (Figure 3.3) with electrodes containing NaI/I_2 mediators charged and discharged at constant current of 5 mA to varying anodic and cathodic potentials. Electrodes containing

either NaI or I_2 mediators were also analyzed under open-circuit condition for comparison purposes.

The XAFS spectra were analyzed using the Athena Software package [242]. The XAFS was calibrated with respect to the I_2 K-edge energy at half-height, which has been assigned to 33,169 eV. The K-edge absorption was isolated by fitting the pre-edge region (-300 to -100 eV) to a first order polynomial, extrapolating over the entire range of the spectrum, and subtracting the background from the entire spectrum. Energy independent step normalization was applied by fitting the post-edge region (150-800 eV) to a cubic polynomial and extrapolating back to the edge energy. The photoelectron wave number, k, was defined relative to the edge energy at half-height. The extended x-ray absorption fine structure (EXAFS), $\chi(k)$, was extracted using multi-node cubic spline procedures, which minimized the amplitude of non-physical peaks in the 0-1.5 Å region of the Fourier transform. The Fourier transforms were generated using k^2-weighted EXAFS spectra over the range of 2.0-10.0 or 2.0-13.0$Å^{-1}$ with a Hanning window of 1.0 $Å^{-1}$.

Quantitative analyses of EXAFS spectra and Fourier transforms were also made using the Artemis software package [242]. The data were fitted using theoretical standards calculated based on *ab initio* self-consistent real space multiple-scattering formalism of the FEFF code (version 8.2) [243-244]. The FEFF calculations were performed using established structural models for I_2 [245] and NaI [246]. The Fourier transforms were generated using k^2-weighted EXAFS spectra over the range 2.0-10.0 $Å^{-1}$ with a Hanning window of 1.0 $Å^{-1}$. The fits were performed in real space using appropriate windows for the first shell contribution. In fitting the data, the many body amplitude reduction factor (S_0^2) was floated while the coordination number (*N*) was constrained to its

crystallographic value. The coordination distances (R), disorders (σ^2), and inner potential (E_o) were used as variables in the fit. The number of fitting parameters was kept below the maximum number of independent data points allowed by the Brillouin theorem [247]. The goodness of each fit is given by the value of the R-factor, which is the sum of the square of residuals between measured and model data normalized to the magnitude of the measured data.

3.2 Conductivity of the PEO/$LiClO_4$ with mediator

Table 3.1 lists the lateral conductivities of PEO/$LiClO_4$ membranes without and with NaI/I_2 mediators. It can be seen that the average conductivities are 6.2×10^{-4} and 2.0×10^{-2} S cm^{-1}, respectively, for the membranes without and with mediators. The conductivity increased significantly with the addition of the mediators. It is worth mentioning that when I_2 is combined with I^-, there will be a fast reaction between them to form I_3^- ($I_2+I^- \leftrightarrow I_3^-$) [248]. If it is true, three iodine-containing species, I_2, I^-, and I_3^-, are involved in the conduction process. The overall conductivity, given in Equation 3.1, is the sum of two components: 1) the physical migration of the ionic species, and 2) the electron exchange reaction that causes an apparent charge displacement. The mechanism of the second process in this case can be described with Figure 3.4. The processes of electron exchange between mediators are as follows: 1) approach of two mediators; 2) collision occurs and, electron transfers from I_3^- to I_2 or I_3^- to I^-; 3) separation of the mediators. Thus, the conductivity can be described by the following equation, which is derived from the Dahms-Ruff equation: [249-251]

$$\sigma = \left(\frac{2e^2}{kT} D_{AX}\right) c_A + \left(\frac{e^2 \delta_{AX}^2 k_{ex}}{3kT}\right) c_A^2 \tag{3.1}$$

where the subscripts AX and A denote I_3^- and I^- respectively, D_{AX} is the physical diffusion coefficient, c_A is concentration, δ_{AX} is the center-to-center intersite distance at the exchange reaction, k_{ex} is the exchange reaction rate of the two reactions described in Figure 3.4. Note that the second term in Equation 3.1 describes the exchange-reaction-based conduction, which exists only in the presence of the mediators. Thus, an enhancement effect to the overall conductivity can be obtained [248]. According to Ref. [248], when the concentration of mediators is low (0.01 mol L^{-1}), the contribution of electron exchange reaction may be negligible. But at a high concentration of mediators (~2.57 mol L^{-1} in this case), the second term in Equation 3.1 may become a major contribution to the overall conductivity.

Table 3.1 Conductivity of membranes without and with mediators.

Membrane	Conductivity (S cm^{-1})	Average conductivity (S cm^{-1})
without mediators	6.61×10^{-4}	6.22×10^{-4}
	6.44×10^{-4}	
	5.60×10^{-4}	
with mediators	2.33×10^{-2}	2.02×10^{-2}
	1.87×10^{-2}	
	1.86×10^{-2}	

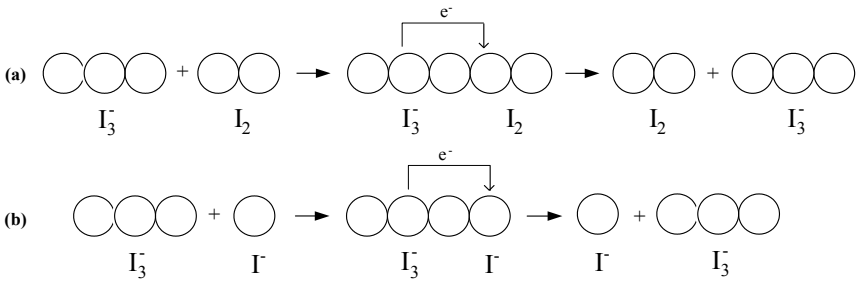

Figure 3.4 Schematic of electron transfer processes between iodine species: (a) between I_3^- and I_2; (b) between I_3^- and I^-.

3.3 CV results

Before each CV test, an electrochemical impedance spectroscopy measurement was conducted. For the carbon black supercapacitor (CB SC) the series resistance was about 1.0 Ω. Figure 3.5 illustrates the CVs of a CB SC at different scanning rates. The specific capacitance of the CB SC at the scanning rate of 25 mV s^{-1} was 44.7 F g^{-1} within a voltage window of 0.0-1.0 V. For the CB SC, the CV curve shows a roughly rectangular shape, implying that the SC with the current configuration has a good capacitive behavior [252]. However, for a SC with NaI/I_2 mediators or NaI/I_2 SC, peaks can be observed in the voltage range of 0.0-0.7 V, indicating a battery-like behavior with Faradaic charge/discharge. At a voltage higher than 0.7 V, the SC shows a capacitive behavior. An enhancement factor by ~3 can be seen through a comparison of the specific current density of the CB SC and that of the NaI/I_2 SC within the voltage range of 0.7-1.0 V.

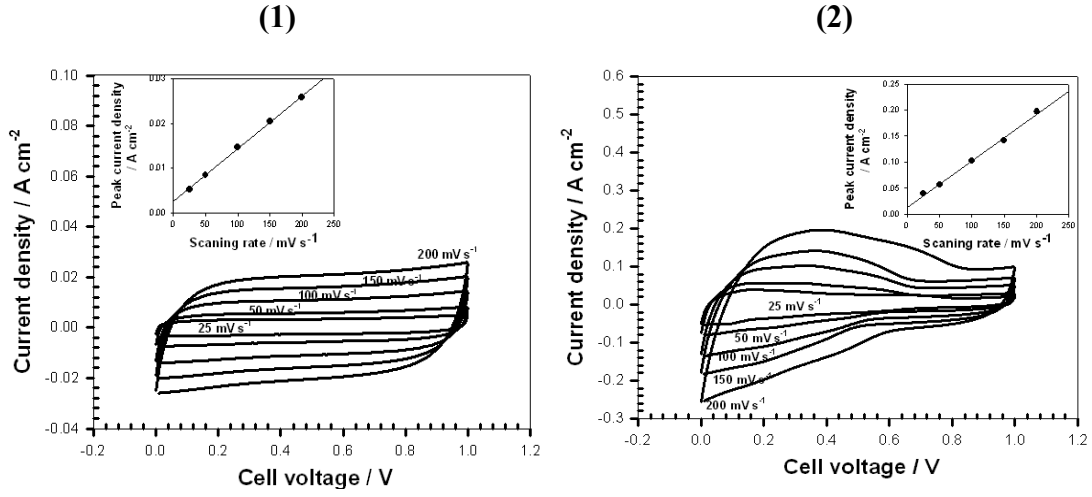

Figure 3.5 Cyclic voltammograms of (1) the CB SC and (2) NaI/I_2 SC with scanning rates of 25, 50, 100, 150, and 200 mV s^{-1}.

The specific capacitance can be calculated by the following equation: [253]

$$C = \frac{Min(q_a, q_c)}{\Delta V \cdot m_{active}} \tag{3.2}$$

where q_a and q_c are the sums of charge calculated for the anodic and cathodic polarization half cycles, respectively, ΔV is the voltage window of the CV test (1 V), and m_{active} is the total mass of active materials (carbon black for the CB SC and carbon black plus mediators for the mediator SCs). The specific capacitance values are listed in Table 3.2. According to Table 3.2, the maximum specific capacitances of the CB SC and NaI/I_2 SC within a voltage window of 0.0-1.0 V were both obtained at the scanning rate of 25 mV s^{-1}, which were 44.7 and 209.0 F g^{-1} respectively. The increment factors were between 3.9 and 4.7 for the specific capacitance, indicating the enhancement effect of NaI/I_2 mediators. In addition, the data show that the specific charge decreases with increasing the scanning rate for both supercapacitors.

Table 3.2 Specific capacitance of CB SCs and NaI/I_2 SCs at different scanning rates but within the same voltage window of 0.0-1.0 V.

Scanning rate ($mV\ s^{-1}$)	Specific capacitance of CB SC ($F\ g^{-1}$)	Specific capacitance of NaI/I_2 SC ($F\ g^{-1}$)
25	44.7	209.9
50	38.2	159.4
100	35.0	139.8
150	33.5	130.1
200	32.1	140.9

The inset figures in Figure 3.5 show the dependence of the peak current on the scanning rate. A linear relationship can be established between the peak current and the scanning rate, which is a characteristic of ideal SC behavior. The capacitance can also be calculated using the following equation, which is also called differential capacitance [254]:

$$I = \frac{dq}{dt} = \frac{dq}{dV} \cdot \frac{dV}{dt} = C_{diff} \cdot v \tag{3.3}$$

By using Equation 3.3, specific differential capacitance can be evaluated as being 38.2 $F\ g^{-1}$ for the CB SC and 192.0 $F\ g^{-1}$ for the NaI/I_2 SC. These two values are in good agreement with the corresponding values evaluated using Equation 3.2 for the lowest scanning rate. At a high scanning rate, the response of the capacitor is difficult to match the scanning rate, resulting in a lower capacitance. If the specific capacitance at 5 $mV\ s^{-1}$ is used as the baseline, the maximum reduction of the capacitance is 28% for CB SC or 33% for NaI/I_2 SC. It is not a surprise that the reduction of CB SC, an EDLC, is smaller than that of NaI/I_2 SC, a pseudocapacitor because the charge/discharge rate of the former is controlled by diffusion of ions while that of the latter is controlled by both transport of

ions and electrochemical reactions at the interfaces. It is unusual that the difference between the reduction rates are relatively small only 5%. This indicates that although mediator SC is a pseudocapacitor, the charge/discharge rate is comparable to that of an EDLC and that mediator improve the transport and electrochemical reaction rates.

Chae et al. in a review paper proposed to use an electronic band theory to explain why some systems show an ideal pseudocapacitive behavior (rectangular CVs) and others show non-ideal behavior with peaks [255]. The main point is that not all Faradaic processes can result in a capacitive behavior and that the ideal capacitive behavior is in relation with electron delocalization in conducting polymers or in conduction band of semi-conductors whereas the non-ideal behavior is in relation with the localized electronic states in insulator-like redox pairs. A strong evidence for this theory is given in a work by Glarum and Marshall who used an *in situ* electron spin resonance (ESR) method to detect changes of the electronic states of a conducting polymer in H_2SO_4 during CV tests [256]. The dependence of current on voltage in the current supercapacitor may be explained by the band theory as following: at lower voltage range (0.0-0.7 V), the electronic states in the mediators are localized, resulting in a battery-like behavior; however, at higher voltage range (0.7-1.0 V), electron delocalization occurs and the current become independent on the voltage, which is characteristic of a capacitive behavior. Further study on this issue with *in situ* monitoring of the electronic states is necessary for verifying this explanation. To the best of our knowledge, the chemical and electrochemical mechanisms with the mediators in solid-state SCs are still poorly understood. However, basic characteristics of chemistry or electrochemistry in liquid

electrolytes may provide guidance for understanding the processes in solid-state SCs. Possible redox reactions in aqueous solutions are given as follows: [257-258]

$$3I^- - 2e^- \leftrightarrow I_3^- \tag{3.4}$$

$$2I^- - 2e^- \leftrightarrow I_2 \tag{3.5}$$

$$I_3^- - e^- \leftrightarrow \frac{3}{2} I_2 \tag{3.6}$$

Reactions 3.4-3.6 can be recognized as origin of the Faradaic charge/discharge of the NaI/I_2 SC within the voltage range of 0.0-0.7 V.

3.4 GCD results

Results obtained from GCD tests are presented in Figure 3.6. The tests were conducted in a voltage range of 0.0-0.9 V at different current densities. As the current density increased, the SC both charged and discharged at a faster rate. Furthermore, the charge/discharge curves were symmetric, indicating a good reversibility [259]. It is well known that the voltage dependence of charge/discharge curves for an EDLC is linear with time, while in the case of Faradaic charge/discharge, the voltage dependence of the charge/discharge curve is nonlinear with time due to the fact that the reaction rate is a function of voltage [260]. These results were in line with those obtained in the CV tests in that both revealed the effect of Faradaic charge/discharge originated from the redox reactions of the mediators.

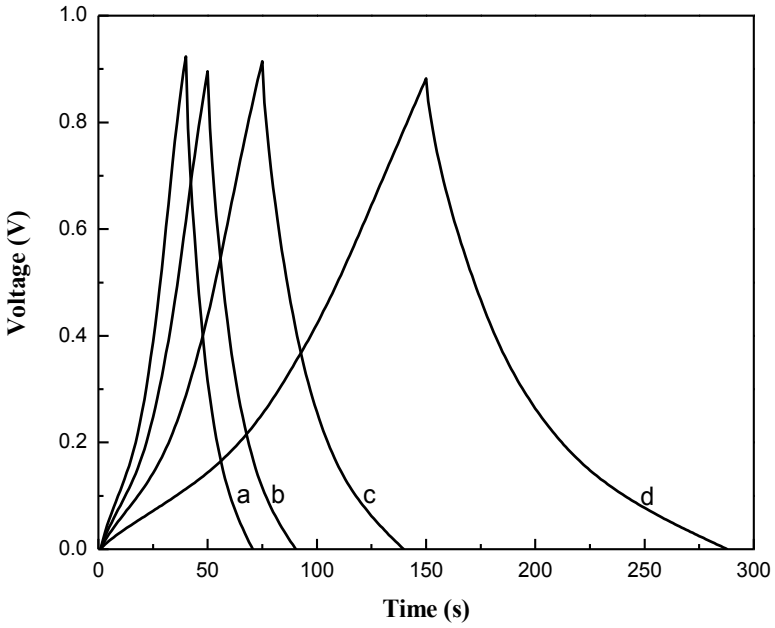

Figure 3.6 Representative cell voltage versus time curves for a NaI/I_2 SC with constant charge/discharge current densities of (a) 20, (b) 15, (c) 10 and (d) 5 mA cm^{-2}.

Specific energy (SE), and average specific power (ASP) are important properties for characterizing the performance of a SC. SE can be calculated from the GCD data using the following equation: $SE = \frac{I\int_{t}^{t+\Delta t} V(t)dt}{m \times 3600}$, where I is the discharge current density, $V(t)$ is the voltage as a function of time, Δt is the discharge time and m is the total mass of active materials in both electrodes [261]. The ASP is defined as $ASP = \frac{SE}{\Delta t}$ [262]. The specific energy as a function of average specific power for the SCs without and with mediators is shown in Figure 3.7, in the form of a Ragone plot. With the addition of NaI/I_2 mediators, the Ragone plot of the SC shifted to a higher specific power and energy region, showing a significant enhancement effect of the mediators. Therefore,

in addition to maintaining a greater charge capacity, the NaI/I_2 SCs can simultaneously deliver a greater specific energy and power.

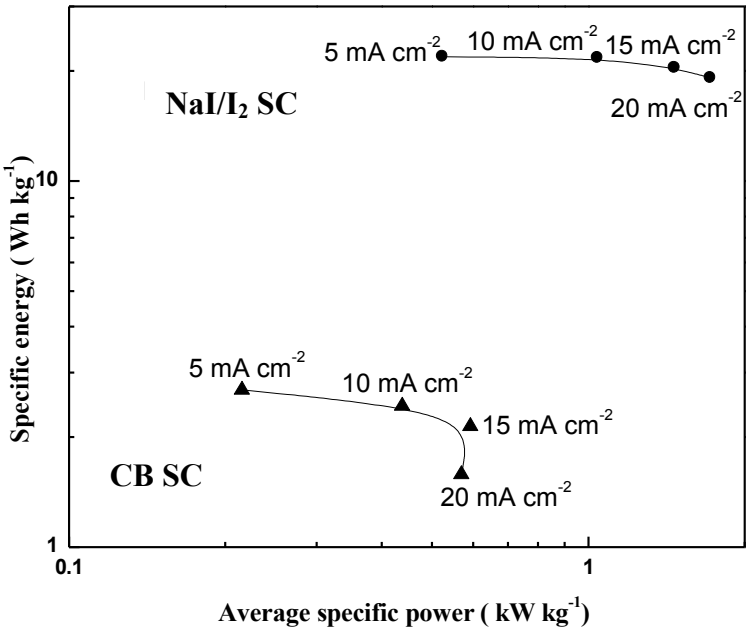

Figure 3.7 Ragone plots for a CB SC (▲) and a NaI/I_2 SC (●).

3.5 Cycling stability and self-discharge

For a SC to be applicable to industry, high cycling stability and slow self-discharge are also important requirements. Therefore, both cycling stability and self-discharge experiments were conducted. Figure 3.8 illustrates the result of a long-term charge/discharge cycling stability. Although there were appreciable variations in the first 3,000 cycles, the total specific charge stabilized after 3,000 cycles maintaining about 90% of its initial charge capacity. The exact mechanism for this phenomenon is the subject of a future study, but it is not a surprising behavior because the mediators may tend to reside

at pores in the amorphous regions and some other preferred sites in the mixture of PEO polymer electrolyte and carbon black [263-264]. Thus, the mediators may start to aggregate in the initial stage of cycling but eventually settle down. Figure 3.9 shows the result of the self-discharge experiment for a NaI/I_2 SC. The supercapacitor was charged to 0.95 V, and the open-circuit voltage was monitored as a function of time over a duration of 50,000 seconds. From the self-discharge curve it can be seen that the present NaI/I_2 SC has a reasonably slow self-discharge rate. Although there's a sharp voltage drop in the first 400 seconds, thereafter, the voltage tends to be stable around 0.7 V.

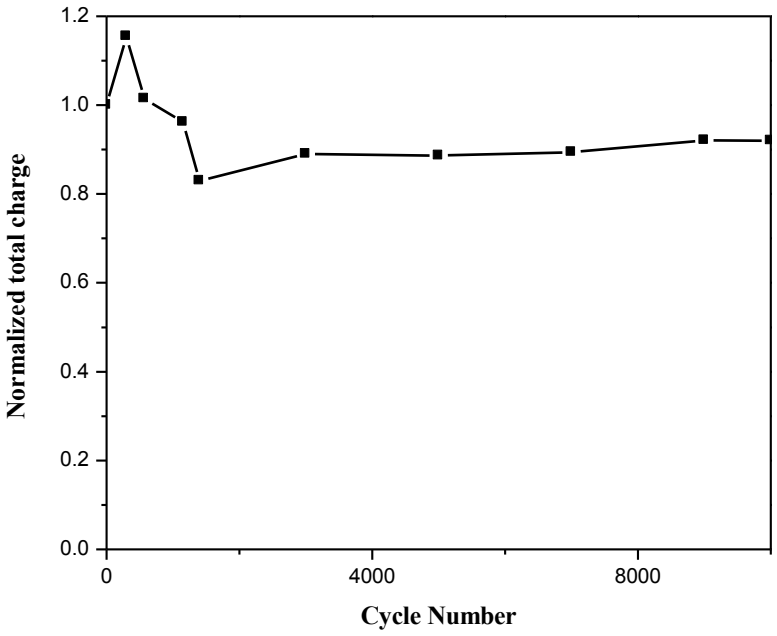

Figure 3.8 Normalized total charge as a function of the charge/discharge cycle number. The charge/discharge current density is 25 mA cm^{-2} and the voltage window is 0.0-1.0 V.

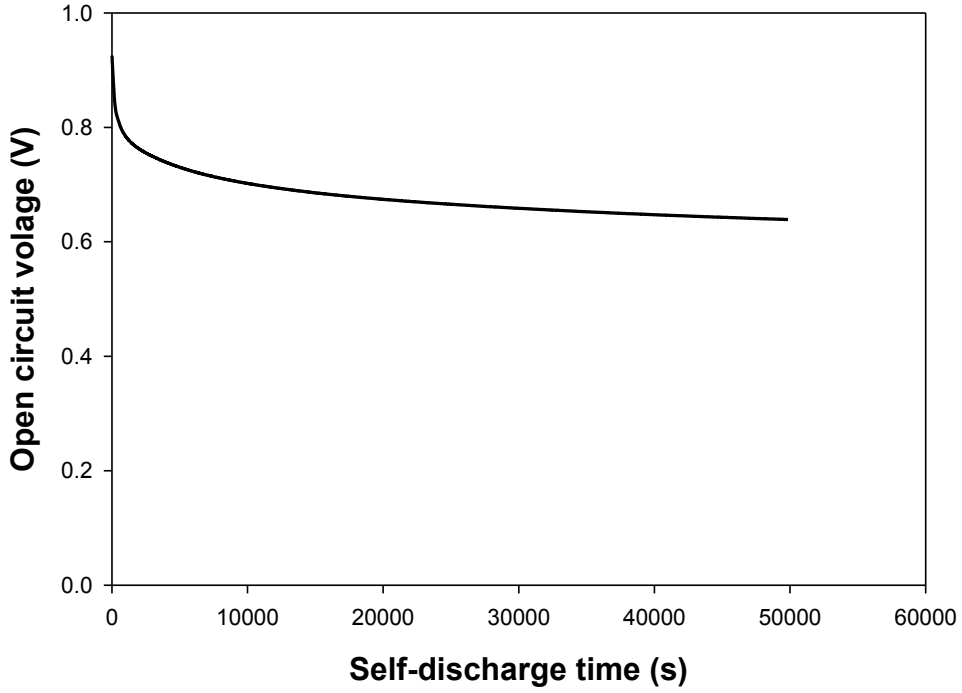

Figure 3.9 The decline of open circuit voltage of a NaI/I_2 SC with time following a charge process to 0.95 V.

3.6 X-ray absorption spectroscopic study

3.6.1 Experimental results

Table 3.3 The components of the electrode samples for XAS measurements.

Sample Name	PEO+$LiClO_4$+EC (mg)	I_2 (mg)	NaI (mg)	Carbon black (mg)
I_2 electrode	53.5	99.1	0	5.4
I_2 flake	0		0	0
NaI electrode	61.2	0	109.0	6.1
NaI powder	0	0		0
NaI/I_2 electrode	179.5	9.4	95.5	13.9

The baseline I-K-edge k^2-weighted EXAFS spectra and their phase uncorrected Fourier transforms (FT) for the I_2 electrode and I_2 flake are displayed in Figure 3.10. A

comparison of experimental and simulated data is shown in Figure 3.11. The k^2-weighted EXAFS spectra and their phase-uncorrected Fourier transforms of the NaI electrode and NaI powder are displayed in Figure 3.12. A comparison of experimental and simulated data is displayed in Figure 3.13.

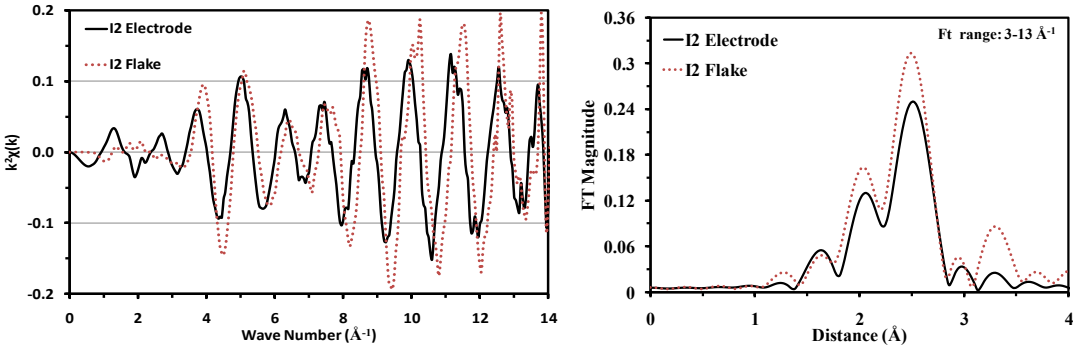

Figure 3.10 Baseline I-K-edge k^2-weighted EXAFS spectra and their phase-uncorrected Fourier transforms of I_2 electrode and I_2 flake.

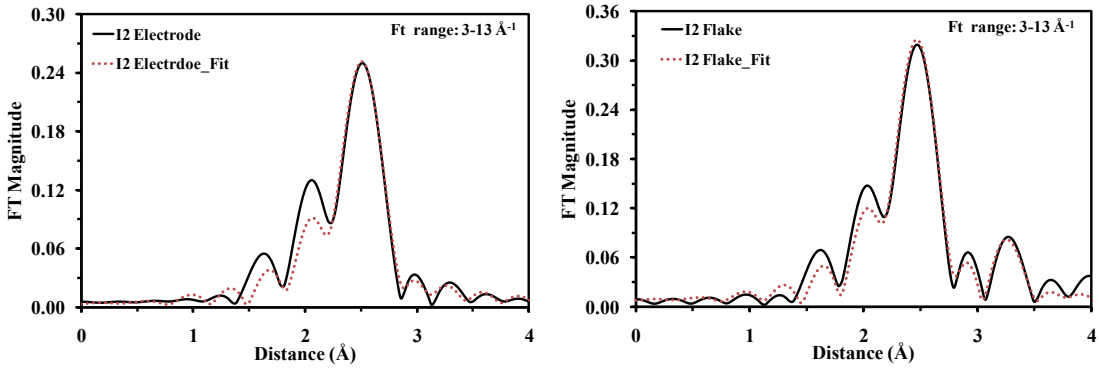

Figure 3.11 Fourier transforms of measured and simulated k^2-weighted EXAFS for the I_2 electrode and I_2 flake.

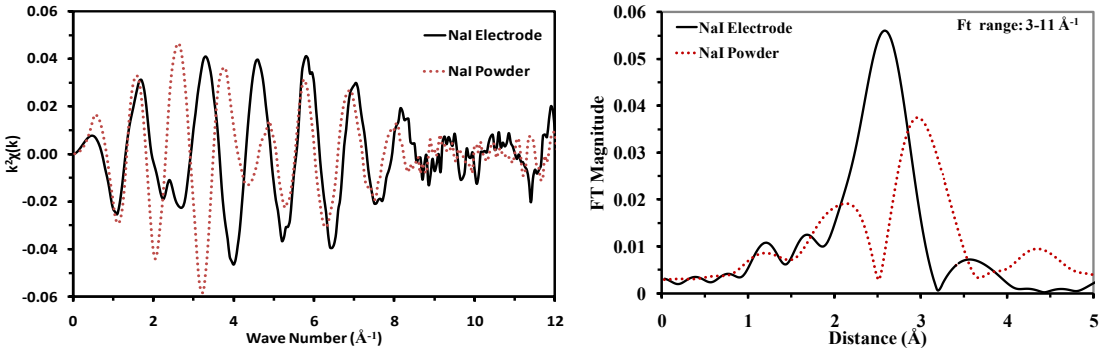

Figure 3.12 Baseline I-K-edge k^2-weighted EXAFS and their phase-uncorrected Fourier transforms of the NaI electrode and NaI powder.

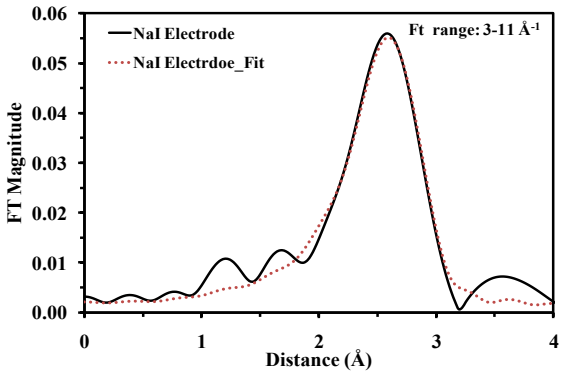

Figure 3.13 Fourier transforms of measured and simulated k^2-weighted EXAFS for the NaI electrode.

Three groups of *in situ* I-K-edge XAFS and XANES spectra, which are given in Figure 3.14, were recorded for the mediator SC. The first group was recorded at open circuit voltage (OCV, -0.08 V). The mediator SC was then charged from -0.08 to 0.80 V at 5 mA, and a second group of spectra was recorded. The third group was done after discharge the SC to its OCV at 5 mA. *In situ* k^2-weighted EXAFS spectra extracted and their phase uncorrected Fourier transforms of XAFS spectra provided in Figure 3.14 are shown in Figure 3.15. Comparisons of Fourier transforms of measured and simulated k^2-weighted EXAFS for the mediator SC are shown in Figure 3.16. The structural and

energetic parameters of the materials under different conditions are summarized in Table 3.3.

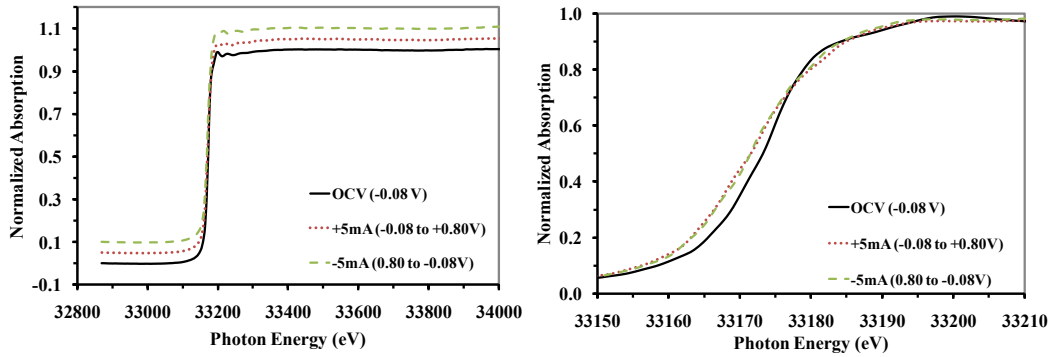

Figure 3.14 *In situ* I-K-edge XAFS spectra (left) and XANES region (right) of the spectroelectrochemical cell polarized to different potentials.

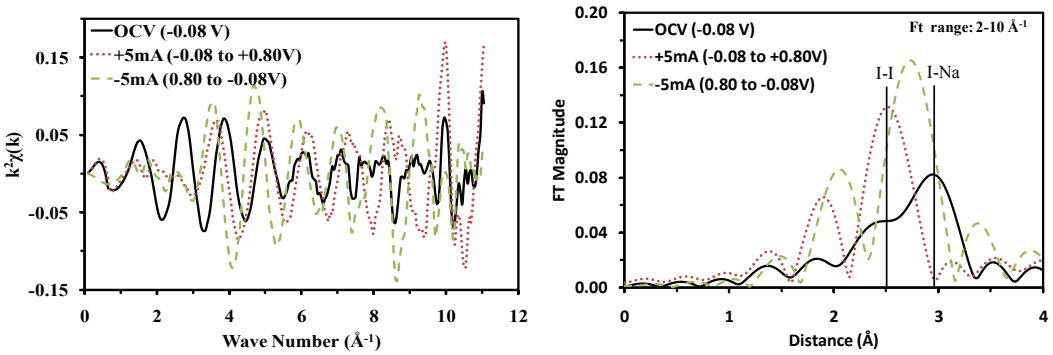

Figure 3.15 *In situ* k^2-weighted EXAFS spectra extracted and their phase uncorrected Fourier transforms of XAFS spectra described in Figure 3.14.

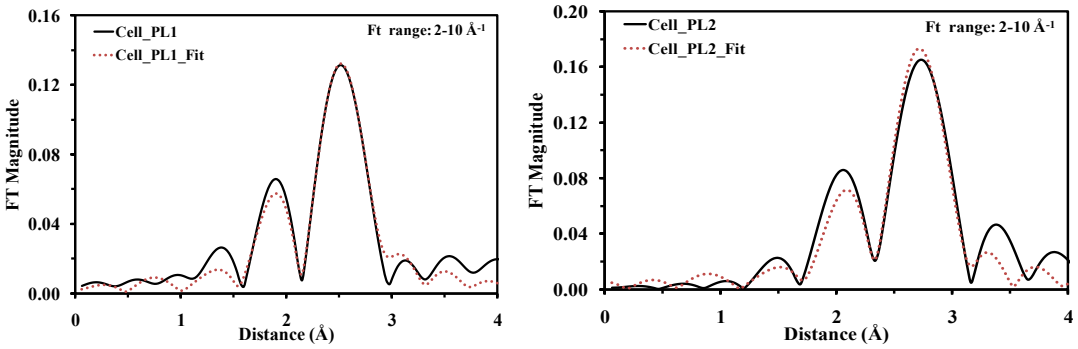

Figure 3.16 Experimental and Fourier-transformed data for the mediator SC after charging to 0.80 V (left), and discharge to -0.08 V (right).

Table 3.4 Summary of local structure parameters for I_2 flake, I_2 electrode, and Na/I_2 electrode polarized at different potentials.

Sample	Bond	N	R (Å)	σ^2 (10^{-3} Å^2)	E_o (eV)
I_2 flake	I-I	1	2.723(3)	3.2(4)	5.7(7)
I_2 electrode	I-I	1	2.754(8)	4.3(6)	7.1(19)
NaI Electrode	I-Na	1.7(2)	3.086(10)	13.9(15)	4.2(8)
NaI/I_2 electrode charged from -0.08V to +0.8V	I-I	1.3(2)	2.776(10)	8.9(15)	4.0(12)
NaI/I_2 electrode discharged from +0.8V to -0.08V	I-I	2.4(3)	2.944(9)	10.7(14)	7.4(9)

N-Coordination number, R-first shell distance between atoms, σ^2 – first shell disorder, E_o- inner potential.

3.6.1 Result analysis

According to Ref. 266, in liquid state, the first shell distance between iodine atoms is only 2.70 Å and transformation from liquid to solid phase will increase the first shell distance. The first shell distance and disorder of iodine in the electrode relative to iodine in the flake increased from 2.72 to 2.75 Å. The first shell distance for iodine flake corresponds to the intramolecular distance within the iodine molecule and agrees with the literature reported value of 2.72 Å [264-267]. In addition it is clear that iodine in the electrode is present in the solid state rather than in the liquid state [266]. The FT data for

the I_2 flake (Figure 3.10) display a strong double peak structure in the 1.8-2.8 Å region and a second much weaker double peak structure in the 2.8-3.6 Å region. However, the FT data for the I_2 electrode consists of only the first double peak structure without a contribution from the second shell of atoms. This importantly indicates lack of a contribution from the second shell of atoms which confirms that iodine in the electrode is present with a high degree of structural disorder between molecules within a single layer. In fact, it is desired to achieve a highly dispersed distribution for iodine mediators within polymer electrolyte because this will provide a high utilization rate for the mediators in the electrodes of a supercapacitor.

The EXAFS oscillations and the radial structure function of NaI in the electrode differ significantly from those of NaI in powder form (Figure 3.12) indicating a structural modification as a result of possible interactions with PEO and other components in the electrolyte. Iodine in the electrode, is coordinated with 1.7(2) Na at a distance of 3.09 Å with a moderate degree of disorder of 0.0139 ± 1.5. However, an XRD study [268] of a PEO-NaI complex revealed that iodine in this complex is coordinated with 1 Na at 2.91 Å and 1 Na at 3.20 Å which corresponds to 2 Na at an average distance of 3.05 Å. The present EXAFS results for the NaI electrode are close to those reported in the XRD study. The small differences between the EXAFS and XRD results are likely due to the fact that our electrode contains $LiClO_4$, EC, and CB in addition to be PEO. The slightly lower XAFS-based coordination number of 1.7(2) relative to the XRD-based coordination number of 2 could be due to the presence of iodide ions I^-.

In the *in situ* study, the XAFS spectra were collected while holding the cell at the end the potential range of the charge and discharge cycles. The XAFS spectra (Figure 3.14)

are featureless due, in part, to the large natural width of the I-K-edge (10.6 eV) [269-270]. However, the edge energy at half-height shifts to lower energy when the cell is charged and discharged relative to the initial state of the cell when it was held at OCV. The shift is a clear indication of the change in oxidation state and/or local structure of iodine as a function of cell condition. The EXAFS oscillations (left figure in Figure 3.15) clearly show significant differences between the OCV, charged and discharged states of the supercapacitor. The Fourier transforms (right figure in Figure 3.15) show a clear distinction in the local coordination geometry of iodine depending on the polarization condition of the supercapacitor. The FT data for the OCV condition clearly shows contributions from I-I and I-Na as one would expect. However, upon charging, the I-Na contribution disappears while the I-I contribution is significantly enhanced. Furthermore, upon discharging the charged cell, the I-I contribution shifted to a higher distance and its intensity is further enhanced.

Comparisons of Fourier transforms of measured and simulated k^2-weighted EXAFS for the SC charged at 5 mA from -0.08 to 0.80 V and the SC discharged at 5 mA from 0.80 to -0.08 V are shown in Figure 3.16. Due to the limited data range in the case of the cell held at OCV, it was not possible to uniquely extract the local structure parameters for the I-I and I-Na species. Upon charging, I is coordinated with 1.3(2) I atoms at a distance of 2.78(1) Å which is only slightly larger than the I-I distance 2.75 Å for the case of I_2 in electrode. Such a distance is only slightly larger than that observed for solid I_2 but is significantly less than that observed for I_3^-, which is normally reported near 2.93 Å. However, the coordination number is very close to that for I_3^-, which is 1.33.

Upon discharging the SC, iodine is coordinated with 2.4(3) iodine atoms at a distance of 2.94(1), which is significantly greater than that reported for solid I_2 (2.72 Å) but less than that for NaI (3.09 Å). However, such a distance is close to those reported for polyiodide ions such as I_3^- in $KI_3 \cdot H_2O$ (2.93Å) [271] or in $[C_5H_5)_2Fe]I_3$ (2.93 Å) [257]. The increase in the coordination distance from 2.78 to 2.94 Å is consistent with the increase in the coordination number from 1.3(2) to 2.4(3) and suggests the possible formation of clusters and/or linear chains containing large number of iodide atoms.

These results suggest that I^- is oxidized to I_2 according to $2I^- \rightarrow I_2 + 2e^-$ during the first charge cycle while I_2 is reduced to I_3^- according to $3I_2+2e^- \rightarrow 2I_3^-$ during the discharge cycle. These redox reactions have been reported to occur at the carbon/iodide interface giving extremely high capacitance [257].

3.7 Conclusions

1. All-solid-state mediator SCs were fabricated by using Nafion membrane as the separator, PEO/$LiClO_4$ as the solid-state electrolyte, and dispersed NaI/I_2 mediators as active materials.

2. The addition of NaI/I_2 mediators improved the specific energy and specific power of the SC by ~8 and ~4 folds respectively in comparisons with those of the CB SC, showing a significant enhancement effect of the mediators.

3. The all-solid-state NaI/I_2 supercapacitor shows clear battery-like behavior at lower polarization and capacitive behavior at high polarization owing to localization and de-localization of the electronic states in the composite electrode.

4. The *in situ* XAS study provides a better understanding of the charge/discharge mechanism of the NaI/I_2 mediator SC, that is, over the voltage range between 0.0-1.0 V, the redox states of mediators vary between I_3^- and I_2.

CHAPTER 4 ALL-SOLID-STATE MEDIATOR SUPERCAPACITOR WITH PVDF/LiTFS MEMBRANE AS THE SEPARATOR

In Chapter 3, all-solid-state SCs were fabricated using Nafion membranes as the separator, and a PEO polymer electrolyte doped with NaI/I_2 mediators as the electrodes [273-274]. Previous results have shown that SCs prepared using this novel method can achieve high specific capacitance, high specific power, high specific energy, long cycle life, and low self-discharge. This demonstrates that in addition to carbon materials, metal oxides, and electronically conducting polymers, mediator-doped polymer electrolytes are a fourth type of material that can be utilized to fabricate all-solid-state SCs. The reasons that a Nafion membrane was chosen to be the separator are its low resistance, good mechanical strength, thermal stability, and chemical stability. However, the voltage window for Nafion-based SCs is between 0.0 and 1.0 V or between -1.0 and 0.0 V, which limits full utilization of the high valence states of the active materials. Thus, in this chapter, a PVDF/LiTFS membrane was made to replace the Nafion membrane as the separator. Because the membrane and the mediator-doped PEO electrolytes did not contain water, it was envisioned that the voltage window could be greater than 1.0 V. The performance of the SC was evaluated using cyclic voltammetry (CV) and galvanostatic charge/discharge (GCD) methods. The main objective was to demonstrate that with a PVDF/LiTFS membrane as the separator, a high performance all-solid-state SC could be realized.

4.1 Experimental

4.1.1 Preparation of PVDF/LiTFS membrane

PVDF powder (M.W.=534,000, Sigma-Aldrich) was mixed with LiTFS powder (~99.995%, Sigma-Aldrich). The mixture was dissolved in acetone (99.9%, Sigma-Aldrich) and then stirred at 60°C for approximately 4 hours until it became a homogeneous translucent gel. The mass ratio of PVDF to LiTFS was 1:1. The gel was cast into evaporation dishes and allowed to dry for 12 hours to obtain a thin, semi-transparent PVDF/LiTFS membrane.

4.1.2 Preparation of PEO-based suspensions for electrode loadings

Three types of electrode suspension, composed of PEO/$LiClO_4$ and active materials, were prepared with the method described in Section 3.1.2. The contents of the three types of electrode suspensions, namely, the carbon black (CB) suspension, the NaI/I_2/CB suspension, and the $K_3Fe(CN)_6$/$K_4Fe(CN)_6$/CB suspension are listed in Table 4.1.

Table 4.1 Contents of three types of electrode suspension.

Suspension name	Composition (wt%)						
	PEO	$LiClO_4$	CB	NaI	I_2	$K_4Fe(CN)_6$	$K_3Fe(CN)_6$
Carbon black	61.4	18.6	20.0	0	0	0	0
NaI/I_2/CB	61.4	18.6	2.0	6.7	11.3	0	0
$K_4Fe(CN)_6$/ $K_3Fe(CN)_6$/CB	61.4	18.6	2.0	0	0	9.5	8.5

4.1.3 Preparation of supercapacitor assemblies

A nanofoam carbon paper was acquired from Marketech International Inc. The specification of the carbon paper is as follows: density, 0.25 to 1.0 g cm^{-3}; BET surface area, 400 $m^2 g^{-1}$; average pore size, 0.7 nm; electrical resistivity, 0.010 to 0.040 ohm-cm. The prepared PEO-based suspension was dropped on a piece of nanofoam carbon paper. After loading with suspensions, the electrodes were dried naturally in air for approximately 12 hours and then kept in a plastic bag.

To make a SC assembly, the PVDF membrane prepared in Section 4.1.1 was used as the separator. Two carbon electrodes (2.0 cm^2) loaded with active materials and polymer electrolytes, and a PVDF membrane were pressed at approximately 1,000 psi for 1 minute to obtain a sandwich-structured SC, as shown in Figure 4.1.

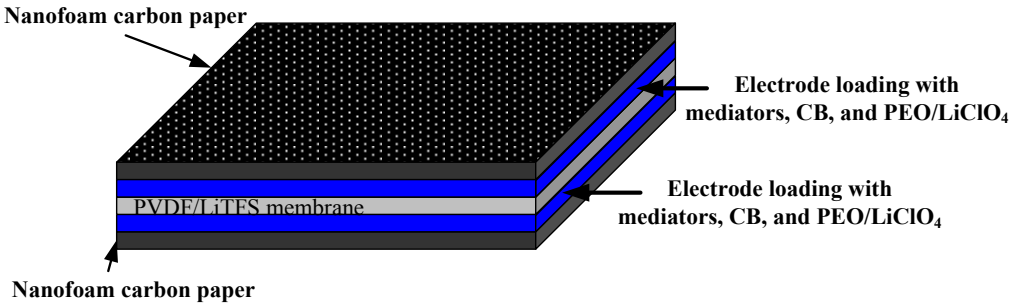

Figure 4.1 Schematic of an all-solid-state supercapacitor assembly.

4.1.4 Characterization

Lateral or in-plane conductivities of the PVDF/LiTFS and Nafion films were evaluated using a four-electrode AC impedance method described in detail in a previous publication [240].

Cyclic voltammetry (CV) and galvanostatic charge/discharge (GCD) measurements were conducted at ambient temperature using solid-state electrochemical cells or SC assemblies in the form shown in Figure 4.1. The SC was connected to a potentiostat (Gamry) with a frequency response analyzer module interfaced to a personal computer. The performance of the SCs was studied using CV (voltage range of 0.0 to 3.0 V, scanning rate of 10 to 200 mV s^{-1}) and GCD (charge/discharge current density of 10 to 25 mA cm^{-2}).

4.2 Conductivity analysis of the PVDF/LiTFS membrane

The conductivity of the membrane separator in a solid-state SC is crucial to its performance. Therefore, the conductivity of the PVDF/LiTFS membrane was measured using the four-electrode EIS method. In addition, for comparison, the conductivity of a commercial Nafion® 117 membrane was also evaluated with the same method, and the data are given in Table 4.2. Before conducting the conductivity measurement with the Nafion membrane, it was fully hydrated and activated in 1 mol L^{-1} H_2SO_4 for 12 hours.

Table 4.2 Conductivities of PVDF/LiTFS and Nafion 117 membranes at ambient conditions.

Membrane	Conductivity, S cm^{-1}	Average conductivity, S cm^{-1}
PVDF/LiTFS	1.730×10^{-2}	1.74×10^{-2}
	1.747×10^{-2}	
	1.745×10^{-2}	
Nafion 117	2.715×10^{-2}	2.83×10^{-2}
	2.734×10^{-2}	
	3.041×10^{-2}	

As shown in Table 4.2, the average conductivity values for the PVDF/LiTFS and Nafion membranes are 1.74×10^{-2} and 2.83×10^{-2} S cm^{-1} at 25°C, respectively. The conductivity of the PVDF/LiTFS membrane is lower than that of a fully hydrated Nafion membrane. However, the relatively high conductivity and stability of the PVDF/LiTFS membrane have made them outstanding among the currently studied lithium-ion-conducting polymer membranes [275-276]. On the other hand, the ionic conduction in Nafion membranes depends on the hydration level, which means that if it is dehydrated under ambient conditions, the conductivity will decrease [277]. The ionic conduction in polymers containing lithium ions is believed to rely on the diffusion of lithium ions, which have a small ionic radius, through the free volume in the polymer [278]. This implies that with a PVDF/LiTFS membrane, a high ionic conductivity can be obtained without the presence of water in the polymer.

4.3 Cyclic voltammetry

4.3.1 Supercapacitors with carbon black

To establish a reference for evaluating the effects of the two kinds of mediators, an all-solid-state SC that contained only carbon black (CB) as the active material was assembled, and its performance was evaluated using CV. Figure 4.2 illustrates the CVs of a CB SC at different scanning rates. No redox peaks were observed in the CVs of the CB SC, indicating that this kind of SC is a typical EDL SC. Figure 4.2 also shows that the current density increased as the scanning rate decreased. It is widely accepted that the CV of an ideal EDL SC is rectangular-shaped. However, for the CB SC in the present configuration, the CVs at different scanning rates were not rectangular-shaped, showing

poor reversibility [279]. This poor reversibility may result from a high series resistance (10.9 Ω) of the CB SC.

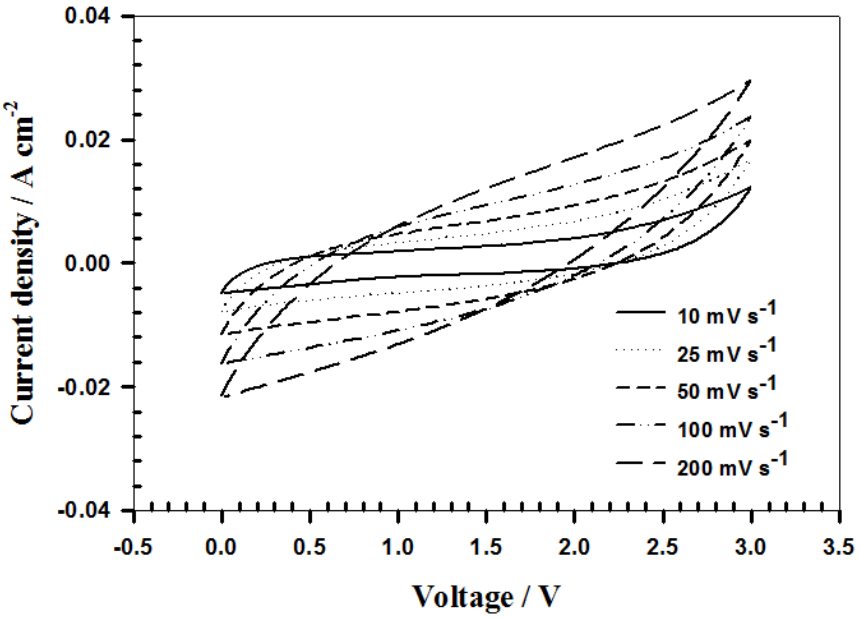

Figure 4.2 Cyclic voltammetry curves as a function of potential scanning rate for a supercapacitor with carbon black as the active material.

Table 4.3 Summary of the specific capacitance for the carbon black SC, the NaI/I_2/CB SC, and the $K_4Fe(CN)_6/K_3Fe(CN)_6$/CB SC.

Scanning rate, mV s^{-1}	Specific capacitance, F g^{-1}		
	Carbon black	NaI/I_2/CB	$K_4Fe(CN)_6/K_3Fe(CN)_6$/CB
10	40.7	209.0	138.8
25	20.4	145.4	99.8
50	10.2	107.5	82.5
100	7.9	89.0	50.4
200	5.8	52.9	36.5

According to the CV results, the specific capacitance with respect to the active material is calculated using Equation 3.2 [279]. The specific capacitance values are listed in Table 4.3. According to Table 4.3, the specific capacitance of the CB SC was 40.7 F g^{-1} at a scanning rate of 10 mV s^{-1}, and the capacitance decreased upon increasing the scanning rate.

4.3.2 Supercapacitors with sodium iodide/iodine (NaI/I_2) mediators

Figure 4.3 shows CV curves for a NaI/I_2 SC at scanning rates from 10 to 200 mV s^{-1}. All of the CVs showed a slightly distorted rectangular shape without distinct, sharp redox peaks [138]. In addition, both the absence of sharp redox peaks and the presence of high current density compared to that of the CB SC are characteristic features of electrochemical materials with pseudocapacitance [142]. The specific capacitance was 209.0 F g^{-1} at a scanning rate of 10 mV s^{-1}. The specific capacitances of the NaI/I_2 SC were 5 to 10 times greater than those of the CB SC depending on the scanning rate, showing an enhancement effect of the NaI/I_2 mediators due to the pseudocapacitance. Moreover, with the NaI/I_2 SC, the changes of current polarity when the voltage scan was reversed were much faster than those of the CB SCs, indicating a lower internal resistance and good reversibility [139]. This was confirmed by the EIS results (data not shown), which showed that the internal resistance was only 3.6 Ω. In this system, the mediators behave as both conducting charge carriers and charge storage materials. According to the discussion in Ref. [273], the pseudocapacitance of the NaI/I_2 SC originates from the following redox reactions: $I_2(s) + 2e^- = 2I^-$ and $I_3^- + 2e^- = 3I^-$. However, for the SC with NaI/I_2 mediators, no sharp redox peaks were observed in the CV results, revealing a typical capacitive behavior that can be found in other systems with

pseudocapacitance [280-282]. The addition of mediators increases the capacitance by contributing pseudocapacitance, which is a dominant component in the overall capacitance. Moreover, it can also be concluded from Figure 4.3 that the current density increased proportionally with the scanning rate, which is also considered a typical characteristic of an EDL SC [283].

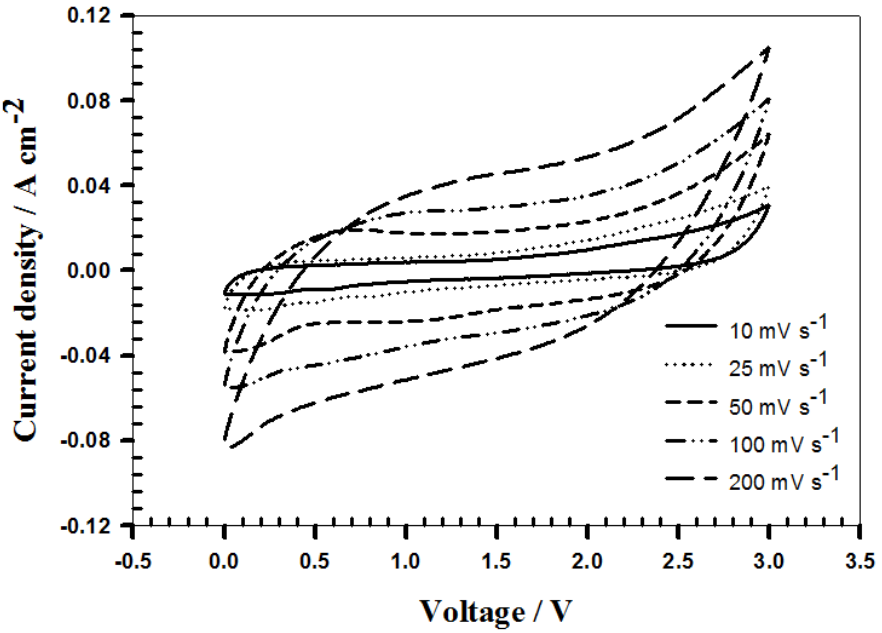

Figure 4.3 Cyclic voltammetry curves as a function of potential scanning rate for a supercapacitor with NaI/I_2/CB as the active material.

4.3.3 Supercapacitor with $K_3Fe(CN)_6/K_4Fe(CN)_6$ mediators

$K_3Fe(CN)_6$ and $K_4Fe(CN)_6$are known to engage in fast electron transfer between themselves [22]. The carbon nanofoam electrodes employed contained PEO/$LiClO_4$, $K_3Fe(CN)_6/K_4Fe(CN)_6$, and carbon black. Figure 4.4 shows CV curves at scanning rates from 10 to 200 mV s^{-1}. The shapes of the CV curves for the $K_3Fe(CN)_6/K_4Fe(CN)_6$ SC were similar to those observed for the NaI/I_2 SC and other systems with pure capacitive

behavior. However, a pair of broad redox peaks appeared at approximately 0.5 V. The redox peaks are believed to be related to the redox reaction $K_3Fe(CN)_6 + e^- + K^+ = K_4Fe(CN)_6$ [284].

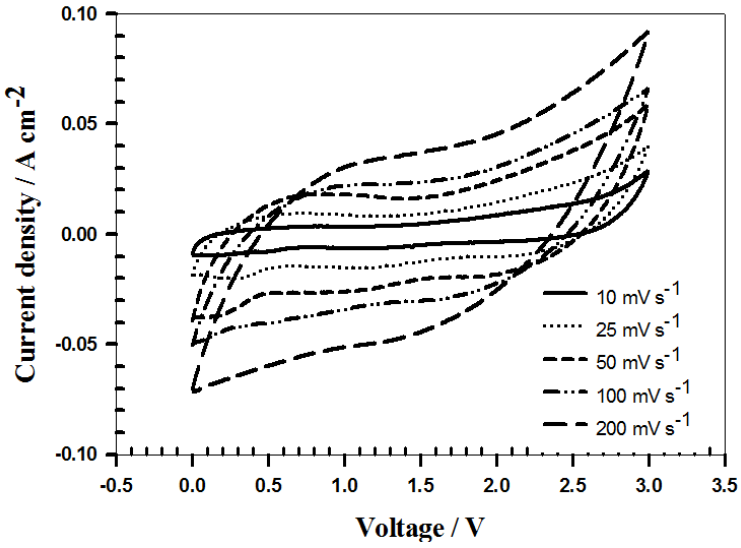

Figure 4.4 Cyclic voltammetry curves as a function of potential scanning rate for a supercapacitor with $K_3Fe(CN)_6/K_4Fe(CN)_6$/CB as the active material.

The specific capacitance of the $K_3Fe(CN)_6/K_4Fe(CN)_6$ SC as a function of the scanning rate is also listed in Table 4.3. The specific capacitance was 138.8 F g^{-1} at a scanning rate of 10 mV s^{-1}, which is much less than 209.0 F g^{-1}, the specific capacitance of the NaI/I_2 SC at the same scanning rate. It is worth noting that the theoretical specific charge of the $K_3Fe(CN)_6/K_4Fe(CN)_6$ mediators (in a molar ratio of 1:1) is 138.3 C g^{-1}, which is smaller than the theoretical specific charge of 239.1 C g^{-1} for the NaI/I_2 mediators (in a molar ratio of 1:1). The specific capacitance increased as the scanning rate decreased, which is a behavior similar to both the CB SC and NaI/I_2 SC. However, for this $K_3Fe(CN)_6/K_4Fe(CN)_6$ SC, the specific capacitance was 3 to 6 fold that of the CB SC,

depending on the scanning rate. Thus, the enhancement effect was not as pronounced as with NaI/I_2 mediators.

4.4 Galvanostatic charge/discharge

Galvanostatic charge/discharge (GCD) tests were also conducted to evaluate the performance, specifically the specific energy and specific power of SCs with NaI/I_2 and $K_3Fe(CN)_6/K_4Fe(CN)_6$ mediators, and the results are shown in Figure 4.5 (A) and (B). The tests were conducted in a voltage range between 0.0 to 2.5 V at charge/discharge current densities of 10, 15, 20, and 25 mA cm^{-2}. Figure 4.5 shows that for both SCs, regardless of the value of the charge/discharge current density, the discharge curves were essentially linear over the entire discharge period except for a small sharp drop in the very initial stage, which corresponds to the ohmic loss due to series resistance. The linearity of the discharge curves indicated that the mediator SCs described in this work have typical capacitive characteristics and resemble an EDL SC.

From the discharge profiles of the mediator SCs, the specific energy and the average specific power were calculated. The specific energy values as a function of specific power for both mediator SCs are shown in Figure 4.6 in the form of a Ragone plot. In addition to maintaining a greater charge capacity, both mediator SCs could simultaneously deliver a high specific energy and power. The NaI/I_2 SC exhibited a better performance in terms of specific energy and specific power than the $K_3Fe(CN)_6/K_4Fe(CN)_6$ SC. This is in line with results of the CV tests. The maximum specific energy of the NaI/I_2 SC with a PVDF separator was 49.1 Wh kg^{-1} with respect to the mass of active material, which is about 2 times the maximum specific energy of an SC with a Nafion separator and NaI/I_2 mediator [273]. The higher specific energy for SCs

with a Nafion separator is mainly due to the greater voltage window for the SC with a PVDF/LiTFS separator compared to SCs with a Nafion separator.

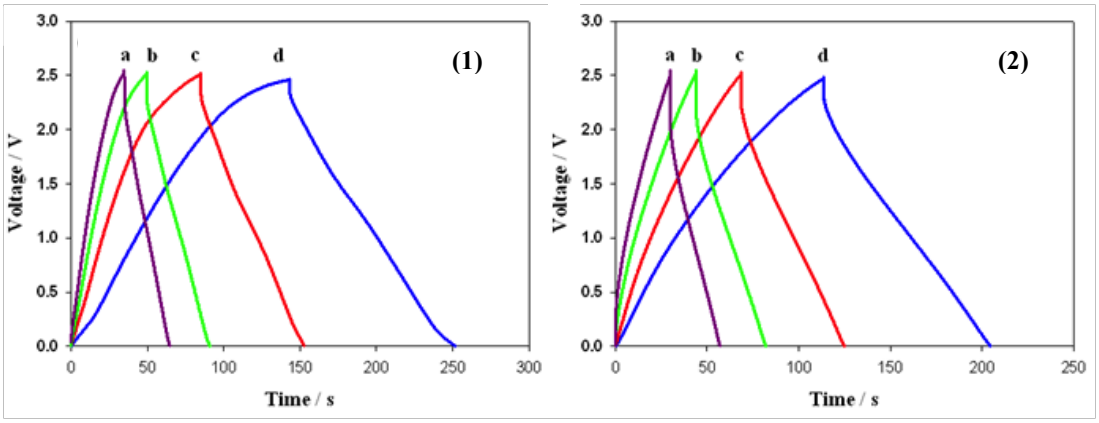

Figure 4.5 Representative cell voltage versus time curves for: (1) NaI/I_2/CB SC and (2) $K_3Fe(CN)_6/K_4Fe(CN)_6$/CB SC, with constant charge/discharge current densities of (a) 25, (b) 20, (c) 15 and (d) 10 mA cm^{-2}.

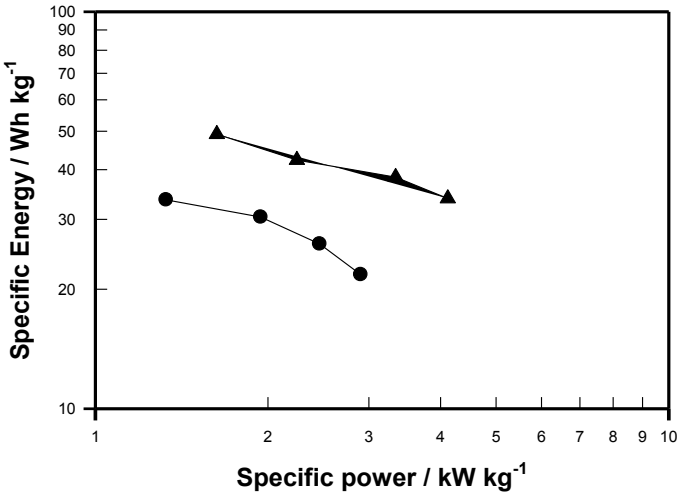

Figure 4.6 Ragone plots for a NaI/I_2/CB SC (▲) and $K_3Fe(CN)_6/K_4Fe(CN)_6$/CB SC (●).

4.5 Effects of mediator concentration on the performance

In a previous publication [274] on the SCs with Nafion membranes as the separator, the effect of the concentration of NaI/I_2 mediators on specific capacitance is discussed. The results showed that the specific capacitance was increased from 107 to 150 F g^{-1} when the loading of the mediators was increased from 5 to 33%. A cooperative effect of the electrode components, electrolyte, carbon black and mediators was used to explain this phenomenon. The electron transfer among the active materials is more difficult at a lower concentration than at a higher concentration. Furthermore, unlike the case of other types of SCs where ion access/transport to the active materials/sites dominates the charge/discharge process, in the present SCs, where the mediators are dispersed among ions in the solid-state electrolyte, the electron transfer among the active materials dominates the charge/discharge process.

However, is this still true for a mediator SC with PVDF membranes as the separator? In this section, the effect of the mediator concentration on the performance of the NaI/I_2 SCs is investigated.

Four types of SCs with mediator concentration of 5%, 10%, 20%, and 30% were prepared, and the electrochemical performance were evaluated with GCD. The voltage range for GCD tests was: 0-2.5 V, and the charge/discharge current densities were 10, 15, 20, 25 mA cm^{-2}, respectively.

The dependence of specific capacitance, specific power, and specific energy on the mediator concentration at various charge/discharge current densities are given in Figures 4.7-4.9. Since there are three types of performance (specific capacitance, energy and

power) and two parameters (concentration of mediators and the charge/discharge current density), a number of conclusions can be made from Figures 4.7-4.9 as following:

1. Specific capacitance and energy increased with the decrease of charge/discharge current density. This phenomenon is in agreement with that of the CV results, which shows that both specific capacitance and energy are better when the scanning rate is slower.
2. From Figure 4.7 it can be concluded that for mediator SCs with PVDF/LiTFS as the separator, the greater the mediator concentration, the greater the specific capacitance. This is also in line with result of SCs with Nafion membrane as separator.
3. The specific energy of the mediator SC first increases, then decreases with the increase of the mediator concentration. The maximum energies were obtained when the mediator concentration is 20%.
4. Similarly to the specific energy, there's a maximum value for the specific power.

In Figure 4.10, the conductivity of PDVF electrolyte doped with NaI/I_2 mediator is plotted as a function of the concentration. It is very interesting to observe a similar trend to that of specific energy and power. This fact simply means that charge transfer in the mediator-doped polymer electrolyte becomes slower at a concentration greater than 20%. However, according to Dahms-Ruff equation (Equation 3.1), the conduction of a media containing mediators should increase with increase of the concentration. A rational explanation is that the concentration in the Dahms-Ruff equation actually means activity or concentration of dissociated mediators excluding aggregated mediators. When the concentration of mediator is small, they are readily solvated and dissociated and can

contribute to charge transfer. However, if the concentration is above a limit, association will prevail and render a lower concentration of solvated mediator or a lower activity. Because of the higher resistance, the average power of the device will be lower according to Equation 1.8. If all the mediators are active and effective the specific capacitance should be proportional to the concentration. However from Figure 4.7, the specific capacitance increases slightly with concentration. Because the active or effective mediator decreases above a concentration of 20%, it is likely that the charge shielding or dielectric constant increases. Because of relatively low power at a concentration above 20%, the charge tends to release at a lower voltage as being manifested by the slight asymmetrical charge/discharge curves and the specific energy becomes lower at a concentration above 20%.

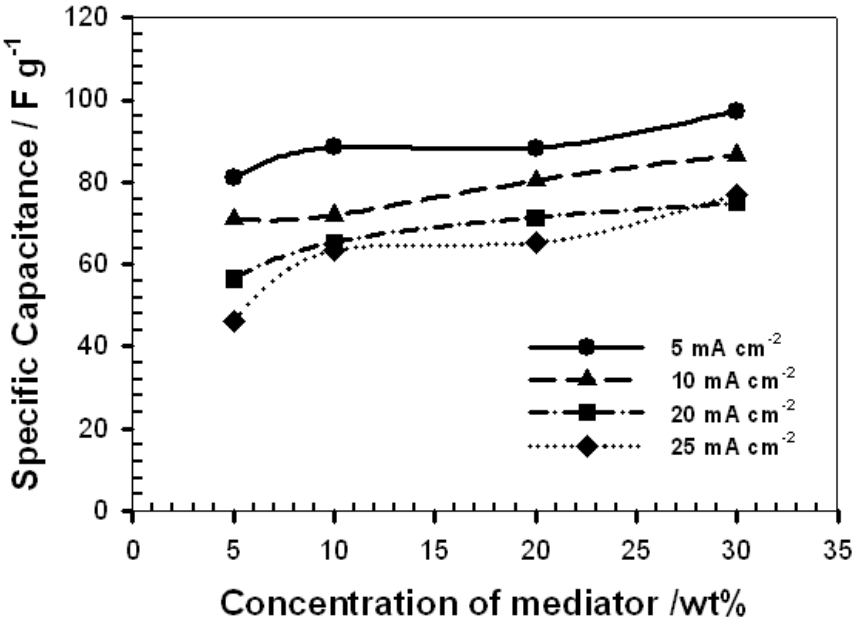

Figure 4.7 Dependence of specific capacitance of the NaI/I_2 mediator SCs on the concentration of the mediators at various charge/discharge current densities.

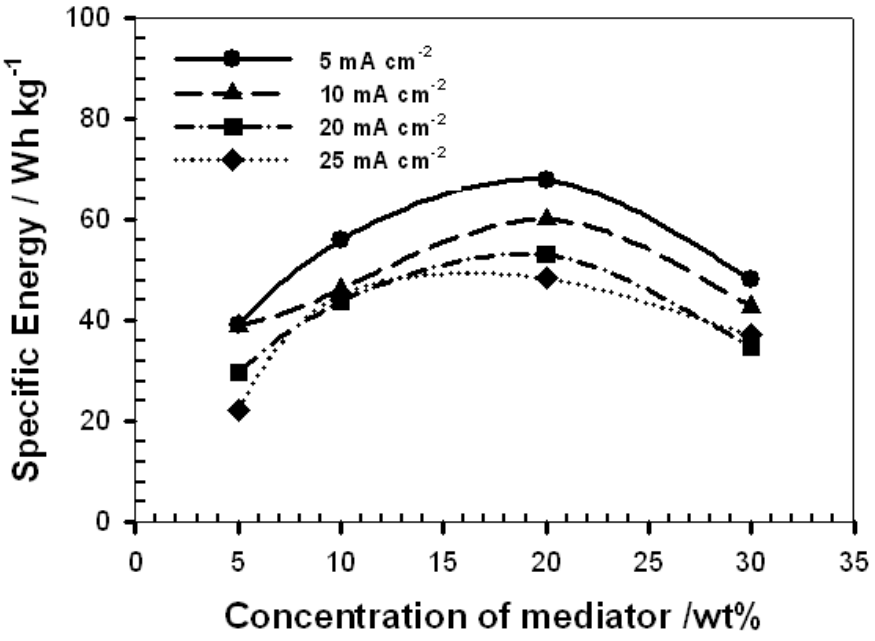

Figure 4.8 Dependence of specific energy of the NaI/I_2 mediator SCs on the concentration of the mediators at various charge/discharge current densities.

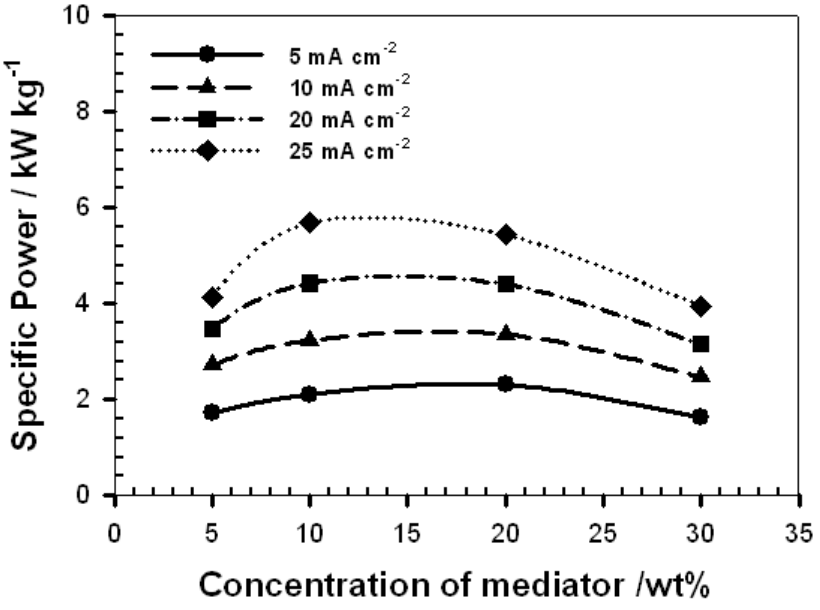

Figure 4.9 Dependence of specific power of the NaI/I_2 mediator SCs on the concentration of the mediators at various charge/discharge current densities.

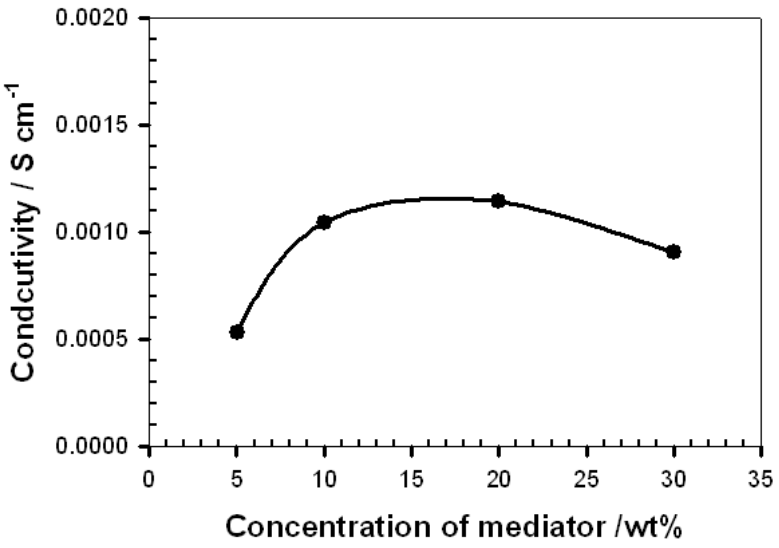

Figure 4.10 Dependence of the conductivity of the electrode on the concentration of the NaI/I_2 mediators at various charge/discharge current densities.

4.6 Conclusions

1. Membranes composed of PVDF and LiTFS in a weight ratio of 1:1 were prepared, and their conductivity was 1.74×10^{-2} S cm^{-1}. This kind of membrane was then used as the separator in a solid-state mediator SC.

2. With the use of water-free PVDF/LiTFS polymer membranes and PEO/$LiClO_4$ polymer electrolytes, the operating voltage window of mediator SCs can reach 2.5 to 3 V, resulting in a significant increase of the specific energy compared with mediator SCs with a Nafion separator, for which the operating voltage window is only 1.0 V.

3. Two types of mediators containing NaI/I_2 and $K_3Fe(CN)_6/K_4Fe(CN)_6$ were added into the PEO/$LiClO_4$ polymer electrolyte to improve the performance of the solid-state SC. Compared to 40.7 F g^{-1}, which is the specific capacitance of a CB SC at a scanning rate of 10 mV s^{-1}, the specific capacitances of the NaI/I_2 and $K_3Fe(CN)_6/K_4Fe(CN)_6$ SCs at a

scanning rate of 10 mV s^{-1} were 209.0 and 138.8 F g^{-1}, respectively. The enhancement of the performance of the mediator SCs with respect to the CB SC is mainly due to an enhancement of the conductivity of the electrolyte in the porous electrodes and the pseudocapacitance provided by the mediators.

CHAPTER 5 A FUNDAMENTAL STUDY OF INTERFACES IN POLYMER ELECTROLYTE FUEL CELL

5.1 Molecular dynamic simulation of Pt/liquid electrolyte and Pt/Nafion interfaces

5.1.1 Simulation methods

A mechanical dynamics (MD) simulation module, FORCITE (Accelrys Inc.), was used to conduct MD simulations. The forcefield used in the simulations was PCFF. PCFF is a consistent family of forcefields. The family were parameterized against a wide range of experimental observables for organic compounds containing H, C, N, O, S, P, halogen atoms and ions, alkali metal cations, and several biochemically important divalent metal cations initially and later were extended so as to have a broad coverage of organic polymers, (inorganic) metals, and zeolites. For MD modeling in the present study, each atomistic model was first geometrically optimized. After the optimization, the dynamics simulation was then carried out for the model. In the dynamic simulation, the duration time was 500 ps, the ensemble was NVE, and the initial temperature was set to be 450 and 500 K. After the 500 ps dynamics simulation, the temperature of the model will be stabilized at different temperatures.

5.1.2 Molecular dynamics models

5.1.2.1 Nafion clusters in catalyst layers vs. free Nafion clusters

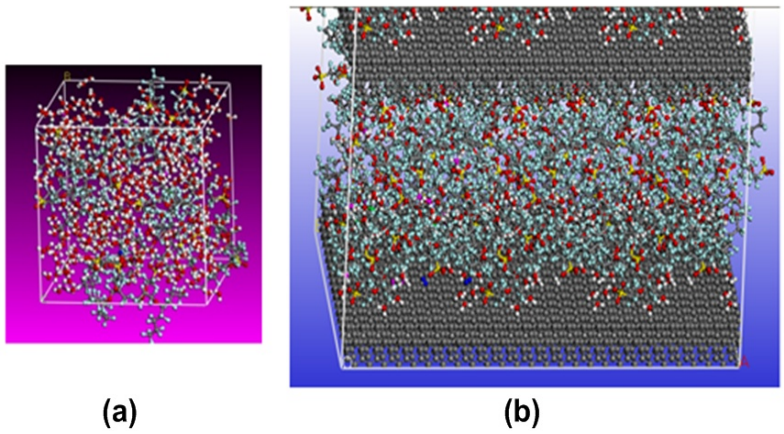

Figure 5.1 MD models for (a) a free Nafion cluster, and (b) a Nafion cluster in the gap between two carbon slabs with a face index of (111).

As shown in Figure 5.1(a), a MD model (unit cells) for simulating free Nafion clusters were constructed. The model consists of H_2O, H_3O^+, H^+, methanol, and Nafion backbone and side chains. Although in reality, the bonds in H_3O^+ can undergo formation or cleavage, the bonds remain intact in the present MD simulations because the simulations purport to evaluate the contribution of the "vehicular diffusion" or physical diffusion versus the structural diffusion. The model was set up with a water content level of 4. It was demonstrated in the previous study that at this water content level, physical diffusion dictates the conduction whereas the contribution of structural diffusion is negligible. In addition, the simulation results of the MD model for a free Nafion cluster are in good agreement with the experimental results on the transport properties in a piece of pure Nafion membrane.

As shown in Figure 5.1(b), a model with a Nafion cluster sandwiched by two carbon slabs with a face index of (1 1 1) and distance of 10 nm are created to mimic the Nafion clusters between carbon supports in catalyst layers. The procedure is to transfer the free Nafion cluster model in Figure 5.1(a) into the two carbon slabs and run an energy minimization calculation session to allow reconciliation between the Nafion cluster and the carbon slabs. The surface atoms of the carbon slabs can be charged to mimic the situations when the catalyst layers are charged during operation. In the current studies the charge density varies from -0.005 to 0.05 e per surface atom. The electroneutrality of the model is maintained by introducing more negatively charged sulfonated groups than positively ions when a positive charge is introduced on the slabs, and by introducing less sulfonated groups than the positive ions when a negative charge is on the slabs. In order to conduct a MD simulation, the initial velocity of every atom in the model was randomly determined according to Boltzmann statistics. The time step was set at 1.0 fs and duration was 500 ps.

The position vector of each particle, $R_i(t)$, is saved as a function of time. The diffusivity of a specific molecule or ion was evaluated using [240,285]:

$$D_a = \frac{1}{6N_a} \lim_{t\to\infty} \frac{d}{dt} \sum_{i=1}^{N_a} \left\langle [R_i(t) - R_i(t)]^2 \right\rangle \tag{5.1}$$

where N_a is the number of diffusing molecules. The sum term on the right side divided by N_a is the mean square displacement (MSD).

The water content in the unit cells in Figure 5.1 is defined as the molar ratio of water to the sulfonated group in Nafion and expressed as an empirical function of relative

humidity according to the experimental data presented in Refs. [286] and [287]. At a relative humidity of 50% the water content is about 3 and in liquid water the corresponding water content is about 22. The density of Nafion, ρ, is a function of water content, λ.

Table 5.1 lists the calculated diffusivities of species in the models shown in Figure 5.1. The last line of Table 5.1 shows data obtained in the case of free Nafion cluster. The diffusivity of hydrogen in Nafion 117 at 300 K, 1 atmosphere, and a relative humidity of ~60% is 6.83×10^{-5} cm^2 s^{-1}. According to the hydrogen crossover data in a Nafion membrane published by Cheng et al. [288] and Henry's constants published by Mann et al. [289], the diffusivity of hydrogen in Nafion should be 9.0×10^{-5} cm^2 s^{-1} under similar conditions. Thus, the present simulation results for the free Nafion cluster are in good agreement with the experimental results. According to Cheng et al., the experimental diffusivity of hydrogen in catalyst layer should be on the order of 10^{-4} cm^2 s^{-1} [288]. The present results for diffusion of hydrogen are generally consistent with the experimental observations. For diffusion of oxygen in Nafion, the data reported by Secanell et al. is 8.45×10^{-6} cm^2 s^{-1} which is also close to the value of 1.09×10^{-5} cm^2 s^{-1} obtained using the MD simulation method [290].

The data in Table 5.1 also indicates that the diffusivity of hydrogen in the Nafion cluster between the carbon slabs is 3-8 times greater than that in the free Nafion cluster. Increase in diffusivity in the Nafion cluster between carbon slabs is a generic phenomenon for other species including O_2, H_3O^+, H_2O, and CH_3OH. This may be explained by the strong interaction between the Nafion cluster and the carbon slabs. It is interesting that the maximum diffusivity appears when the magnitude of charge density is

low or zero. The charges on the carbon slabs attract oppositely charged species (H_3O^+ or sulfonated groups) and polar species (H_2O and CH_3OH). The oppositely charged species exert attractions to similarly charged species. Thus, charging the carbon slabs may impede the movement of these molecules and ions.

Table 5.1 Computational results of diffusivities of species in the Nafion cluster for the model shown in Figure 5.1.

Charge per surface C atom, e	D_{H_2} ($cm^2\ s^{-1}$)	D_{O_2} ($cm^2\ s^{-1}$)	D_{H_3O+} ($cm^2\ s^{-1}$)	D_{H_2O} ($cm^2\ s^{-1}$)	D_{CH_3OH} ($cm^2\ s^{-1}$)
-0.005	2.47×10^{-4}	7.04×10^{-6}	8.95×10^{-6}	2.57×10^{-5}	2.10×10^{-5}
-0.0005	2.92×10^{-4}	3.46×10^{-6}	5.98×10^{-6}	1.68×10^{-5}	1.43×10^{-5}
0.0	2.47×10^{-4}	8.22×10^{-6}	1.26×10^{-5}	2.89×10^{-5}	2.04×10^{-5}
0.00005	5.96×10^{-4}	2.11×10^{-5}	1.16×10^{-5}	3.04×10^{-5}	1.49×10^{-5}
0.01	2.10×10^{-4}	1.67×10^{-5}	4.73×10^{-6}	9.50×10^{-6}	1.16×10^{-5}
0.05	2.53×10^{-4}	1.70×10^{-6}	6.12×10^{-6}	1.04×10^{-5}	1.75×10^{-5}
Free Nafion cluster	6.83×10^{-5}	1.09×10^{-5}	2.60×10^{-6}	6.38×10^{-6}	5.31×10^{-6}

5.1.2.2 Pt(111)/Nafion interface vs. Pt(111)/liquid electrolyte interface

The MD models were created as shown in Figure 5.2. The electrode model is a tetrahedral Pt crystal with four facets of (111) type seating on top of a carbon slab. The four facets were exposed to the electrolyte environment. There are 802 Pt atoms and 4800 C atoms. Three types of clusters were placed in the vacuum space above the configuration to create electrode/electrolyte interfaces: (a) Pt/(H_2O+H_3O^+), (b) Pt/H_2SO_4, and (c) Pt/Nafion. In the Pt/Nafion model, the Nafion cluster contains Nafion backbones, functional groups, H_2O, and H_3O^+.

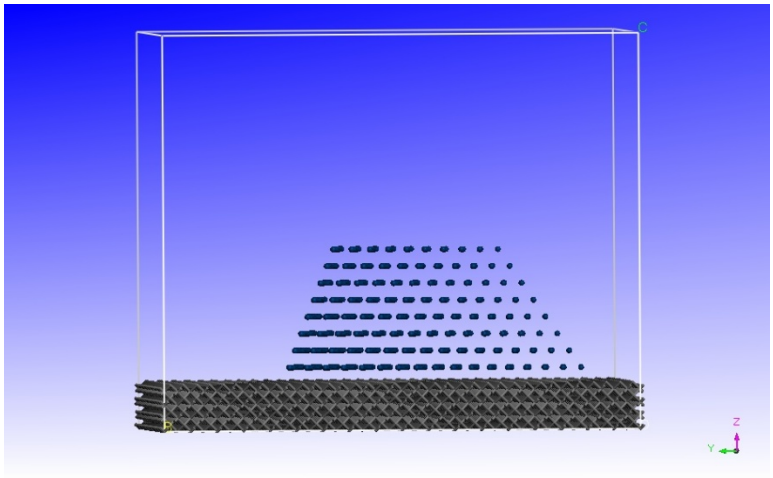

Figure 5.2 A Pt crystal with five (111) faces on top of a carbon slab with a (111) face.

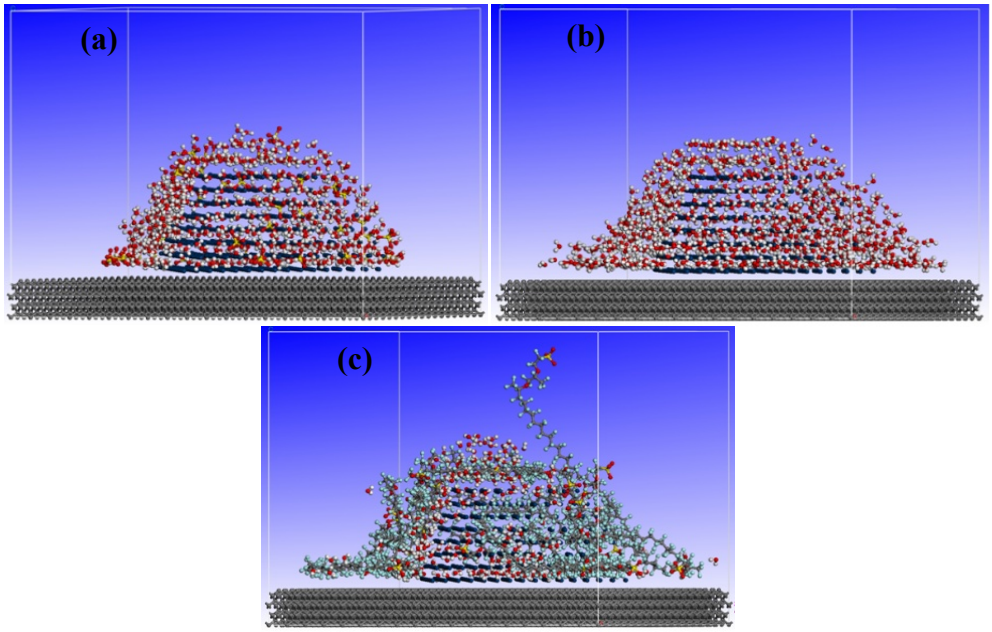

Figure 5.3 The configurations after a first stage of a MD run: (a) Pt/(H_2O+H_3O^+), (b) Pt/H_2SO_4, and (c) Pt/Nafion.

Figure 5.3 show the configurations of the three Pt/electrolyte models after a 500 ps MD dynamics simulation. For the Pt/(H_2O+H_3O^+) and the Pt/H_2SO_4 models, all the

molecules from the electrolyte settle down uniformly near the Pt surface. In the case of Pt/Nafion model, although the Nafion molecules finally settle down on the Pt surface, it is clear that the distribution of the Nafion chains on Pt is not as homogeneous as for the other two models.

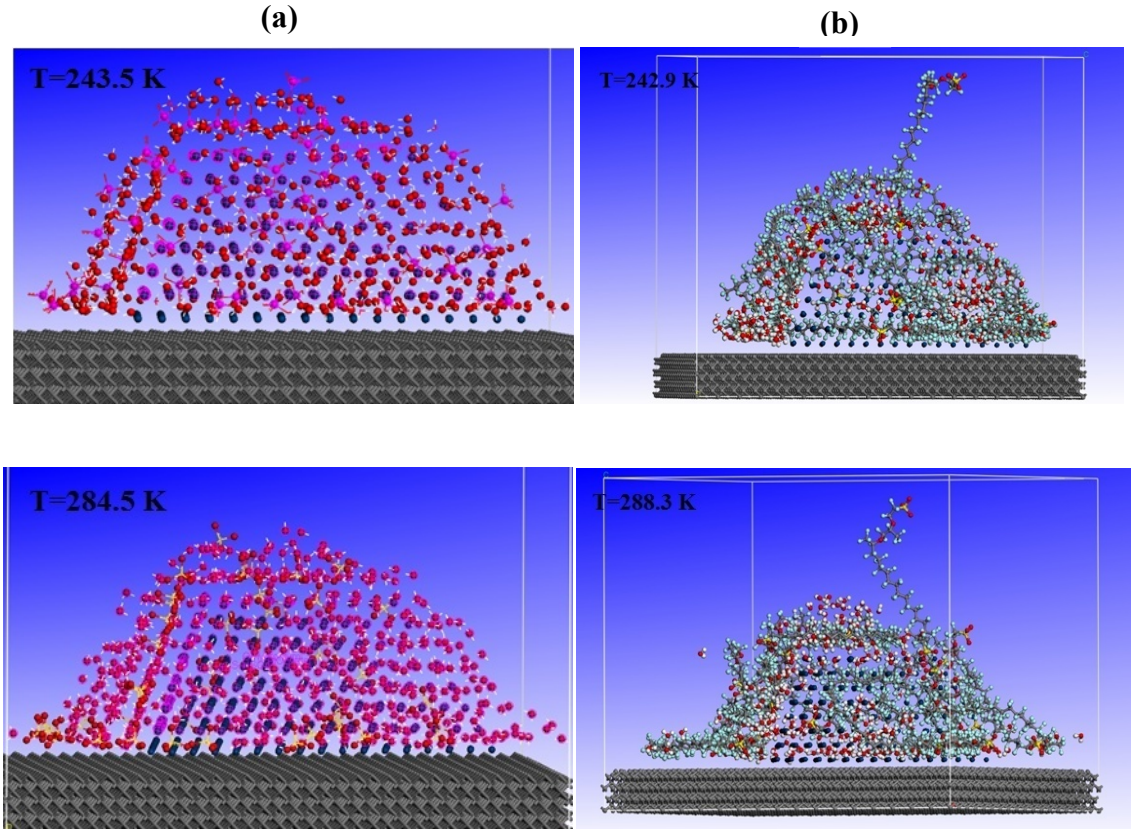

Figure 5.4 Side view of the compact layers formed near the Pt surface after 500 ps MD dynamics simulation for (a) Pt/H_2SO_4 and (b) Pt/Nafion models at different temperatures.

A similar phenomenon for all the three types of Pt/electrolyte systems is that distinct compact layers were formed near the Pt surface. The side views of the compact layers of Pt/H_2SO_4 and Pt/Nafion are given in Figure 5.4, which show that a well-defined compact layer is formed near the Pt surface for all the systems. Specifically, it can be seen from Figure 5.4(a) that for the Pt/H_2SO_4 model, two well-defined compact layers were formed under the temperature of 243.5 and 284.5 K. When the temperature is higher, the second

layer is not as regularly arranged as it is under lower temperature. However, for Pt/Nafion model (shown in Figure 5.4(b)), only one well-defined compact layer is observed.

Table 5.2 Position of the first and second peaks in radial distribution function.

System	Charge type	Temperature (K)	First and second peak (Å)			
			Pt-H_2O	Pt-H_3O^+	Pt-SO_3^-	Pt-F
Pt/Nafion	Neutral	286.5	3.09 4.95	3.01 5.81	3.23	2.75
		302.8	3.07 4.73	3.15 5.05	3.39	2.85
		436.4	3.11 5.01	3.27 4.81	3.29	3.05
	-31 e	307.4	3.01 4.97	2.99 4.85	3.49	2.89
		327.5	3.07 4.97	3.05 5.01	3.51	2.67
		353.6	2.93 4.95	3.13 4.87	3.59	2.83
	+31 e	302.5	3.05 4.87	6.63 7.71	3.37	2.69
		317.5	2.97 5.03	5.33 7.47	3.19	2.81
		343.4	3.11 5.15	3.47 6.07	3.43	2.89
Pt/H_2SO_4	Neutral	313.5	3.00 5.12	3.04 5.15	3.59	
	-31 e	318.8	3.01 5.15	3.05 5.19	3.75	
	+31 e	314.2	2.97 4.93	3.33 4.71	3.67	

In addition to the neutral state, MD simulations were carried out on polarized Pt surface, where -31 e or 31 e were assigned to all the Pt atoms equally. According to Ref. [291], these charges give a potential difference at the interface of about -0.5 and +0.5 V respectively. The results are summarized in Table 5.2. It can be seen that for the Pt/Nafion interface a positive charge on the Pt surface displaces the peaks for the radial distribution between H_3O^+ and Pt far away whereas the effect of polarization on other species is minimum. The effect on H_3O^+ is greater at lower temperature than at higher temperature. In the case of Pt/H_2SO_4 interface, the effect of polarization on all species is minimum. This result is in line with the fact that the reaction rate or exchange current density for oxygen reduction reaction is lower for Pt/Nafion system than that for Pt/H_2SO_4 system. For the Pt/H_2SO_4 system, H_3O^+ are not repelled by the positive charges on the electrode where H_3O^+ in Nafion are not easy to access the electrode surface to participate in the reaction: $O_2 + 4H_3O^+ + 4e^- = 6H_2O$.

5.1.3 Discussion on spatial ordering of water molecules on Pt surface

Figure 5.5 illustrates the positions of the oxygen and sulfur atoms in the first layer on top of Pt crystal for Pt/(H_2O+H_3O^+), Pt/H_2SO_4, and Pt/Nafion models. Figure 5.5(a) clearly shows that the oxygen atoms in water preserve the structure of the (111) face of Pt crystal. Although generally speaking, the water molecules are arranged in a good spatial periodicity or ordering, there are imperfections. Figure 5.5(b) illustrates the first layer of H_2O and H_2SO_4 on top of Pt crystal. It is very interesting that the oxygen atom in HSO_4^- tend to locate the “right” place to maintain the periodicity or special ordering of the first layer on Pt surface. This spatial ordering is destructed in the case of Pt/Nafion interface. As shown in Figure 5.5(c), the unoccupied locations are actually occupied by F atoms.

Thus, the ordering of water molecules is destructed. The areas with adsorbed F atoms block the transport of H_2O and H_3O^+ at the interface.

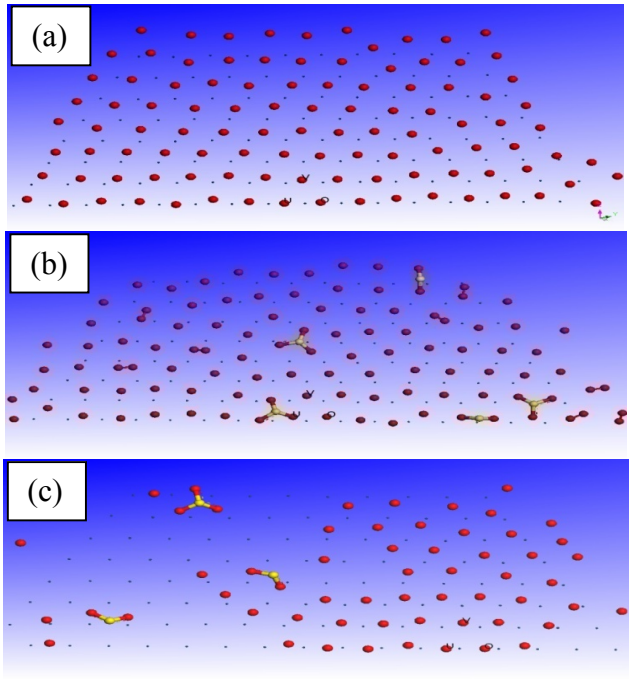

Figure 5.5 Positions of oxygen atoms of H_2O, H_2SO_4, or sulfonated group on top of Pt crystal with a (111) face for (a) Pt/(H_2O+H_3O^+), (b) Pt/H_2SO_4, and (c) Pt/Nafion models. Red: oxygen; blue: Pt atom; yellow: S atom.

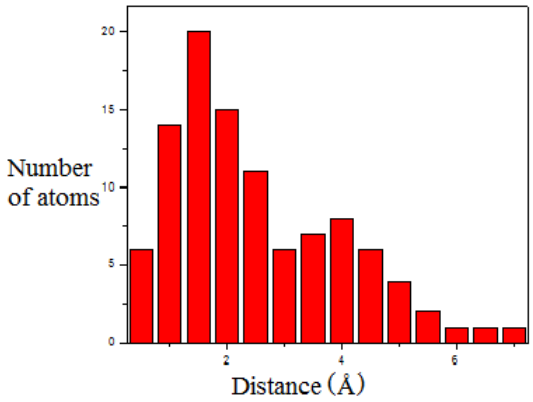

Figure 5.6 Histogram of distance of water molecules from the "right" positions that assume a perfect periodicity.

In order to quantify the ordering of the first layer on Pt surface, information entropy is evaluated using the following equation:

$$S = -\sum_{i=1}^{N} p_i \lg(p_i) = -\sum_{i=1}^{N} \frac{n_i}{N} \lg\left(\frac{n_i}{N}\right) \quad (5.2)$$

where N is the total number of atoms in the system, and n_i is the number of atoms located in each sub-interval in the histogram of the distance of water molecules from the "right" positions that assume a perfect periodicity (Figure 5.6). The results are listed Table 5.3. It is clear that the first layer in the case of Nafion has the highest entropy whereas that for pure water has the least.

Table 5.3 Information entropy for the first layer on the surface of the crystal.

System	Temperature (K)	Entropy
Pt/Nafion	288.3	1.000
	313.2	1.210
Pt/H_2SO_4	284.5	0.912
	303.5	0.902
Pt/H_2O	257.5	0.876
	295.9	0.947

5.2 *Ab initio* models: Pt/Nafion interface vs. Pt/H_2SO_4 interface

5.2.1 Observation of association and dissociation of proton in H_2SO_4 and Nafion

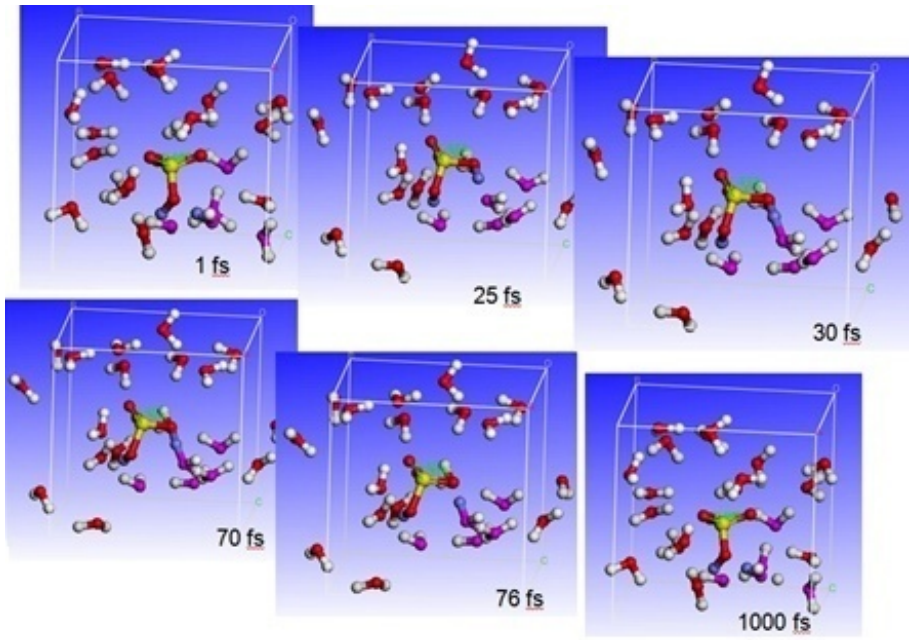

Figure 5.7 Cartoons showing dissociation and association of proton in H_2SO_4.

Figure 5.7 shows a set of snapshots an *ab initio* simulation conducted at room temperature. Two protons in a H_2SO_4 molecule are blue colored. It can be seen that at 30 fs, one proton form a bond with a water molecule. At 76 fs, the proton disbands with the H_2SO_4 molecule. The charge of this proton is transported a distance of a few molecules away in 1,000 fs. However, another proton is very stable in the HSO_4^- anion. This is in agreement with the common understanding that it is easy for H_2SO_4 to form one H_3O^+ and one HSO_4^- anion but difficult to form two H_3O^+ and one SO_4^{2-} anion.

Figure 5.8 includes four snapshots of the Nafion cluster during a geometrical optimization, showing the dissociation of sulfonated group (-SO_3H) and the transport of proton. The original hydrogen atom in -SO_3H is highlighted in light purple. In step 1, it

can be seen that a covalent bond is established between this hydrogen atom and an oxygen atom from a nearby water molecule. In step 5, the bond O-H bond in the sulfonated group is broken, resulting in a H_3O^+ and a $-SO_3^-$. These two steps denote the dissociation of sulfonated group. In step 10, another hydrogen atom in the H_3O^+ (shown in dark purple) formed a covalent bond with a second water molecule. The original H-O covalent bond breaks in step 12. As a result, a transportation process is fulfilled in these following two steps.

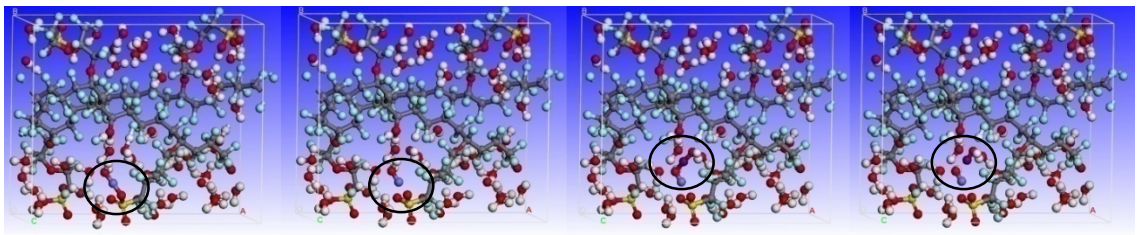

Figure 5.8 Cartoons showing dissociation and transportation of proton in Nafion.

5.2.2 Establishment of the interface models

According to the results of the MD simulation, the structure of the electrolyte at the interface is highly ordered and periodic. Thus, the *ab initio* molecular dynamics (AIMD) study was uniformly conducted using periodic boundary conditions. Typical *ab initio* models are shown in Figure 5.9. These are two unit cells with a Pt slab and clusters of H_2SO_4 and Nafion electrolyte on the top of the Pt slab. For these two unit cell, there are terraced Pt atoms on the surface of the Pt slab. These locations with terraced Pt atoms are considered as active sites on Pt catalysts. However, in the present study, unit cells with a smooth Pt surface were also created.

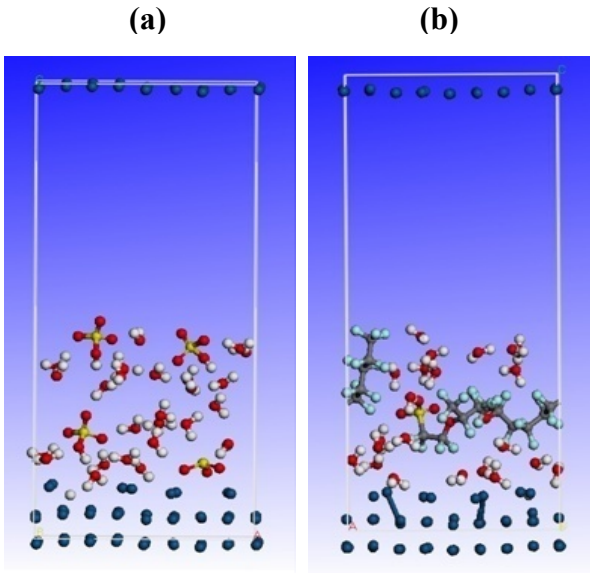

Figure 5.9 *Ab* initio models of terraced Pt surface with (a) H_2O, H_3O^+, and HSO_4^-, and (b) Nafion clusters.

5.2.3 *Ab initio* molecular dynamics simulation results

The charge on the Pt slab and energy of the system as functions of time are shown in Figures 5.10-5.13. Both charge and energy fluctuate with time and they correlate with one another. According to Balbuena et al., the fluctuation of the charge can be used to evaluate the electron exchange current density [292]. However, in the present work, I prefer not to adopt this approach. The reason is that the size of the models is too small and the time duration is too short which are limited by the capability of existing computers in most present and previous *ab initio* simulations. Although I have established a workstation with 100 CPUs, completion of an *ab initio* computation for the models with duration of 1,000 fs would require one month. In fact, the main idea of this work is to combine MD, AIMD, and quantum statistical methods to evaluate the exchange current density at the interfaces but not to rely only on AIMD to reveal the

charge transfer processes. Rather, the major goal of the *ab initio* simulation is to provide the amplitude and period of charge and energy fluctuations. These parameters will then be used for the quantum statistical computations. Two interesting findings from the AIMD simulations are as follows. First, although the Pt is not charged initially, the total charges of the Pt slabs are all positive. This means the interfaces are spontaneously polarized with electrons passing across the interface from Pt slabs to the electrolytes. This can be considered as a proof of the assumption that any interface between dissimilar materials should be polarized in certain extent and form a double layer. Second, the relative amplitude of energy fluctuation is greater for smooth surface than that for terraced surface. The peak of the energy fluctuation can be considered as the energy barrier for the system to transit from one to another charged state [293], or activation energy. The results show that for the smooth surface the activation energy is greater than that for the terrace surface or the terraced surface is more active than the smooth surface. This is in line with the commonly accepted understanding that terraced Pt surface is more active [294].

Figure 5.14 illustrates the potential distributions at the interfaces. At the interface between H_2SO_4 and positively charged Pt slab, the electrical field is positive in the contact layer and negative in the electrolyte beyond the contact layer. This is in line with commonly accepted theory regarding the electric double layer in liquid electrolyte. The minimum potential is marked as the inner Helmholtz face. However, for the Pt/Nafion interface, the distribution is not uniform. There are several maxima and minima. However, the general trend for the Pt/Nafion interface is similar to that for the Pt/H_2SO_4 interface.

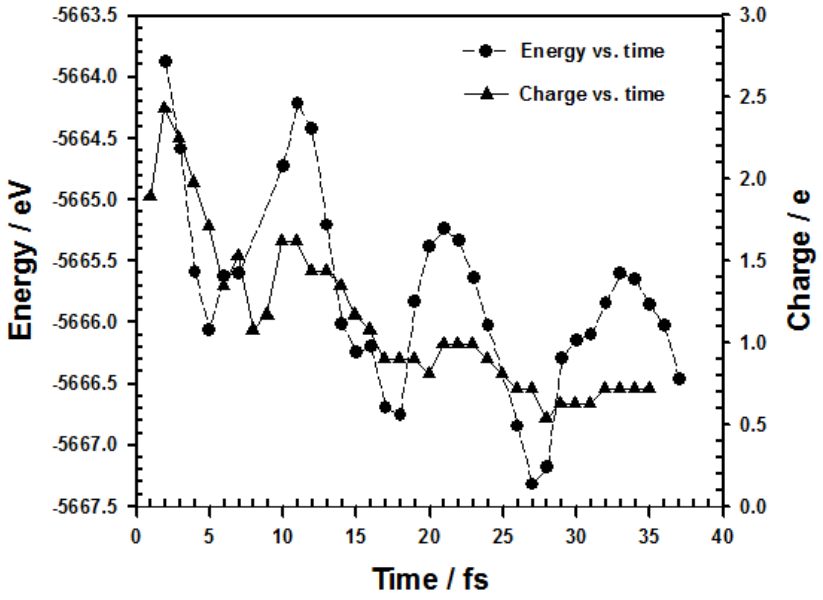

Figure 5.10 The charge on a smooth Pt slab interfacing with water molecules and H_3O^+ ions and the total energy of the system as functions of time.

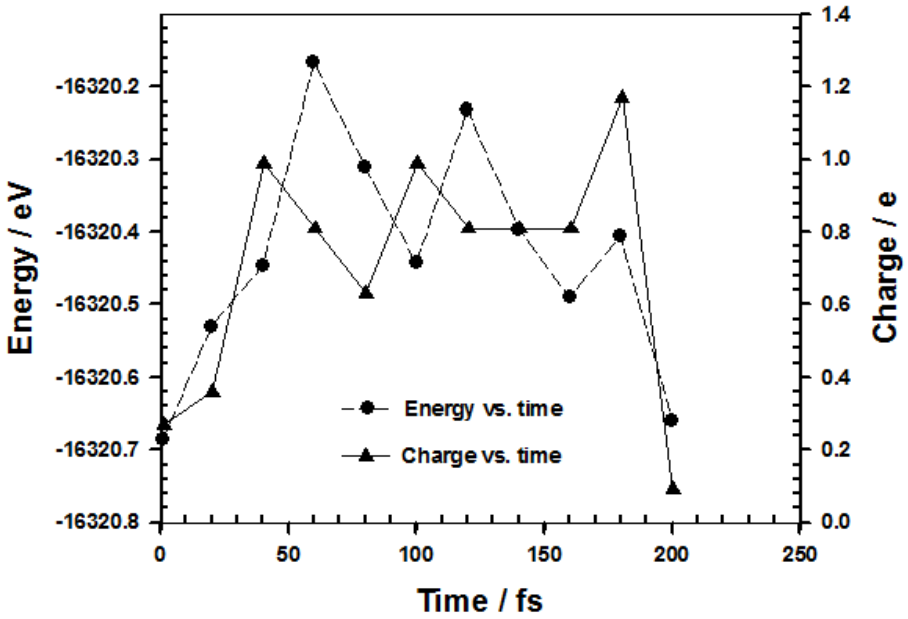

Figure 5.11 The charge on a terraced Pt slab interfacing with water molecules and H_3O^+ ions and the total energy of the system as functions of time.

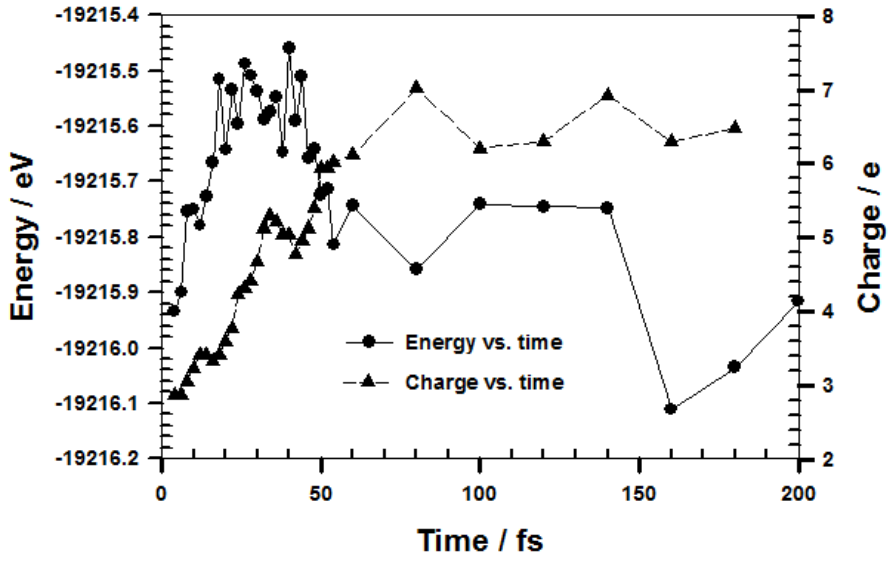

Figure 5.12 The charge on a terraced Pt slab interfacing with H_2SO_4 solution the total energy of the system as functions of time.

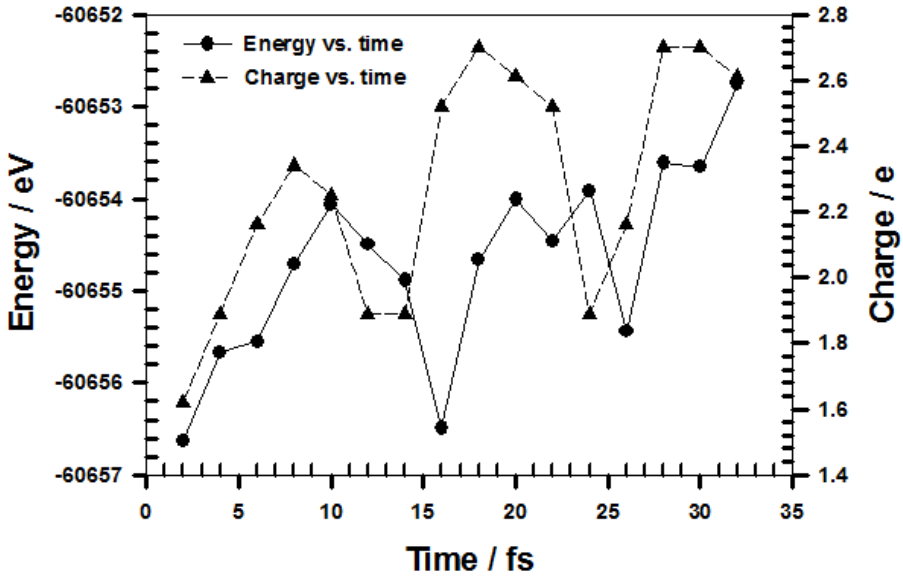

Figure 5.13 The charge on a terraced Pt slab interfacing with a Nafion cluster and the total energy of the system as functions of time.

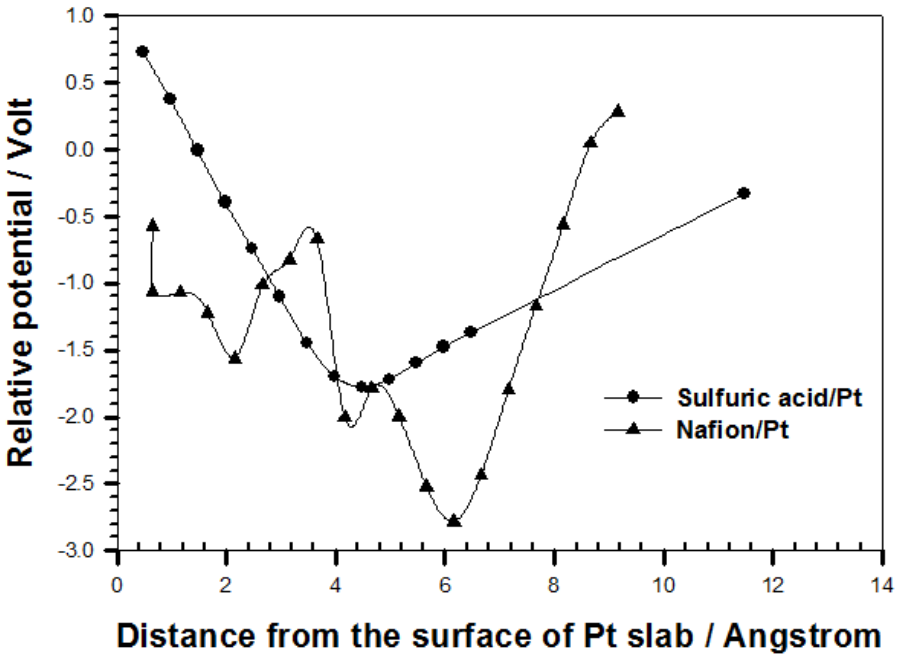

Figure 5.14 Potential distribution at Pt/electrolyte interfaces.

5.3 Quantum statistical computation

5.3.1 Computational approach

The general description of the quantum statistical method for evaluating the electrochemical exchange current density, $\boldsymbol{j}$, given by the following formula [295]:

$$\boldsymbol{j} = \sum_{\Omega}[\boldsymbol{C}]\left(\frac{\boldsymbol{W_{eff}}}{\boldsymbol{2\pi}}\right)\boldsymbol{exp}\,(\boldsymbol{\sigma_t})\int_{\boldsymbol{Z_{min}}}^{\infty}\boldsymbol{k_e(z,\Omega)exp}\,\left(-\frac{\boldsymbol{\Delta E_a(z,\Omega)}}{\boldsymbol{kT}}\right)\boldsymbol{dz} \qquad (5.3)$$

where Ω is angular degree of freedom; z refers to the reagent-metal surface distance; $[C]$ is the bulk reagent concentration; σ_t is the electron tunneling factor; $\Delta E_a\ (z,\ \Omega)$ is the activation energy; k is the Boltzmann constant and T is the temperature in the experiment; W_{eff} is the effective frequency of classic vibration modes of reacting cluster; and k_e is electron transfer coefficient.

W_{eff} can be estimated by,

$$\mathrm{W_{eff}} = \frac{\mathrm{nkT}}{\mathrm{h}} * 2\pi \tag{5.4}$$

$\boldsymbol{k_e}$ can be evaluated by,

$$\boldsymbol{k_e} = \mathbf{1} - \boldsymbol{exp}\left(\frac{\frac{\Delta E_e}{2}}{\boldsymbol{hW_{eff}}} * \boldsymbol{r}\right) \tag{5.5}$$

where the resonance splitting of the potential energy surface $\Delta \boldsymbol{E_e}$ can be evaluated via a perturbation the approach,

$$\frac{\Delta \boldsymbol{E_e(z,\Omega)}}{\mathbf{2}} = \int \boldsymbol{\Psi_i}(\boldsymbol{U_{coul}} + \boldsymbol{U_{edl}})\boldsymbol{e}\boldsymbol{\Psi_f}\, \boldsymbol{dv} \tag{5.6}$$

In the formula, $\boldsymbol{\Psi_i}$ and $\boldsymbol{\Psi_f}$ are wavefunctions in the vibration of reacting molecules that can be evaluated using an *ab initio* method; $\boldsymbol{U_{coul}}$ and $\boldsymbol{U_{edl}}$ are columbic potential of the reactant and EDL potential in the interface area, respectively; $\boldsymbol{e}$ is unit charge of electron;

The parameter $\boldsymbol{r}$ takes the following form,

$$\boldsymbol{r} = \left(\frac{\boldsymbol{\pi}}{\boldsymbol{(E_{in} + E_s)kT}}\right)^{\frac{\mathbf{1}}{\mathbf{2}}} \tag{5.7}$$

where $\boldsymbol{E_{in}} + \boldsymbol{E_s}$ is sum of the inner- and outer-sphere contributions.

The strategy for the quantum statistical computation using Equations 5.3-5.7 procedure is as follows. First, the MD simulation results will be used to determine the general structure of the interface. The electron tunneling factor, activation energy, and wavefunctions are evaluated using the *ab initio* method. The *ab initio* molecular dynamics simulations yield a temporal series of molecular configurations including

activation energies, vibration energy, charges, and wavefunctions at each step. By applying the famous Ergodic hypothesis for a canonical ensemble, all of the configurations generated in the MD and AIMD simulations can be treated as possible configurations exist at a time in a large system. Thus, an average over all these configurations gives the quantity for a realistic system. Table 5.4 shows constants from Equations 5.3 to 5.7 for computing the electrochemical exchange current density. Third, following simplification has been made. In computing the electron tunneling factor and the resonance splitting of the potential energy surface $\Delta \boldsymbol{E_e}$, only the highest occupied molecular orbitals (HOMOs) are considered. It is believed that the contribution of the lower orbtals is orders of magnitude less than that of the HOMOs. Thus, for Pt we only consider 6s and 6p orbitals.

Table 5.4 Constants assumed value in our calculations.

Parameter	Unit	Values with unit
K	J K^{-1}	1.38×10^{-23}
T	K	300
$[C]$	mol L^{-1}	0.1
E	C	1.6×10^{-19}
$U_{coul} + U_{edl}$	V	1

5.3.2 Results

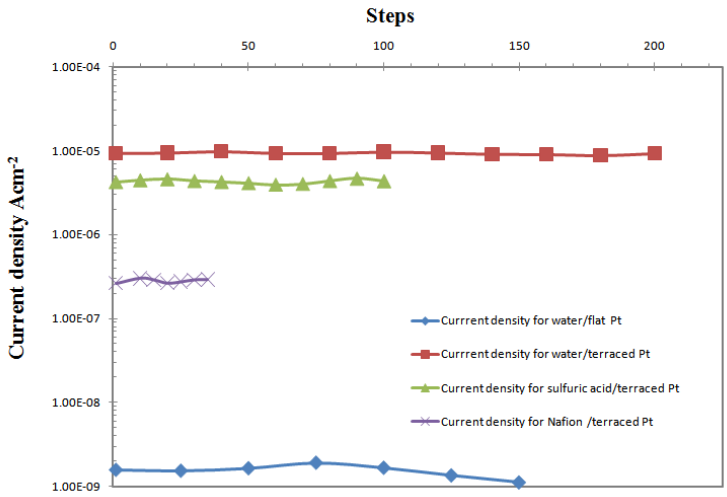

Figure 5.15 Current density vs. steps for four types of interfaces.

Figure 5.15 shows the total current density as function of simulation step or configurations in the trajectory of simulation for four different cases. They are: 1) flat Pt/(H_2O+H_3O^+) interface; 2) terraced Pt/(H_2O+H_3O^+) interface; 3) terraced Pt/H_2SO_4 interface; and 4) terraced Pt/Nafion interface. It is clear that the interface with a terraced Pt has much greater current density than the interface with a flat Pt surface. The current densities for protonated water and H_2SO_4 solution are much greater than that for Nafion.

5.4 STM study of the Pt/Nafion and Carbon/Nafion interfaces

5.4.1 Experimental approach

Two types of substrates were used. The first type was polycrystalline Pt sheets. The second type was highly oriented pyrolytic graphite (HOPG) plates. Both types of samples were acquired from Alfa Aesar. Before coating with Nafion film, the Pt sheets were cleaned up using sulfuric acid and rinsed with distilled water and acetone. The Pt sheet

was then dried with pure N_2 to remove the residues. The surfaces of HOPG samples were prepared by peeling off the surface layer using a piece of adhesive tape. This exposed a clean and fresh HOPG surface.

Diluted Nafion solution (5 wt%, Sigma Aldrich) was dropped on the surfaces of Pt sheets or fresh HOPG samples. The weights of the coated Pt sheets were weighed before applying Nafion solution and after Nafion film was dry. The increment of the weight was 0.1 mg. Since the density of dry Nafion ionomer was about 2.0 g cm^{-3} [287] and the area of the Pt sheet was 1.0 cm^2, the thickness of the film was 500 nm. As shown in Figure 5.16, on top of the Nafion film a Ag|AgCl and Ag strip were painted using silver adhesive blended with AgCl powder and silver adhesive respectively and they were used as reference and counter electrodes respectively. In addition, a U-shape Ag strip was painted and used for discharge purpose. Release of the charge that may accumulate in the Nafion film proved to be important for obtaining the high resolution and stable images of the coated samples. The arrangements of the electrodes for all HOPG and Pt samples were similar. Two Ag strips and the sample substrate were connected with a potentiostat to apply potential. The sample substrate was also connected in a circuitry to apply a bias voltage between the STM tip and the substrate. The potential and bias voltage were applied independently.

In order to confirm the thickness of the film, the Nafion film was peel off from a HOPG sample and the sample was examined with SEM. The micrographs of a coated HOPG sample are shown in Figure 5.17. The left micrograph (1) shows that the film uniformly covered the substrate. It is clear that part of the Nafion film was torn away

from the HOPG substrate. The right micrograph (2) shows under a greater magnification that the thickness of the film was a few hundred nanometers.

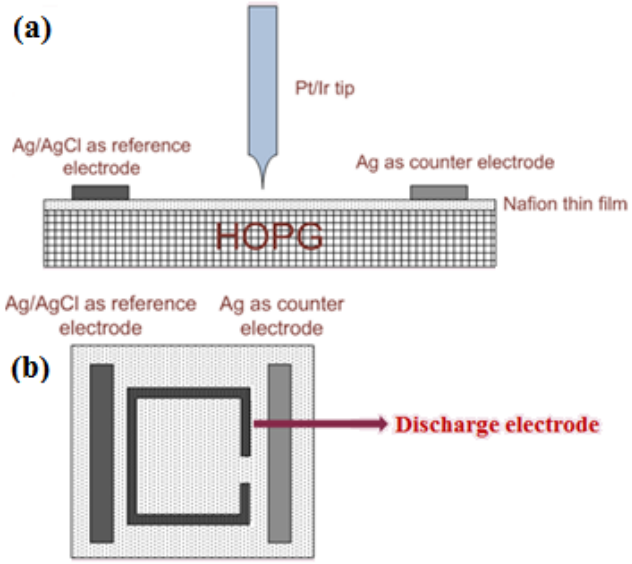

Figure 5.16 Schematic of the experimental setup for EC STM imaging of a Nafion coated substrate: (a) cross section view; (b) top view.

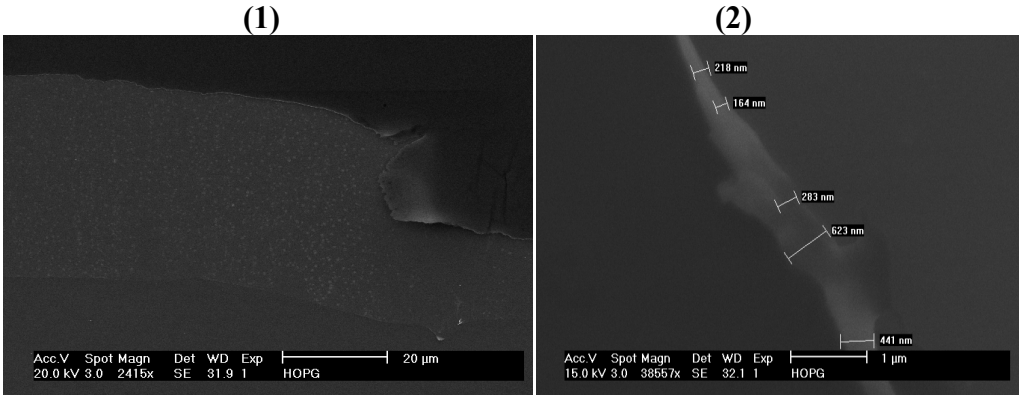

Figure 5.17 SEM micrographs of Nafion-coated HOPG sample: (1) lower magnification and (2) higher magnification. The Nafion film was peeled off but part of the film remained on the HOPG substrate.

5.4.2 Results

The images shown in Figure 5.18 were obtained from Pt sheets. The left was from a blank Pt sheet and the right was from a Nafion coated Pt sheet. Both images are very similar. The average size of the crystals on the Nafion-coated Pt sample was much greater than that on the blank Pt sample. Figure 5.19 shows images of a blank and Nafion coated HOPG. It is clear that the spacing between neighboring atoms or periodicity of the arrays was about 2.50 Å in good agreement with the theoretical value of 2.461 Å for HOPG. For the Nafion-coated HOPG sample, the image shows a similar symmetry but a much greater periodicity (~20 Å). Figure 5.20 shows three most commonly recorded structures. They are triangular shapes, diamond shapes, and hexagonal net.

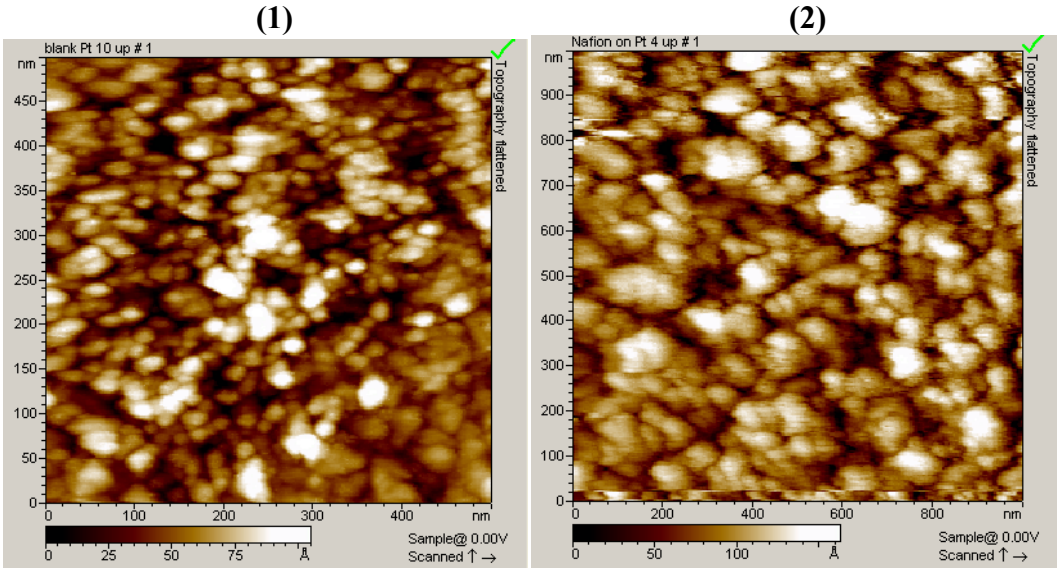

Figure 5.18 STM topographic images of Pt sheet samples: (1) A blank Pt sheet and (2) A Pt sheet coated with Nafion film (Potential: -0.40 V, bias: -0.2 V).

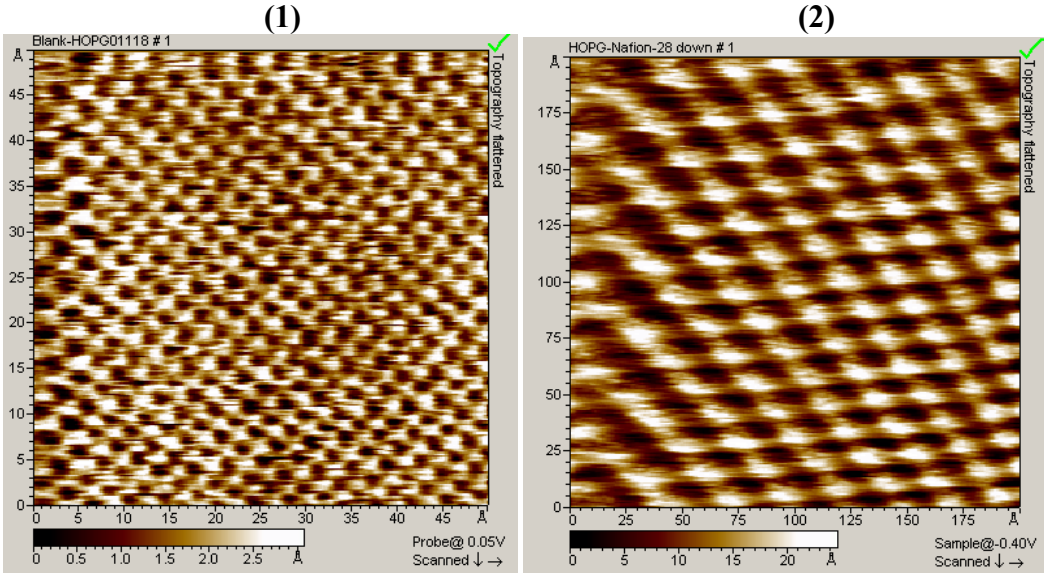

Figure 5.19 STM topographic images of HOPG samples: (1) A blank HOPG sheet and (2) A HOPG sheet coated with Nafion film. (Potential: 0.0 V, bias: -0.4 V)

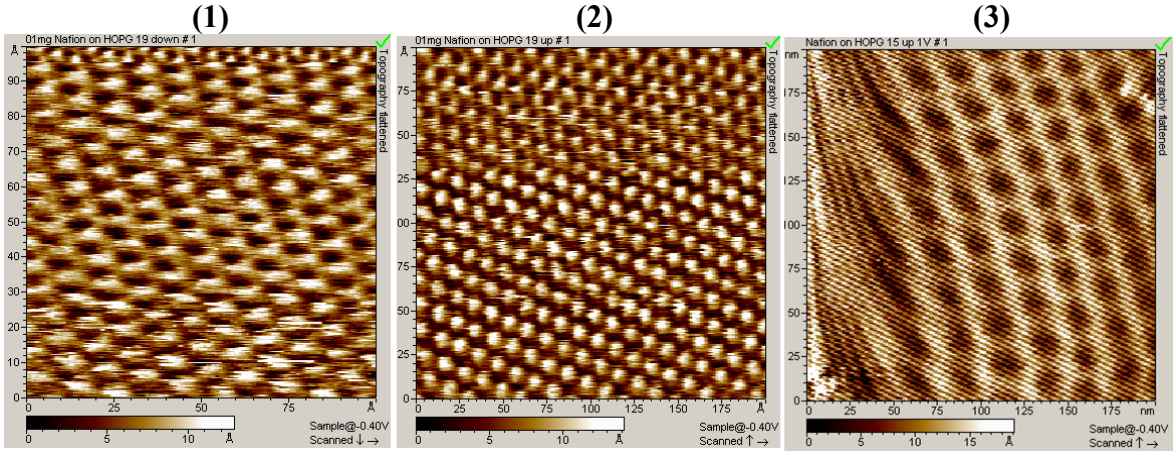

Figure 5.20 Three most commonly recorded structures: (1) triangular; (2) diamond; and (3) hexagonal or honeycomb.

Figure 5.21 shows periodic structures in one area of a Nafion-coated HOPG sample with different magnifications. The scanned area for the upper left image was 2000 nm × 2000 nm. At the bottom part of this image, there were some blur features close to the

cracks, which were believed to be the cracks on the HOPG when it was cleaned with an adhesive tape before coated with Nafion. These features became clear when the scan area was set farther from the cracks as shown in the upper center image. When the magnification was doubled in the upper right image, the size of the triangular features was about 160 nm and periodicity was about 200 nm similar to those in the upper center image. When the magnification was further doubled in the bottom left image, the size and periodicity remained the similar. The magnification for the bottom center image was 40 folds of that for the upper center image. The triangular features disappeared. However, arrays of atom-like features appeared. The horizontal and vertical periodicities were about 40 and 20 Å respectively. All these observations demonstrate that the periodic features observed on the Nafion-coated HOPG samples were not fake images but reflected a real structure at the HOPG/Nafion interface.

Figure 5.22 shows the responses of the images to change of the applied potential. The initial applied potential was 1.0 V. When the applied potential was switched from 1.0 to -1.0 V, the periodic arrays (deformed hexagonal net) temporarily disappeared and then a different type of periodic arrays (triangular shapes) appeared. When the applied potential was switched back to 1 V, the periodic arrays of triangular shapes disappeared and at the bottom hexagonal net reappeared. At 0 V, the arrays were equilateral triangles. When the potential was switched to -0.45 V, these triangles disappeared. At the bottom part of the bottom right image, a net type of features appeared.

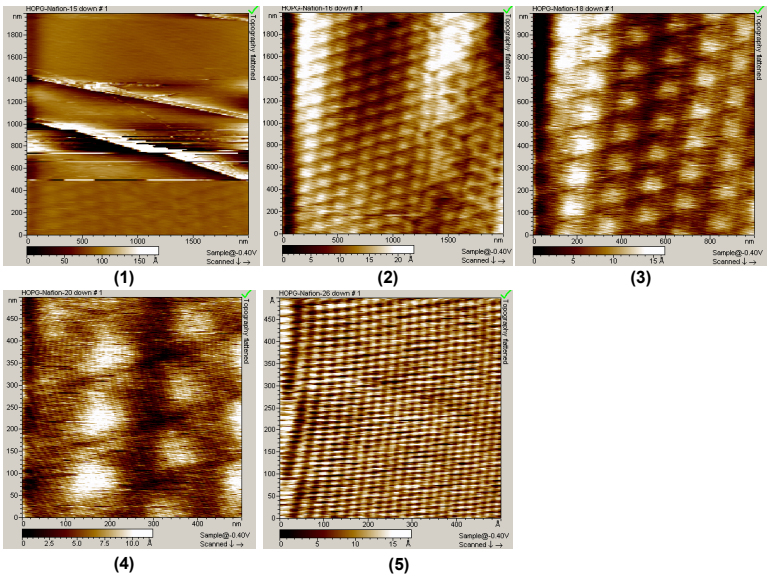

Figure 5.21 STM images obtained from one location of a Nafion coated HOPG sample with different magnifications: (1) 2000×2000 nm; (2) 2000×2000 nm, (3) 1000×1000 nm, (4) 500×500 nm, (5) 500× 500 Å.

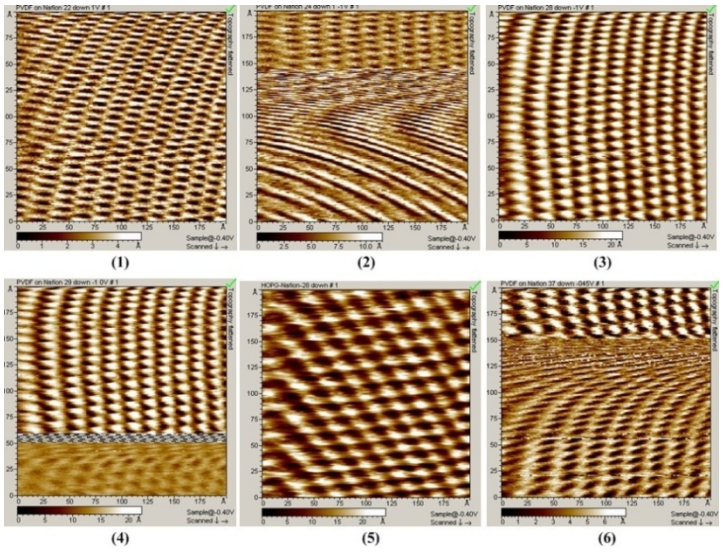

Figure 5.22 STM image respond to change of the applied potential: (1) at 1.0 V; (2) switching from 1.0 to -1.0 V; (3) -1.0 V; (4) switching from -1.0 to 1.0 V; (5) 0 V; (6) switching from 0 to -0.45 V

5.4.3 Discussion

Wang et al. studied dry-prepared and di-chloroethane-treated HOPG samples [296]. They found essentially, there were two types of patterns: the triangular and honeycomb structures that can be simultaneously observed at grain boundaries. A general layer-sliding model was utilized to explain the experimental results: sliding of the HOPG topmost layer was used to explain the origins of the triangular and honeycomb structures, and molecule intercalation into inter-layer spacing between the first and second layers of HOPG induced inhomogeneous deformation of the HOPG topmost layer that accordingly generated the Moiré patterns of the HOPG sample in di-chloroethane."

Sun et al. studied supperlattice formed on blank HOPG samples [297]. Their conclusion was "Based on the above simulations, the STM data could be well understood in the terms of the rotational moiré pattern hypothesis. The shifts in different directions are formed by either intralayer twisting or gliding. These kinds of motions of the carbon atoms in a graphite layer make the boundary region highly strained."

According to the conclusions the previous studies on essentially blank HOPG samples, the STM images may reveal different types of patterns including the triangular, hexagonal (honeycomb),and superlattice structures. However, with existing theories, it is still difficult to explain why both Nafion-coated Pt and HOPG samples show enlarged structures. The rate of enlargement was between 5-20 times.

Probably the first difficult question that is required to provide an explanation with respect to the present experimental results is: how can electron tunneling occur in a Nafion film with a thickness of at least 100 nm? According to existing theoretical analysis, in air or vacuum, the tunneling distance is in the range of a few angstroms. Tang

et al. investigated thin PTFE film of a few nanometers on HOPG, and they observed some blur periodic patterns [298]. Based on their observations, they proposed the electrical field is so strong at the STM tip that the dielectric film was broken down and a current passed through the break-down path. However, we did examine the film after many days of experiment on the used samples. No sign of break-down was found. In addition, in the present case, the thickness of the film was much greater than what they examined.

Lindsay et al. proposed that the pressure applied by the tip and resonance between some atoms or molecules and the tip might permit electron tunneling in a thick polymer film on top of a HOPG sample [299]. This theory required that the tip actually pressing into the polymer. We think this is an impossible assumption because we found that a single touch if the tip would make it impossible to obtain an image with an atomic resolution.

Yuan et al. [300] and Carrara et al. [43] presented independently another mechanism that STM can image a non-conducting film via current flow in water film on the outer surface of the the non-conducting film or water clusters in a non-conducting film. In this case, the STM functions in a similar way to a scanning electrochemical microscopy (SECM). However, it is well known that with SECM the imaging resolution is in micrometer level.

Similar to other polymers, the bulk of Nafion consists of both amorphous and crystalline domains [301]. The amorphous domains are water containing and ionic conducting phases while crystalline domains are hydrophobic and non-conducting phases. It was estimated that degree of crystallinity was 8-12 wt%. Ludvigsson et al. studied

recast Nafion film on a single crystal silicon using FTIR and XRD methods [302]. The XRD revealed a wide amorphous peak right after the film was formed but a very sharp peak at a spacing of 2.72 Å after it was stored in ambient conditions for a week, indicating a partial crystallization. Wood et al. studied the structure of Nafion film on Pt and glassy carbon using neutron reflectometry, they found that the interfacial and even the bulk structures were affected by the substrate structure [303]. Kendrick et al. studied Pt/Nafion interface using IR and atomistic simulation (DFT) methods [304]. They concluded that the side chain and CF_2 groups anchored to Pt and form an integrated part of the Pt/Nafion interface and that the -CF_2 groups were ordered were the interface.

With the assumption that the Nafion is partially ordered, a possible explanation for this phenomenon would be the resonant tunneling between the tip and the electronic conductor through such a thick Nafion film. In order to illustrate this possibility, a series of 2-D multi-barrier models are introduced as shown in Figure 5.23 for mimicking the electronic structure of Nafion. Because recast Nafion film is not a crystalline structure but can be viewed as a structure between periodic and completely random structures, we propose these following parameters. The first height of the barrier is 10.25 eV resembling the gap between the tip and Nafion film. Usually the workfunction is about 5 eV for a metal. Thus the top of the conduction band in the tip is at the 5eV level in Figure 5.23. Inside Nafion, there are hundreds of barriers with random heights, widths, and distances between neighboring barriers. However, the average height is 5.25 eV. The average width and distance are 2 Å. The last barrier has a height of 7 eV.

The transmission coefficient can be evaluated by solving the time-independent Schrodinger Equation (Appendix). For a model with 250 barriers and a total width of

100 nm, the transmission coefficient versus energy of free electrons is illustrated in Figure 5.24(a). A result with completely periodic 2-D structure with the 2nd to 249th height being 5.25 eV and the width and distance being 2 Å is also shown in Figure 5.24(b) for comparison. For both periodic and non-periodic potential barriers, there is one band of 249 energy states between 2 and 3.2 eV below the internal barrier height of 5.25 eV with significant transmission coefficients. However, for free electrons with kinetic energy of 5.25 eV, the transmission coefficient is negligible. Similar analyses and observations can be found in Ref. [305-306] in which the authors evaluated the transmission coefficient of free electrons through a multibarrier semiconductor heterojunctions. However, in these analyses the semiconductor heterojunctions are completely periodic structures.

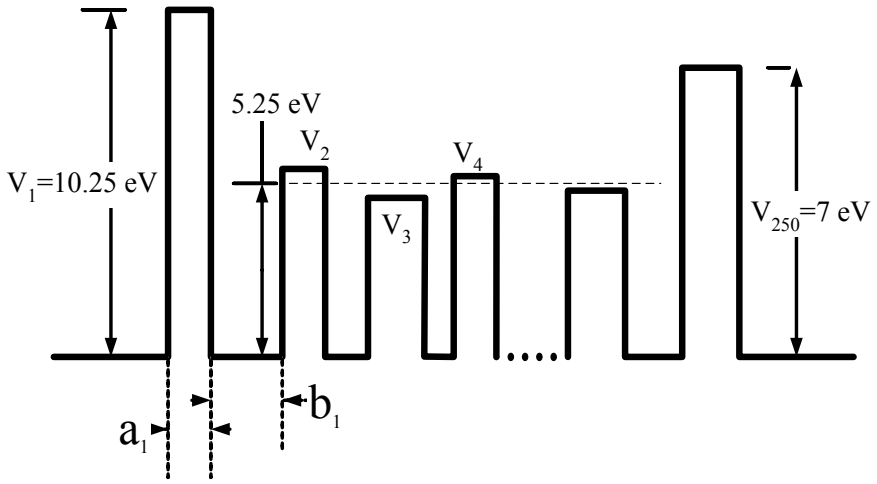

Figure 5.23 A 2-D potential barrier model emulating a junction of STM tip/air/Nafion film/HOPG or Pt. There are total 250 barriers. The heights of the potential barriers are random numbers between 5.0 and 5.5 eV. The widths of the barriers and distances between the barriers are also random numbers.

However, with existing theories, it is still difficult to explain why both Nafion-coated Pt and HOPG samples show enlarged structures under STM. In fact, we tried to use a Nafion 112 membrane with a thickness of 1,000 nm to cover the surface of an HOPG. The tip could not be engaged with the sample. We also tried to coat the surface with a PVDF film. The tip was able to engage and the STM images could be obtained but the image was unclear and unstable.

Halbritter analyzed resonant tunneling phenomenon at the interface between metal and oxide [307-308]. He concluded the hybridization of the conduction state and the localized state enhanced electron tunneling. Probably, the hybridization at the interface between Pt or HOPG and covalently (strongly) bonded Nafion forms a structure that maintains the symmetry but has a large scale. More research will be conducted to reveal the mechanism for the phenomenon.

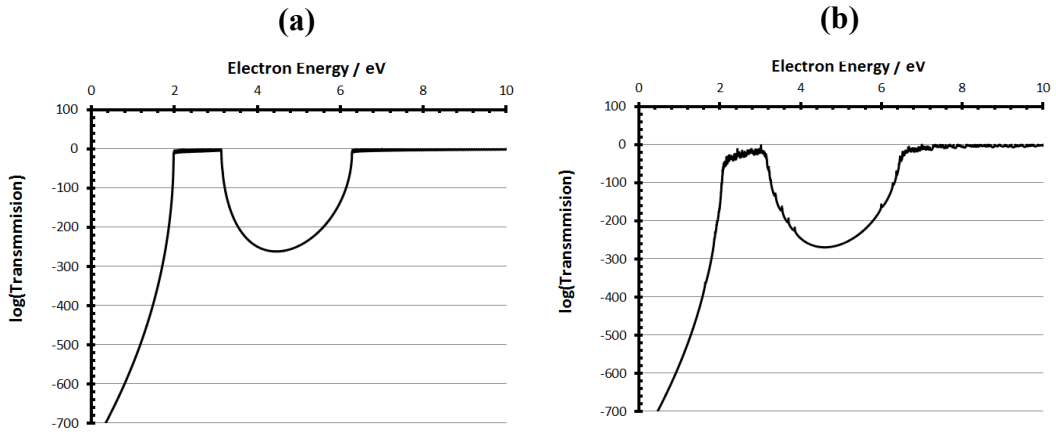

Figure 5.24 Transmission coefficient of electron tunneling versus electron kinetic energy: (a) The thickness and spacing between the energy barriers are 2 Å; (b) The thickness and spacing between the energy barriers are random number with an average of 2 Å.

5.5 Conclusions

The following conclusions can be made based on the theoretical and experimental results:

1) Polarization has very significant effect on H_3O^+ at Pt/Nafion interface but minimum effect on protons at Pt/H_2SO_4 interface. Negative charges have minimum effect for both interfaces.

2) *Ab initio* simulation can spontaneously generate polarized interfaces or EDLs and dissociation/association of protons from electrolytes.

3) Fluctuations of energy correlate with charge transfer across the interface, from which the energy barriers for charge transfer can be estimated.

4) Quantum statistical calculations correctly predict the trends of the electrochemical current density.

5) Images with atomistic resolutions for Nafion-coated Pt and HOPG samples can be obtained with a STM. The images can be recognized as a reflection of the morphology and structure at the interfaces between Nafion film and electron conducting substrates. The interface structures are highly ordered structures in line with the atomistic simulation results.

6) It is possible that electrons tunnel in a 100 nm Nafion thin film via a resonant tunneling between the STM tip and molecules in the contact layer at the interface.

Appendix

Time independent Schrodinger equation:

In the regions between potential barriers, $-\frac{\hbar^2}{2m}\frac{d^2\psi}{dx^2} = E\psi$

Inside the energy barriers, $-\frac{\hbar^2}{2m}\frac{d^2\psi}{dx^2} = (E-V)\psi$

The solution of the Schrodinger equation is

x<0, $\psi_0 = e^{ikx} + B_0 e^{-ikx}$

0<x<a, $\psi_1 = A_1 e^{\kappa_1 x} + B_1 e^{-\kappa_1 x}$

a<x<a+b, $\psi_2 = A_2 e^{ikx} + B_2 e^{-ikx}$

a+b<x<2a+b, $\psi_3 = A_3 e^{\kappa_3 x} + B_3 e^{-\kappa_3 x}$

……..

x>250a+250b, $\psi_{500} = A_{500} e^{ikx}$

The boundary conditions are as follows:

At the left sides of the barriers:

$$A_{2n}e^{ikSigma(2n)} + B_{2n}e^{-ikSigma(2n)} = A_{2n+1}e^{\kappa_{2n+1}Sigma(2n)} + B_{2n+1}e^{-\kappa_{2n+1}Sigma(2n)}$$

$$ikA_{2n}e^{ikSigam(2n)} - ikB_{2n}e^{-ikSigma(2n)} = \kappa_{2n+1}A_{2n+1}e^{i\kappa_{2n+1}Sigma(2n)} - \kappa_{2n+1}B_{2n+1}e^{-\kappa_{2n+1}Sigma(2n)}$$

At the right side of the barriers:

$$A_{2n}e^{ikSigma(2n-1)} + B_{2n}e^{-ikSigma(2n-1)} = A_{2n-1}e^{\kappa_{2n+1}Sigma(2n-1)} + B_{2n-1}e^{-\kappa_{2n+1}Sigma(2n-1)}$$

$$ikA_{2n}e^{ikSigma(2n-1)} - ikB_{2n}e^{-ikSigma(2n-1)} = \kappa_{2n-1}A_{2n-1}e^{i\kappa_{2n-1}Sigam(2n-1)} - \kappa_{2n-1}B_{2n-1}e^{-\kappa_{2n-1}Sigam(2n-1)}$$

In the equations

$$k^2 = \frac{2mE}{\hbar^2}$$

$$\kappa_i^2 = \frac{2m(V_i - E)}{\hbar^2}$$

$$Sigma(2n) = \sum_{i=1}^{n} (a_i + b_i)$$

$$Sigma(2n-1) = (\sum_{i=1}^{n} (a_i + b_i)) - b_n$$

Where m is the mass of electron and $\hbar$ is Planck's constant.

REFERENCE

[1]. Y. M. Vol'fkovich, T. M. Serdyuk, Electrochemical Capacitors, Russ. J. Electrochem., 38 (2002) 935-958.

[2]. A. Lewandowski, M. Galinski, Practical and theoretical limits for electrochemical double-layer capacitors, J. Power Sources, 173 (2007) 822-828.

[3]. W. Li, J. Chen, J. Zhao, J. Zhang, J. Zhu, Application of ultrasonic irradiation in preparing conducting polymer as active materials for supercapacitor, Mater. Lett., 59 (2005) 800-803.

[4]. G.A. Snook, P. Kao, A.S. Best, Conducting-polymer-based supercapacitor devices and electrodes, J. Power Sources, 196 (2011) 1-12.

[5]. M. Galinski, A. Lewandowski, I. Stepniak, Ionic liquid as electrolytes, Electrchimi. Acta, 51 (2006) 5567-5580.

[6]. X.M. Liu, X.G. Zhang, NiO-based composite electrode with RuO_2 for electrochemical capacitors, Electrochim. Acta, 49 (2004) 229-232.

[7]. R. Kötz, M. Carlen, Principles and applications of electrochemical capacitors, Electrochim. Acta, 45 (2000) 2483-2498.

[8]. P. Thounthong, V. Chunkag, P. Sethakul, S. Sikkabut, S. Pierfederici, B. Davat, Energy management of fuel cell/solar cell/supercapacitor hybrid power source, J. Power Sources, 196 (2011) 313-324.

[9]. Z. Lan, J. Wu, J. Lin, M. Huang, P. Li, Q. Li, Influence of ionic additives NaI/I_2 on the properties of polymer gel electrolyte and performance of quasi-solid-state dye-sensitized solar cells, Electrochim. Acta, 53 (2008) 2296-2301.

[10]. S. Dong, B. Wang, B. Liu, Amperometric glucose sensor with ferrocene as an electron transfer mediator, Biosens. Bioelectron., 7 (1992) 215-222.

[11]. EG&G Technical Services, Inc., Fuel Cell Handbook, U.S. Department of Energy, Office of Fossil Energy, National Energy Technology Laboratory, 2004.

[12]. P. Costamagna, S. Srinivasan, Quantum jumps in the PEMFC science and technology from the 1960s to the year 2000, J. Power Sources, 102 (2001) 242-252.

[13]. P. Jannasch, Recent developments in high-temperature proton conducting polymer electrolyte membranes, Curr. Opin. Colloid Interface Sci., 8 (2003) 96-102.

[14]. E. Chalkova, X. Zhou, C. Ambler, M.A. Hofmann, J.A. Weston, H.R. Allcock, S.N. Lvov, Sulfonimide polyphosphazene-based H_2/O_2 fuel cells, Electrochem. Solid-State Lett. 10 (2002) 221-223.

[15]. Basic needs for the hydrogen economy, DOE BES Workshop Report, Argonne Nationa Laboratory & U.S. DOE-BES, May 13-15, 2003.

[16]. P. Spinelli, C. Francia, E.P. Ambrosio, M. Lucariello, Semi-empirical evaluation of PEMFC electro-catalytic activity, J. Power Sources, 178 (2008) 517-524.

[17]. M.D. Maci, J.M. Campi, E. Herrero, J.M. Feliu, On the kinetics of oxygen reduction on platinum stepped surfaces in acidic media, J. Electroanal. Chem. 564 (2004) 141-150.

[18]. L. Zhang, C. Ma, S. Mukerjee, Oxygen reduction and transport characteristics at a platinum and alternative proton conducting membrane interface, J. Electroanal. Chem. 568 (2004) 273-291.

[19]. J. O'M. Bockris, S. Srinivasan, Fuel Cells: Their Electrochemistry, McGraw-Hill Book Company, New York, 1969.

[20]. R.J. Hunter, Zeta Potential in Colloid Science: Principles and Applications, Academic Press, New York, 1981.

[21]. A. W. Adamson, Physical Chemistry of Surfaces, Willey-Interscience Publication, New York, 1982.

[22]. B.E. Conway, Electrochemical Supercapacitors, Kluwer Academic/Plenum Publisher, New York, 1999.

[23]. A. Zunger, A. Franceschetti, G. Bester, W. B. Jones, K. Kim, P. A. Graf, L-W. Wang, A. Canning, O. Marques, C. Voemel, J. Dongarra, J. Langou, S. Tomov, Predicting the electronic properties of 3D million atom semiconductor nanostructures, J. Phys. B: Conference Series, 46 (2006) 292-298.

[24]. S. E. Thompson, S. Parthasarathy, Moore's law: the future of Si microelectronics, Mater. Today, 9 (2006) 20-25.

[25]. W. Goddard III, B. Merinov, A. V. Duin, T. Jacob, M. Blanco, V. Molinero, S.S. Jang, Y. H. Jang, Multi-paradigm multi-scale simulations for fuel cell catalysts and membranes, Mol. Simul., 32 (2006) 251-268.

[26]. K.A. Mauritz, R.B. Moore, State of understanding of Nafion, Chem. Rev., 104 (2004) 4535-4585.

[27]. S. Ma, Q. Chen, F.H. Jøgensen, P.C. Stein, E.M. Skou, ^{19}F NMR studies of Nafion™ ionomer adsorption on PEMFC catalysts and supporting carbons, Solid State Ionics, 178 (2007) 1568-1575.

[28]. P.B. Balbuena, E.J. Lamas, Y. Wang, Molecular modeling studies of polymer electrolytes for power sources, Electrochim. Acta, 50 (2005) 3788-3795.

[29]. M.J. Janik, M. Neurock, First principles analysis of the electro-oxidation of CO over Pt (1 1 1), Electrochim. Acta, 52 (2007) 5517-5528.

[30]. C.D. Taylor, S.A. Wasileski, J.-S. Filhol, M. Neurock, First principles reaction modeling of the electrochemical interface: Consideration and calculation of a tunable surface potential from atomic and electronic structure, Phys. Rev. B 73 (2006) 165402 1-16.

[31]. A.B. Anderson, N.M. Neshev, R.A. Sidik, P. Shiller, Mechanism for the electrooxidation of water to OH and O bonded to platinum: quantum chemical theory. Electrochimi. Acta, 47 (2002) 2999-3008.

[32]. A.B. Anderson , Y. Cai, R.A. Sidik, D.B. Kang, Advancements in the local reaction center electron transfer theory and the transition state structure in the first step of oxygen reduction over platinum, J. Electroanal. Chem., 580 (2005) 17-22.

[33]. F. Jiao, P.G. Bruce, Mesoporous crystalline β-MnO_2 - a reversible positive electrode for rechargeable lithium batteries, Adv. Mater., 19 (2007) 657-660.

[34]. W. Schmickler, New models for the structure of the electrochemical interface, Prog. Surf. Sci., 22(4) (1986) 323-420.

[35]. D.L. Wood, J. Chlistunoff, J. Majewski, R.L. Borup, Nafion structural phenomena at platinum and carbon interfaces, J. Am. Chem. Soc., 131 (2009) 18096-18104.

[36]. M.J. Cheah, I.G. Kevrekidis, J. Benziger, Effect of interfacial water transport resistance on coupled proton and water transport across Nafion, J. Phys. Chem. B, 115 (2011) 10239-10250.

[37]. A.S. AricoÁ, P. CretõÁ, P.L. Antonucci, J. Cho, H. Kimc, V. Antonucci, Optimization of operating parameters of a direct methanol fuel cell and physio-chemical investigation of catalyst-electrolyte interface, Electrochim. Acta, 43 (1988) 3719-3729.

[38]. U.A. Paulus, A. Wokaun, G.G. Scherer, P. Scherrer, T.J. Schmidt, V. Stamenkovic, V. Radmilovic, N.M. Markovic, P.N. Ross, Oxygen reduction on carbon-supported Pt-Ni and Pt-Co alloy catalysts, J. Phys. Chem., B 106 (2002) 4181-4191.

[39]. R. Wiesendanger, Scanning probe microscopy and spectroscopy-methods and applications, Cambridge University Press, Cambridge, 1994.

[40]. S.L. Tang, A.J. McGie, A. Suna, Molecular-resolution imaging of insulating macromolecules with the scanning tunneling microscope via anon-tunneling, electric-field-induced mechanism, Phys. Rev. B, 47 (7) (1993) 3850-3856.

[41]. S.M. Lindsay, O.F. Sankey, Y. Li, C. Herbst, Pressure and resonance effect in scanning tunneling microscopy of molecular adsorbates, J. Phys. Chem., 94 (1990) 4655-4660.

[42]. J.-Y. Yuan, Z. Shao, C. Gao, Alternative method of imaging surface topologies of nonconducting bulk specimen by scanning tunneling microscopy, Phys. Rev. Lett., 67(7) (1991) 863-866.

[43]. S. Carrara, V. Eroklin, C. Nicolini, STM image formation of organic thin films: The role of water shell, Langmuir, 16 (2000) 6577-6582.

[44]. B.E. Conway, W.G. Pell, Double-layer and pseudocapacitance types of electrochemical capacitors and their applications to the development of hybrid devices. J. Solid State Electrochem. 7 (2003) 637-644.

[45]. X. Anderieu, L. Josset, Proceedings of the symposium on electrochemical capacitors, Electrochem. Soc., Pennington PV 95-29 (1997) 181-186.

[46]. J.-B. Donnet, R. C. Bansal, M.-J. Wang, Carbon black: science and technology, 2nd edition, Marcel Dekker, New York, 1993.

[47]. A.J. Bard, M.V. Mirkin, D.O. Wipf, in: A.J. Bard (Ed.), Electroanalytical Chemistry, vol. 18, Marcel Dekker, New York, NY, 1994, pp. 243.

[48]. H.-H. Kim, J.-H. Kim, Y.-H. Lee. K.-B. kim, Synthesis and characterization of electrochemically prepared ruthenium oxide on carbon nanotube film substrate for supercapacitor applications, J. Electrochem. Soc., 152 (2005) A2170-A2178.

[49]. R. Amade, E. Jover, B. Caglar, T. Mutlu, E. Bertran, Optimization of MnO_2/vertically aligned carbon nanotube composite for supercapacitor application, J. Power Sources, 196 (2011) 5779-2783.

[50]. S.-J. Kim, G.-J. Park, B.C. Kim, J.-K. Chung, G.G. Wallace, S.-Y. Park, Investigations into the electrochemical characteristics of nickel oxide hydroxide/multi-walled carbon nanotube nanocomposites for use as supercapacitor electrodes, Synth. Met., 161 (2012) 2641-2646.

[51]. B. Dong, B.-L. He, C.-L. Xu, H.-L. Li, Preparation and electrochemical characterization of polyaniline/multi-walled carbon nanotubes somposites for supercapacitor, Mater. Sci. Eng. B, 143 (2007) 7-13.

[52]. M. Yao, B. Cheng, H. Song, X. Chen, Preparation and electrochemical performance of polyaniline-based carbon nanotubes as electrode material for supercapacitor, Electrochim, Acta, 55 (2010) 7021-7027.

[53]. B. Cornell, D. Simonsson, Ruthenium dioxide as cathode material for hydrogen evolution in hydroxide and chlorate solutions, J. Electrochem. Soc., 140 (1993) 3123-3129.

[54]. J.H. Jang, S. Han, T. Hyeon, S.M. Oh, Electrochemical capacitor performance of hydrous ruthenium oxide/mesoporous carbon composite electrodes, J. Power Sources, 123 (2003) 79-85.

[55]. C.-C. Hu, W.-C. Chen, Effects of substrates on the capacitive performance of $RuOx \bullet nH_2O$ and activated carbon- RuOx electrodes for supercapacitors, Electrochim. Acta, 49 (2004) 3469-3477.

[56]. C.-C. Hu, K.-H. Chang, Cyclic voltammetric deposition of hydrous ruthenium oxide for electrochemical supercapacitors: effects of the chloride precursor transformation, J. Power Sources, 112 (2002) 401-409.

[57]. C.-C. Hu, M.-J. Liu, K.-H. Chang, Anodic deposition of hydrous ruthenium oxide for supercapacitors, J. Power Sources 163 (2007) 1126-1131.

[58]. J. Li, Q.M. Yang, I. Zhitomirsky, Nickel foam-based manganese dioxide-carbon nanotube composite electrodes for electrochemical supercapacitors, J. Power Sources, 185 (2008) 1569-1574.

[59]. I.-H. Kim, J.-H. Kim, K.-B. Kim, Electrochemical characterization of electrochemically prepared ruthenium oxide/carbon nanotube electrode for supercapacitor application, Electrochem. Solid-State Lett., 8 (2005) A369-372.

[60]. C.-C. Hu, M.-J. Liu, K.-H. Chang, Anodic deposition of hydrous ruthenium oxide for supercapacitors: Effects of the AcO^- concentration, plating temperature, and oxide loading, Electrochim. Acta, 53 (2008) 2679-2687.

[61]. I.-H. Kim, J.-H. Kim, Y.-H. Lee, K.-B. Kim, Synthesis and characterization of electrochemically prepared ruthenium oxide on carbon nanotube film substrate for supercapacitor applications, J. Electrochem. Soc., 152 (2005) A2170-A2178.

[62]. C.-C. Hu, K.-H. Chang, Cyclic voltammetric deposition of hydrous ruthenium oxide for electrochemical supercapacitors: effects of the chloride precursor transformation, J. Power Sources, 112 (2002) 401-409.

[63]. C.-C. Hu, K.-H. Chang, Cyclic voltammetric deposition of hydrous ruthenium oxide for electrochemical capacitors: effects of codepositing iridium oxide, Electrochim. Acta, 45 (2000) 2685-2696.

[64]. J.H. Park, O.O. Park, Morphology and electrochemical behaviour of ruthenium oxide thin film deposited on carbon paper, J. Power Sources, 109 (2002) 121-126.

[65]. V.D. Patake, C.D. Lokhande, Oh Shim Joo, Electrodeposited ruthenium oxide thin films for supercapacitor: Effect of surface treatments, Appl. Surf. Sci., 255 (2009) 4192-4196.

[66]. Y. Xie, D. Fu, Supercapacitance of ruthenium oxide deposited on titania and titanium substrates, Mater. Chem. Phys., 122 (2010) 23-29.

[67]. S.K. Mandal, N. Munichandraiah, Anodic deposition of porous RuO_2 on stainless steel for supercapacitor studies at high current densities, J. Power Sources, 175 (2008) 657-663.

[68]. V.D. Patake, S.M. Pawar, V.R. Shinde, T.P. Gujar, C.D. Lokhande, The growth mechanism and supercapacitor study of anodically deposited amorphous ruthenium oxide films, Curr. Appl. Phys., 10 (2010) 99-103.

[69]. C.-C. Hu, C.-C. Wang, K.-H. Chang, A comparison study of the capacitive behavior for sol-gel-derived and co-annealed ruthenium-tin oxide composites Electrochim. Acta, 52 (2007) 2691-2700.

[70]. J.P. Zheng, P.J. Cygan, T.R. Jow, Hydrous ruthenium oxide as an electrode material for electrochemical capacitors, J. Electrochem. Soc., 142 (1995) 2699-2703.

[71]. P. Staiti, F. Lufrano, Investigation of polymer electrolyte hybrid supercapacitor based on manganese oxide-carbon electrodes, Electrochim. Acta, 55 (2010) 7436-7442.

[72]. B. Messaoudi, S. Joiret, M. Keddam, H. Takenouti, Anodic behaviour of manganese in alkaline medium, Electrochim. Acta, 46 (2001) 2487-2498.

[73]. L.L. Zhang, T. Wei, W. Wang, X.S. Zhao, Manganese oxide-carbon composite as supercapacitor electrode materials, Microporous Mesoporous Mater., 123 (2009) 260-267.

[74]. C. Yu, L. Zhang, J. Shi, J.G.J. Zhao, D. Yan, A simple template-free strategy to synthesize nanoporous manganese and nickel oxides with narrow pore size distribution, and their electrochemical properties, Adv. Funct. Mater., 18 (2008) 1544-1554.

[75]. X. Wang, A. Yuan, Supercapacitive behaviors and their temperature dependence of sol-gel synthesized nanostructured manganese dioxide in lithium hydroxide electrolyte, J. Power Sources, 172 (2007) 1007-1011.

[76]. J.N. Broughton, M.J. Brett, Investigation of thin sputtered Mn films for electrochemical capacitors, Electrochim. Acta, 49 (25) (2004) 4439-4446.

[77]. M. Nakamura, M. Nakanishi, K. Yamamoto, Influence of physical properties of activated carbons on characteristics of electric double-layer capacitors, J. Power Sources, 60 (1996) 225-231.

[78]. S.-L. Kuo, N.-L. Wu, Investigation of pseudocapacitive charge-storage reaction of $MnO_2 \cdot nH_2O$ supercapacitors in aqueous electrolytes, J. Electrochem. Soc., 153 (2006) A1317-A1324.

[79]. C.-C. Hu, C.-C. Wang, Nanostructures and capacitive characteristics of hydrous manganese oxide prepared by electrochemical deposition, J. Electrochem. Soc., 150 (2003) A1079-A1084.

[80]. S. Devaraj, N. Munichandraiah, High capacitance of electrodeposited MnO_2 by the effect of a surface-active agent, Electrochem. Solid-State Lett., 8 (2005) A373-A377.

[81]. E.-H. Liu, X.-Y. Meng, R. Ding, J.-C. Zhou, S.-T. Tan, Potentiodynamical co-deposited manganese oxide/carbon composite for high capacitance electrochemical capacitors, Mater. Lett., 61 (2007) 3486-3489.

[82]. C.-C. Hu, T.-W. Tsou, Ideal capacitive behavior of hydrous manganese oxide prepared by anodic deposition, Electrochem. Commun., 4 (2002) 105-109.

[83]. M. Min, K. Machida, J.H. Jang, K. Naoi, Hydrous RuO_2/carbon black nanocomposites with 3D porous structure by novel incipient wetness method for supercapacitors J. Electrochem. Soc., 153 (2006) A334-A338.

[84]. D. Yang, Pulsed laser deposition of manganese oxide thin films for supercapacitor applications, J. Power Sources, 196 (2011) 8843-8849.

[85]. J. Xu, L. Gao, J. Cao, W. Wang, Z. Chen, Preparation and electrochemical capacitance of cobalt oxide (Co_3O_4) nanotubes as supercapacitor material, Electrochimi. Acta, 56 (2010) 732-736.

[86]. S.G. Kandalkar, J.L. Gunjakar, C.D. Lokhande, Preparation of cobalt oxide thin films and its use in supercapacitor application, Appl. Surf. Sci., 254 (2008) 5540-5544.

[87]. Y.F. Yuan, X.H. Xia, J.B. Wu, X.H. Huang, Y.B. Pei, J.L. Yang, S.Y. Guo, Hierarchically porous Co_3O_4 film with mesoporous walls prepared via liquid crystalline template for supercapacitor application, Electrochem. Commun., 13 (2011) 1123-1126.

[88]. H. Kim, T. Seong, J. Lim, W. Cho, Electrochemical and structural properties of radio frequency sputtered cobalt oxide electrodes for thin-film supercapacitors, J. Power Sources, 102 (2001) 167-171.

[89]. Y. Shan, L. Gao Mater, Formation and characterization of multi-walled carbon nanotubes/Co_3O_4 nanocomposites for supercapacitors, Chem. Phys., 103 (2007) 206-210.

[90]. C.-G. Liu, Y.-S. Lee, Y.-J. Kim, I.-C. Song, J.-H. Kim, Electrochemical characteristics of hydrothermally deposited nickel hydroxide on multi-walled carbon nanotube for supercapacitor electrode, Synth. Met., 159 (2009) 2009-2012.

[91]. Y.-Z. Zheng, H.-Y. Ding, M.-L. Zhang, Preparation and electrochemical properties of nickel oxide as a supercapacitor electrode material, Mater. Res. Bull., 44 (2009) 403-407.

[92]. A.I. Inamdara, Y.S. Kima, S.M. Pawarb, J.H. Kimb, H. Ima, H. Kim, Chemically grown, porous, nickel oxide thin-film for electrochemical supercapacitors, J. Power Sources, 196 (2011) 2393-2397.

[93]. M. Wu, L. Zhang, D. Wang, C. Xiao, S. Zhang, Cathodic deposition and characterization of tin oxide coatings on graphite for electrochemical supercapacitors, J. Power Sources, 175 (2008) 669-674.

[94]. S.-L. Kuo, N.-L. Wu, Composite supercapacitor containing tin oxide and electroplated ruthenium oxide, Electrochem. Solid-State Lett., 6 (2003) A85-A87.

[95]. R.S. Mane, J. Chang, D. Ham, B.N. Pawar, T. Ganesh, B.W. Cho, J.K. Lee, S.-H. Han, Dye-sensitized solar cell and electrochemical supercapacitor applications of electrochemically deposited hydrophilic and nanocrystalline tin oxide film electrodes, Curr. Appl. Phys., 9 (2008) 87-91.

[96]. K.R. Prasad, K. Koga, N. Miura, Electrochemical deposition of nanostructured indium oxide: high-performance electrode material for redox supercapacitors, Chem. Mater., 16 (2004) 1845-1847.

[97]. J. Chang, W. Lee, R.S. Mane, B.W. Cho, S.-H. Han, Morphology-dependent electrochemical supercapacitor properties of indium oxide, Electrochem. Solid-State Lett., 11 (2008) A9-A11.

[98]. T.P. Gujar, V.R. Shinde, C.D. Lokhande, S.-H. Han, Electrosynthesis of Bi_2O_3 thin films and their use in electrochemical supercapacitors, J. Power Sources, 161 (2006) 1479-1485.

[99]. C.D. Lokhande, T.P. Gujar, V.R. Shinde, Rajaram S. Mane, S.-H. Han, Electrochemical supercapacitor application of pervoskite thin films, Electrochem. Commun., 9 (2007) 1805-1809.

[100]. T. Kudo, Y. Ikeda, T. Watanabe, M. Hibino, M. Miyayama, H. Abe, K. Kajita, Amorphous V_2O_5/carbon composites as electrochemical supercapacitor electrodes, Solid State Ionics, 152-153 (2002) 833-841.

[101]. X. Zhou, H. Chen, D. Shu, C. He, J. Nan, Study on the electrochemical behavior of vanadium nitride as a promising supercapacitor material, J. Phys. Chem. Solids, 70 (2009) 495-500.

[102]. P.M. Kulal, D.P. Dubal, C.D. Lokhande, V.J. Fulari, Chemical synthesis of Fe_2O_3 thin films for supercapacitor application, J. Alloys Compd., 509 (2011) 2567-2571.

[103]. J. Santos-Peña, O. Crosnier, T. Brousse, Nanosized α-$LiFeO_2$ as electrochemical supercapacitor electrode in neutral sulfate electrolytes, Electrochim. Acta, 55 (2010) 7511-7515.

[104]. S.-Y. Wang, K.-C. Ho, S.-L. Kuo, N.-L. Wu, Investigation on capacitance mechanisms of Fe_3O_4 electrochemical capacitors, J. Electrochem. Soc., 153 (2006) A75-A80.

[105]. G.A. Snook, P. Kao, A.S. Best, Conducting-polymer-based supercapacitor devices and electrodes, J. Power Sources, 196 (2011) 1-12.

[106]. K.S. Ryu, Y.G. Lee, Y.S. Hong, Y.J. Park, X.L. Wu, K.M. Kim, M.G. Kang, N.G. Park, S.H. Chang, Poly(ethylenedioxythiophene) (PEDOT) as polymer electrode in redox supercapacitor, Electrochim. Acta, 50 (2004) 843-847.

[107]. N. Oyama, O. Hatozaki, Lithium polymer battery with high energy density, Macromol. Symp., 156 (2000) 171-178.

[108]. M. Hughes, G.Z. Chen, M.S.P. Shaffer, D.J. Fray, A.H. Windle, Controlling the nanostructure of electrochemically grown nanoporous composites of carbon nanotubes and conducting polymers, Compos. Sci. Technol., 64 (2004) 2325-2331.

[109]. I. Boyano, M. Bengoechea, I. de Meatza, O. Miguel, I. Cantero, E. Ochoteco, J. Rodriguez, M. Lira-Cantu, P. Gomez-Romero, Improvement in the Ppy/V_2O_5 hybrid as a cathode material for Li ion batteries using PSA as an organic additive J. Power Sources, 166 (2007) 471-477.

[110]. K.S. Ryu, K.M. Kim, N.G. Park, Y.J. Park, S.H. Chang, Symmetric redox supercapacitor with conducting polyaniline electrodes, J. Power Sources, 103 (2002) 305-309.

[111]. H. Talbi, P.E. Just, L.H. Dao, Electropolymerization of aniline on carbonized polyacrylonitrile aerogel electrodes: applications for supercapacitors, J. Appl. Electrochem., 33 (2003) 465-473.

[112]. K.S. Ryu, K.M. Kim, Y.J. Park, N.G. Park, M.G. Kang, S.H. Chang, Redox supercapacitor using polyaniline doped with Li salt as electrode, Solid State Ionics, 152 (2002) 861-866.

[113]. D.S. Dhawale, A. Vinu, C.D. lokhande, Stable nanostructured polyaniline electrode for supercapacitor application, Electrochim. Acta, 56 (2011) 9482-9487.

[114]. S.H. Mujawar, S.B. Ambade, T. Battumur, R.B. Ambade, S.-H. Lee, Electropolymerization of polyaniline on titanium oxide nanotubes for supercapacitor application, Electrochim. Acta, 56 (2011) 4462-4466.

[115]. L.-J. Sun, X.-X. Liu, K. Laub, L. Chena, W.-M. Gu, Electrodeposited hybrid films of polyaniline and manganese oxide in nanofibrous structures for electrochemical supercapacitor, Electrochim. Acta, 53 (2008) 3036-3042.

[116]. M.D. Ingram, H. Staesche, K.S. Ryder, 'Activated' polypyrrole electrodes for high-power supercapacitor applications, Solid State Ionics, 169 (2004) 51-57.

[117]. K. Naoi, Y. Oura, M. Meada, S. Nakamura, Electrochemistry of surfactant-doped polypyrrole film(I): formation of columnar structure by electropolymerization, J. Electrochem. Soc., 142 (1995) 417-422.

[118]. R.K. Sharma, A.C. Rastogi, S.B. Desu, Pulse polymerized polypyrrole electrodes for high energy density electrochemical supercapacitor, Electrochem. Commun., 10 (2008) 268-272.

[119]. H. An, Y. Wang, X. Wang, L. Zheng, X. Wang, Polypyrrole/carbon aerogel composite materials for supercapacitor, J. Power Sources, 195 (2010) 6964-6969.

[120]. K. Naoi, Y. Oura, H. Tsujimoto, in: F.M. Delnick, D. Ingersoll, X. Andrieu, K. Naoi (Eds.), Proceedings of the symposium on electrochemical capacitors Ii, Electrochemical Society Inc, Pennington, 1997, 120-126.

[121]. S. Suematsu, Y. Oura, H. Tsujimoto, H. Kanno, K. Naoi, Conducting polymer films of cross-linked structure and their QCM analysis, Electrochim. Acta, 45 (2000) 3813-3821.

[122]. T.A. Skotheim, R.L. Elsenbaumer, J.R. Reynolds (Eds.), Handbook of Conducting Polymers, Marcel Decker, New York, 1998, p. 225.

[123]. S.J. Lee, J.M. Lee, I.W. Cheong, H. Lee, J.H. Kim, A facile route of polythiophene nanoparticles via Fe^{3+}-catalyzed oxidative polymerization in aqueous medium, J. Polym. Sci.: Part A: Polym. Chem., 46 (2008) 2097-2107.

[124]. J.M. Pringle, M. Forsyth, D.R. MacFarlane, K. Wagner, S.B. Hall, D.L. Officer, The influence of the monomer and the ionic liquid on the electrochemical preparation of polythiophene, Poly., 46 (2005) 2047-2058.

[125]. D. Reyman, E. Guereca, P. Herrasti, Electrodeposition of polythiophene assisted by sonochemistry and incorporation of fluorophores in the polymeric matrix, Ultrason. Sonochem., 14 (2007) 653-660.

[126]. M.G. Voronkov, I.A. Tokareva, I.A. Dorofeev, V.I. Smirnov, L.G. Shagun, Photochemical synthesis of polythiophenes and polythienylphenylenes, Russ. J. Gen. Chem., 80 (2010) 2075-2077.

[127]. B. Ballarin, M. Facchini, L. Dal Pozzo, C. Martini, Comparison of different porous sol-gel matrices: template synthesis of polythiophene, Electrochem. Commun., 5 (2003) 625-631.

[128]. D. Villers, D. Jobin, C. Soucy, D. Cossement, R. Chahine, L. Breau, D. Belanger, The influence of the range of electroactivity and capacitance of conducting polymers on the performance of carbon conducting polymer hybrid supercapacitor, J. Electrochem. Soc., 150 (2003) A747-A752.

[129]. A. Gok, M. Omastova, A.G. Yavuz, Synthesis and characterization of polythiophenes prepared in the presence of surfactants, Synth. Met., 157 (2007) 23-29.

[130]. B. Senthilkumar, P. Thenamirtham, R. Kalai Selvan, Structural and electrochemical properties of polythiophene, Applied Surf. Sci., 257 (2011) 9063-9067.

[131]. F. Alvi, M.K. Ram, P.A. Basnayaka, E. Stefanakos, Y. Goswami, A. Kumar, Graphene-polyethylenedioxythiophene conducting polymer nanocomposite based supercapacitor, Electrochim. Acta, 56 (2011) 9406-9412.

[132]. R. Liu, I.S. Cho, S.B. Lee, Poly(3,4-ethylenedioxythiophene) nanotubes as electrode materials for a high-powered supercapacitor, Nanotechnol., 19 (2008) 215710-215717.

[133]. T.L. Kelly, K. Yano, M.O. Wolf, Supercapacitive properties of PEDOT and carbon colloidal microspheres, ACS Appl. Mater. Interf., 1 (2009) 2536-2543.

[134]. F. Alvi, M.K. Ram, P.A. Basnayaka, E. Stefanakos, Y. Goswami, A. Kumar, Graphene-polyethylenedioxythiophene conducting polymer nanocomposite based supercapacitor, Electrochim. Acta, 56 (2011) 9406-9412.

[135]. S. Panero, A. Clemente, E. Spila, Solid state supercapacitors using gel membranes as electrolytes, Solid State Ionics, 86-88 (1996) 1285-1289.

[136]. A. Yamada, J.B. Goodenough, Keggin-type heteropolyacids as electrode materials for electrochemical supercapacitors, J. Electrochem. Soc., 145 (1998) 737-743.

[137]. K.-W. Park, H.-J. Ahn, Y.-E. Sung, All-solid-state supercapacitor using a Nafion® polymer membrane and its hybridization with a direct methanol fuel cell, J. Power Sources, 109 (2002) 500-506.

[138]. P. Sivaraman, S.K. Rath, V.R. Hande, A.P. Thakur, M. Patri, A.B. Samui, All-solid-supercapacitor based on polyaniline and sulfonated polymers, Synthetic Metals, 156 (2006) 1057-1064.

[139]. F. Lufrano, P. Staiti, Performance improvement of Nafion based solid state electrochemical supercapacitor, Electrochimica. Acta, 49 (2004) 2683-2689.

[140]. K.S. Ryu, Y.-S. Hong, Y.J. Park, X. Wu, K.M. Kim, Y.-G. Lee, S.H. Chang, S.J. Lee, Polyaniline doped with dimethylsulfate as a polymer electrode for all-solid-state power source system, Solid State Ionics, 175 (2004) 759-763.

[141]. Y.S. Yoon, W.I. Cho, J.H. Lim, D.J. Choi, Solid-state thin-film supercapacitor with ruthenium oxide and solid electrolyte thin films, J. Power Sources, 101 (2001) 126-129.

[142]. Y.G. Wang, X.G. Zhang, All solid-state supercapacitor with phosphotungstic acid as the proton-conducting electrolyte, Solid State Ionics, 166 (2002) 61-67.

[143]. A.M. White, R.C.T Slade, Polymer electrodes doped with heteropolymetallates and their use within solid-state supercapacitors, Synth. Met., 139 (2003) 123-131.

[144]. W.G. Pell, B.E. Conway, Analysis of power limitations at porous supercapacitor electrodes under cyclic voltammetry modulation and dc charge, J. Power Sources, 96 (2001) 57-67.

[145]. H.R. Ghenaatiana, M.F. Mousavi, S.H. Kazemia, M. Shamsipur, Electrochemical investigations of self-doped polyaniline nanofibers as a new electroactive material for high performance redox supercapacitor, Synth. Met., 159 (2009) 1717-1722.

[146]. W. Sun, X. Chen, Preparation and characterization of polypyrrole films for three-dimensional micro supercapacitor, J. Power Sources, 193 (2009) 924-929.

[147]. W. Yang, Z. Gao, J. Wang, B. Wang, Q. Liu, Z. Li, T. Mann, P. Yang, M. Zhang, L. Liu, Synthesis of reduced grapheme nanosheet/urchin-like manganese dioxide composite and high performance as supercapacitor electrode, Electrochim. Acta, 69 (2012) 112-119.

[148]. Z.S. Mo, K.B. Lee, Y.B. Moon, M. Kobayashi, A.J. Heeger, F. Wudl, X-ray scattering from poly(thiophene): crystallinity and crystallographic structure, Macromol., 18 (1985) 1972-1977.

[149]. Y.G. Andreev, P. Lightfoot, P.G. Bruce, Structure of the polymer electrolyte poly(ethylene oxide)$_3$:LiN(SO_2CF_3)$_2$ determined by powder diffraction using a powerful Monte Carlo approach, Chem. Commun., 18 (1996) 2169-2170.

[150]. M. DeBroglie, La spectrographie des phénomènes d'absorption des rayons X, J. Phys. 5 (1916) 161-168.

[151]. R.A. Van Nordsthand, The use of x-ray k-absorption edges in the study of catalytical active solids, Adv. Catal., 12 (1960) 149-187.

[152]. D.E. Sayers, E.A. Stern, F.W. Lytle, New technique for investigating noncrystalline structures: Fourier analysis of the extended X-ray—absorption fine structure, Phys. Rev. Lett., 27 (1971) 1204-1207.

[153]. J.-K. Chang, M.-T. Lee, W.-T. Tsai, *In situ* Mn K-edge X-ray absorption spectroscopic studies of anodically deposited manganese oxide with relevance to supercapacitor applications, J. Power Sources, 166 (2007) 590-594.

[154]. M.-T. Lee, W.-T. Tsai, M.-J. Deng, H.-F. Cheng, I-W. Sun, J.-K. Chang, Pseudocapacitance of MnO_2 originates from reversible insertion/desertion of thiocyanate anions studied using *in situ* X-ray absorption spectroscopy in ionic liquid electrolyte, J. Power Sources, 195 (2010) 919-922.

[155]. N. Watanabe, J. Morais, M.C.M. Alves, Design of an electrochemical cell for *in situ* XAS studies, J. Electron. Spectrosc. Relat. Phenom., 156-158 (2007) 164–167.

[156]. H.-W. Chan, J.-G. Duh, J.-F. Lee, Valence change by *in situ* XAS in surface modified $LiMn_2O_4$ for Li-ion battery, Electrochem. Commun., 8 (2006) 1731-1736.

[157]. M. Balasubramanian, X. Sun, X.Q. Yang, J. McBreen, *In situ* X-ray diffraction and X-ray absorption studies of high-rate lithium-ion batteries, J. Power Sources, 92 (2001) 1-8.

[158]. A. Deb, U. Bergmann, S.P. Cramer, E.J. Cairnsa, *In situ* X-ray absorption spectroscopic study of $Li_{1.05}Ni_{0.35}Co_{0.25}Mn_{0.4}O_2$ cathode material coated with $LiCoO_2$, J. Electrochem. Soc., 154(6), (2007) A534-A541.

[159]. H. Siegenthaler, in: R. Wiesendanger, H.J. Gu¨ntherodt (Eds.), Scanning Tunneling Microscopy II, Springer Series Surface Science, vol. 28, Springer, Berlin, 1992, pp. 7/49.

[160]. W.J. Lorenz, W. Plieth (Eds.), Electrochemical Nanotechnology: In-situ Local Probe Techniques at Electrochemical Interfaces, Wiley-VCH, Weinheim, 1998.

[161]. E. Budevski, G. Staikov, W.J. Lorenz, Electrochemical Phase Formation and Growth: An Introduction to the Initial Stages of Metal Deposition, VCH, Weinheim, 1996.

[162]. A.J. Bard, M.V. Mirkin (Eds.), Scanning Electrochemical Microscopy, Marcel Dekker, New York, NY, 2001.

[163]. A.J. Bard, M.V. Mirkin, D.O. Wipf, in: A.J. Bard (Ed.), Electroanalytical Chemistry, vol. 18, Marcel Dekker, New York, NY, 1994, pp. 243/370.

[164]. R.C. Engstrom, C.M. Pharr, Scanning electrochemical microscopy, Anal. Chem. 61 (1989) 1099A-1104A.

[165]. H. Shiku, T. Matsue, in: H. Baltes, W. Go¨ pel, J. Hesse (Eds.), Sensors Update, vol. 6, Wiley-VCH, Weinheim, 2000, pp. 231/242.

[166]. D.E. Williams, T.F. Mohiuddin, Y.Y. Zhu, Elucidation of a trigger mechanism for pitting corrosion of stainless steels using submicron resolution scanning electrochemical and photoelectrochemical microscopy, J. Electrochem. Soc. 145 (1998) 2664-2672.

[167]. A.R. Kucernak, P.B. Chowdhury, C.P. Wilde, G.H. Kelsall, Y.Y. Zhu, D.E. Williams, Electrochim. Acta 45 (2000) 4483.

[168]. J.V. Macpherson, P.R. Unwin, Noncontact electrochemical imaging with combined scanning electrochemical atomic force microscopy, Anal. Chem. 73 (2001) 550-557.

[169]. J.V. Macpherson, C.E. Jones, A.L. Barker, P.R. Unwin, Electrochemical imaging of diffusion through single nanoscale pores, Anal. Chem. 74 (2002) 1841-1848.

[170]. J. Meier, K.A. Friedrich, U. Stimming, Novel method for the investigation of single nanoparticle reactivity, Faraday Discuss., 121 (2002) 365-372.

[171]. J. Hafner, Atomic-scale computational materials science, Acta Mater., 48 (2000) 71-92.

[172]. P. Hohenberg, W. Kohn, Inhomogeneous electron gas, Phys. Rev. B 136 (1964) B864-B871.

[173]. W. Kohn, L. J. Sham, Self-consistent equations including exchange and correlations effects, Phys. Rev., 140 (1965) A1133-A1138.

[174]. K. D. Kreuer, S. J. Paddison, E. Spohr, M. Schuster, Transport in proton conductors for fuel-cell applications: simulations, elementary reactions, and phenomenology, Chem. Rev., 104 (2004) 4637-4678.

[175]. D. Seeliger, C. Hartnig, E. Spohr, Aqueous pore structure and proton dynamics in solvated Nafion membranes, Electrochim. Acta, 50 (2005) 4234-4240.

[176]. W. A. Goddard III, T. Cagin, M. Blanco, N. Vaidehi, S. Dasgupta, W. Floriano, M. Belmares, J. Kua, G. Zamanakos, S. Kashihara, M. Iotov, G. Gao, Strategies for multiscale modeling and simulation of organic materials: polymers and biopolymers, Comput. Theor. Polym. Sci., 11 (2001) 329-343.

[177]. A. Zunger, A. Franceschetti, G. Bester, W. B. Jones, K. Kim, P. A. Graf, L-W. Wang, A. Canning, O. Marques, C. Voemel, J. Dongarra, J. Langou, S. Tomov, Predicting the electron properties of 3D, million-atom semiconductor nanostructure architectures, J. Phys. B: Conference Series, 46 (2006) 292-298.

[178]. R. Car, M. Parrinello, Unified approach for molecular dynamics and density-functional theory, Phys. Rev. Lett., 55 (1985) 2471-2474.

[179]. M. P. Allen, Introduction to molecular dynamics simulation, Computational Soft Matter: From Synthetic Polymers to Proteins, 23 (2004) 1-27.

[180]. S.L. Mayo, B.D. Olafson, W.A. Goddard III, DREIDING: a generic force field for molecular simulations, J. Phys. Chem., 94 (1990) 8897-8909.

[181]. S. Walbran and A. A. Kornysheva, Proton transport in polarizable water, J. Chem. Phys., 114 (2001) 10039-10048.

[182]. W. Goddard III, B. Merinov, A. V. Duin, T. Jacob, M. Blanco, V. Molinero, S.S. Jang, Y. H. Jang, Multi-paradigm multi-scale simulations for fuel cell catalysts and membranes, Mol. Simul., 32 (2006) 251-268.

[183]. P. Jannasch, Recent developments in high-temperature proton conducting polymer electrolyte membranes, Curr. Opin. Colloid Interface Sci., 8 (2003) 96-102.

[184]. E. Chalkova, X. Zhou, C. Ambler, M. A. Hofmann, J. A. Weston, H. R. Allcock, S. N. Lvov, Sulfonimide polyphosphazene-based H_2/O_2 fuel cells, Electrochem. Solid-State Lett. 5 (2002) A221-A222.

[185]. P. Spinelli, C. Francia, E. P. Ambrosio, M. Lucariello, Semi-empirical evaluation of PEMFC electro-catalytic activity, J. Power Sources, 178 (2008) 517-524.

[186]. M. D. Macia, J. M. Campina, E. Herrero, J. M. Feliu, On the kinetics of oxygen reduction on platinum stepped surfaces in acidic media, J. Electroanal. Chem., 564 (2004) 141-150.

[187]. M. Watanabe, S. Motto, Electrocatalysis by ad-atoms: Part III. Enhancement of the oxidation of carbon monoxide on platinum by ruthenium ad-atoms, J. Electroanal. Chem., 60 (1975) 275-283.

[188]. J. Kua, W. A. Goddard III, Oxidation of methanol on 2nd and 3rd row group VIII transition metals (Pt, Ir, Os, Pd, Rh, and Ru): application to direct methanol fuel cells, J. Am. Chem. Soc., 121 (1999) 10928-10941.

[189]. A. B. Anderson, E. Grantscharova, S. Seong, Systematic theoretical study of alloys of platinum for enhanced methanol fuel cell performance, J. Electrochem. Soc., 143 (1996) 2075-2082.

[190]. A. B. Anderson, Electron density distribution functions and the ASED-MO theory, Int. J. Quantum Chem., 49 (1994) 581-589.

[191]. T. Jacob, B. V. Merinov, W. A. Goodard III, Chemisorption of atomic oxygen on Pt(1 1 1) and Pt/Ni(1 1 1) surfac, 143 (1996) 2075-2082.es, Chem. Phys. Lett., 385 (2004) 374-377.

[192]. G. Barabino, C. Gavotti, M. Marchesi, Molecular dynamics simulation of water near walls using an improved wall-water interaction potential, Chem. Phys. Lett., 104 (1984) 478-484.

[193]. C. Y. Lee, J. A. McCammon, P. J. Rossky, The structure of liquid water at an extended hydrophobic surface, J. Chem. Phys., 80 (1984) 4448-4455.

[194]. E. Spohr, K. Heinzinger, Computer simulations of water and aqueous electrolyte solutions at interfaces, Electrochim. Acta 33 (1988) 1211-1222.

[195]. P. S. Crozier, R. L. Rowley, D. Henderson, Molecular dynamics calculations of the electrochemical properties of electrolyte systems between charged electrodes, J. Chem. Phys., 113 (2000) 9202-9207.

[196]. C. Hartnig, M. T. M. Koper, Molecular dynamics simulation of solvent reorganization in ion transfer reactions near a smooth and corrugated surface, J. Phys. Chem. B, 108 (2004) 3824-3827.

[197]. E. Spohr, Computer simulation of the water/platinum interface, J. Phys. Chem., 93 (1989) 6171-6180.

[198]. J. I. Siepmann, M. Sprik, Influence of surface topology and electrostatic potential on water/electrode systems, J. Chem. Phys., 102 (1995) 511-524.

[199]. I.-C. Yeh, M. L. Berkowitz, Aqueous solution near charged Ag(111) surfaces: comparison between a computer simulation and experiment, Chem. Phys. Lett., 301 (1999) 81-86.

[200]. E. Spohr, Effect of electrostatic boundary conditions and system size on the interfacial properties of water and aqueous solutions, J. Chem. Phys., 107 (1997) 6342-6348.

[201]. E. Spohr, Some recent trends in computer simulations of aqueous double layers, Electrochim. Acta, 49 (2003) 23-27.

[202]. D. L. Price, J. W. Halley, Molecular dynamics, density functional theory of the metal–electrolyte interface, J. Chem. Phys., 102 (1995) 6603-6612.

[203]. J. W. Halley, A. Mazzolo, Y. Zhou, and D. Price, First-principles simulations of the electrode|electrolyte interface, J. Electroanal. Chem., 450 (1998) 273-280.

[204]. S. Izvekov, A. Mazzolo, K. VanOpdorp, G. A. Voth, *Ab initio* molecular dynamics simulation of the Cu(110)-water interface, J. Chem. Phys., 114 (2001) 3248-3257.

[205]. P. Vassilev, R. A. van Santen, M. T. M. Koper, *Ab initio* studies of a water layer at transition metal surfaces, J. Chem. Phys., 122 (2005) 054701.

[206]. A. B. Anderson, N. C. Debnath, Mechanism of Iron dissolution and passivation in an aqueous environment: Active and transition ranges, J. Am. Chem. Soc. 105 (1983) 18-22.

[207]. S. Seong, A. B. Anderson, Water dissociation on Pt(111) and (100) anodes: molecular orbital theory, J. Phys. Chem., 100 (1996) 11744-11747.

[208]. A. B. Anderson, T. V. Albu, *Ab Initio* determination of reversible potentials and activation energies for outer-sphere oxygen reduction to water and the reverse oxidation reaction, J. Am. Chem. Soc., 121 (1999) 11855-11863.

[209]. T. V. Albu, A. B. Anderson, Studies of model dependence in an *ab initio* approach to uncatalyzed oxygen reduction and the calculation of transfer coefficients, Electrochim. Acta, 46 (2001) 3001-3013.

[210]. R. A. Sidik, A. B. Anderson, Density functional theory study of O_2 electroreduction when bonded to a Pt dual sitek, J. Electroanal. Chem., 528 (2002) 69-76.

[211]. A. B. Anderson, N. M. Neshev, R. A. Sidik, P. Shiller, Mechanism for the electrooxidation of water to OH and O bonded to platinum: quantum chemical theory, Electrochim. Acta, 47 (2002) 2999-3008.

[212]. A. B. Anderson, Theory at the electrochemical interface: reversible potentials and potential-dependent activation energies, Electrochim. Acta, 48 (2003) 3743-3749.

[213]. J. Narayanasamy, A. B. Anderson, Calculating reversible potentials for elementary reactions in acid and base from model reaction energies, J. Phys. Chem. B, 107 (2003) 6898-6901.

[214]. M. F. Toney, J. N. Howard, J. Richer, G. L. Borges, J. G. Gordon, O. R. Melroy, D. G. Wiesler, D. Yee, L. B. Sorensen, Voltage-dependent ordering of water molecules at an electrode-electrolyte interface, Nature, 368 (1994) 444-446.

[215]. Y. Lozovoi, A. Alavi, J. Kohanoff, R. M. Lynden-Bell, *Ab initio* simulation of charged slabs at constant chemical potential, J. Chem. Phys., 115 (2001) 1661-1669.

[216]. J.-S. Filhol, M. Neurock, Elucidation of the electrochemical activation of water over Pd by first principles, Angew. Chem. Int. Ed., 45 (2006) 402-406.

[217]. C. D. Taylor, S. A. Wasileski, J.-S. Filhol, M. Neurock, First principles reaction modeling of the electrochemical interface: Consideration and calculation of a tunable surface potential from atomic and electronic structure, Phys. Rev., B 73 (2006) 165402.

[218]. M. J. Janik, C. D. Taylor, M Neurock, First-principles analysis of the initial electroreduction steps of oxygen over Pt(111), J. Electrochem. Soc., 156 (2009) B126-B135.

[219]. K. Raghavan, K. Foster, K. Motakabbir, M. Berkowitz, Structure and dynamics of water at the Pt(111) interface: molecular dynamics study, J. Chem. Phys., 94 (1991) 2110-2117.

[220]. E. Spohr, Computer simulation of the water/platinum interface, J. Phys. Chem., 93 (1989) 6171-6180.

[221]. S. Senapati, A. Chandra, Surface charge induced modifications of the structure and dynamics of mixed dipolar liquids at solid–liquid interfaces: A molecular dynamics simulation study, J. Chem. Phys., 113 (2000) 8817-8826.

[222]. X. Xia, M. L. Berkowitz, Electric-field induced restructuring of water at a platinum-water interface: a molecular dynamics computer simulation, Phys. Rev. Lett., 74 (1995) 3193-3196.

[223]. I.-C. Yeh, M. L. Berkowitz, Effects of the polarizability and water density constraint on the structure of water near charged surfaces: Molecular dynamics simulations, J. Chem. Phys., 112 (2000) 10491-10495.

[224]. P. G. Kusalik, I. M. Svishchev, The spatial structure in liquid water, Science, 265 (1994) 1219-1221.

[225]. I. M. Svishchev, P. G. Kusalik, J. Wang, R. J. Boyd, Polarizable point‐charge model for water: results under normal and extreme conditions, J. Chem. Phys., 105 (1996) 4742-4750.

[226]. M. F. Toney, J. N. Howard, J. Richer, G. L. Borges, J. G. Gordon, O. R. Melroy, D. G. Wiesler, D. Yee, L. D. Sorensen, Distribution of water molecules at Ag(111)/electrolyte interface as studied with surface X-ray scattering, Surf. Sci., 335 (1995) 326-332.

[227]. P. B. Balbuena, E. J. Lamas, Y. Wang, Molecular modeling studies of polymer electrolytes for power sources, Electrochim. Acta, 50 (2005) 3788-3795.

[228]. Adri C. T. van Duin, Siddharth Dasgupta, Francois Lorant, William A. Goddard, ReaxFF: a reactive force field for hydrocarbons, J. Phys. Chem. A, 105 (2001) 9396-9409.

[229]. B. Hammer, J. K. Nørskov, Theoretical surface science and catalysis-calculations and concepts, Adv. Catal., 45 (2000) 71-129.

[230]. B. Hammer, L. B. Hansen, J. K. Nørskov, Improved adsorption energetics within density-functional theory using revised Perdew-Burke-Ernzerhof functional, Phys. Rev. B, 59 (1999) 7413-7421.

[231]. A. Damjanovic, V. Brusic, Electrode kinetics of oxygen reduction on oxide-free platinum electrodes, Electrochim. Acta, 12 (1967) 615-628.

[232]. E. Yeager, M. Razaq, D. Gervasio, A. Razaq, D. Tryk, Proceedings of the workshop on structural effects in electrocatalysis and oxygen electrochemistry, Cleveland, OH, The Electrochemical Society, 92 (1991) 440-473.

[233]. C. D. Taylor, M. J. Janik, M. Neurock, R. G. Kelly, *Ab initio* simulations of the electrochemi-cal activation of water, Mol. Simul., 33 (2007) 429-436.

[234]. M. J. Janik, M. Neurock, A first principles analysis of the electro-oxidation of CO over Pt(1 1 1), Electrochim. Acta, 52 (2007) 5517-5528.

[235]. A. B. Anderson, T. V. Albu, Catalytic effect of platinum on oxygen reduction an *ab initio* model including electrode potential dependence, J. Electrochem. Soc., 147 (2000) 4229-4238.

[236]. T. Li, P. B. Balbuena, Oxygen reduction on a platinum cluster, Chem. Phys. Lett., 367 (2003) 439-447.

[237]. J. K. Nørskov, J. Rossmeisl, A. Logadottir, L. Lindqvist, J. R. Kitchin, T. Bligaard, H. Jónsson, Origin of the overpotential for oxygen reduction at a fuel-cell cathode, J. Phys. Chem. B, 108 (2004) 17886-17892.

[238]. R. Jinnouchi, K. Okazaki, New insight into microscale transport phenomena in PEFC by quantum MD, Microscale Thermophys. Eng., 7 (2003) 15-31.

[239]. Y. Wang, P. B. Balbuena, *Ab initio* molecular dynamics simulations of the oxygen reduction reaction on a Pt(111) surface in the presence of hydrated hydronium $(H_3O)^+(H_2O)_2$, J. Phys. Chem. B, 109 (2005) 14896-14907.

[240]. X. Zhou, J. Weston, E. Chalkova, M. A. Hofmann, C. M. Ambler, H. R. Allcock, A. N. Lvov, High temperature transport properties of polyphosphazene membranes for direct methanol fuel cells, Electrochim. Acta, 48 (2003) 2173-2180.

[241]. D.E. Sayers, S. M. Heald, M. A. Pick, J. I. Budnick, E.A. Stern, and J. Wong, X-ray beam line at the NSLS for X-ray absorption studies in material science, Nucl. Instrum. Methods Phys. Res., 208 (1983) 631-635.

[242]. E.A. Stern, M. Newville, B. Ravel, Y. Yacoby, D. Haskel, The UWXAFS analysis package: philosophy and details, Physica B, 208-209 (1995) 117-120.

[243]. A.L. Ankuudinov, B. Ravel, J.J. Rehr, S.D. Conradson, Real-space multiple-scattering calculation and interpretation of x-ray-absorption near-edge structure, Phys. Rev. B., 58 (1998) 7565-7576.

[244]. A.L. Ankudinov, C.E. Boulden, J.J. Rehr, J. Sims, H. Hung, Parallel calculation of electron multiple scattering using Lanczos algorithms, Phys. Rev. B, 65 (2002) 104107-1-104107-11.

[245]. R.W.G. Wyckoff, Crystal Structures, vol. 1, 2nd edition, Robert E. Krieger Publishing Company, Malbar, FL, 1982, p. 53.

[246]. F. van Bolhuis, P.B. Koster and T. Migchelsen, Refinement of the crystal structure of iodine at 110° K, Acta Cryst., 23 (1967) 90-91.

[247]. E.A. Stern, Number of relevant independent points in x-ray-absorption fine-structure spectra, Phys. Rev. B, 48 (1993) 9825-9827.

[248]. R. Kawano and M. Watanabe, Equilibrium potentials and charge transport of an I^-/I_3^- redox couple in an ionic liquid, Chem. Commun., (2003) 330-332.

[249]. I. Ruff and V. J. Friedrich, Transfer diffusion. I. Theoretical, J. Phys. Chem., 75 (1971) 3297-3302.

[250]. H. Dahms, Electronic conduction in aqueous solution, J. Phys. Chem., 72 (1968) 362-364.

[251]. I. Ruff and L. Botár, Effect of exchange reactions on transport processes: A comparison of thermodynamic treatment with random walk on lattice points, J. Chem. Phys., 83 (1985) 1292-1297.

[252]. Y. G. Wang, Z. D. Wang, and Y. Y. Xia, An asymmetric supercapacitor using RuO_2/TiO_2 nanotube composite and activated carbon electrodes, Electrochim. Acta, 50 (2005) 5641-5646.

[253]. R. Jiang, T. Huang, Y. Tang, J. Liu, L. Xue, J. Zhuang, A. Yu, Factors influencing MnO_2/multi-walled carbon nanotubes composite's electrochemical performance as supercapacitor electrode, Electrochim. Acta, 54 (2009) 7173-7179.

[254]. C.M. Pettit, P.C. Goonetilleke, D. Roy, Measurement of differential capacitance for faradaic systems under potentiodynamic conditions: considerations of Fourier transform and phase-selective techniques, J. Electroanal. Chem., 589 (2006) 219-231.

[255]. M. Pourbaix, Atlas d'Équilibres Électrochimiques, p. 614, Gauthier-Villars, Paris 1963.

[256]. J. H. Chae, K. C. ng, and G. Z. Chen, Nanostructured materials for the construction of asymmetrical supercapacitors, J. Power Energy, 224 (2010) 479-503.

[257]. G. Lota and E. Frackowiak, Striking capacitance of carbon/iodide interface, Electrochem. Commun., 11 (2009) 87-90.

[258]. S. H. Glarum and J. H. Marshall, The *in situ* ESR and electrochemical behavior of Poly(aniline) electrode films, J. Electrochem. Soc., 134 (1987) 2160-2165.

[259]. D. Kalpana, K. S. Omkumar, S. S. Kumar, and N. G. Renganathan, A novel high power symmetric ZnO/carbon aerogel composite electrode for electrochemical supercapacitor, Electrochim. Acta, 52 (2006) 1309-1315.

[260]. K. S. Ryu, Y. Lee, K.-S. Han, Y. J. Park, M. G. Kang, N.-G. Park, and S. H. Chang, Electrochemical supercapacitor based on polyaniline doped with lithium salt and active carbon electrodes, Solid State Ionics, 175 (2004) 765-768.

[261]. N. W. Duffy, W. Baldsing, and A. G. Pandolfo, The nickel-carbon asymmetric supercapacitor—Performance, energy density and electrode mass ratios, Electrochim. Acta, 54 (2008) 535-539.

[262]. W. Sun, R. Zheng, and X. Chen, Symmetric redox supercapacitor based on micro-fabrication with three-dimensional polypyrrole electrodes, J. Power Sources, 195 (2010) 7120-7125.

[263]. W. A. Henderson and S. Passerini, Ionic conductivity in crystalline–amorphous polymer electrolytes – $P(EO)_6$: LiX phases, Electrochem. Commun., 5 (2003) 575-578.

[264]. M. J. Reddy, J. S. Kumar, U. V. S. Rao, and P. P. Chu, Structural and ionic conductivity of PEO blend PEG solid polymer electrolyte, Solid State Ionics, 3-4 (2006) 253-256.

[265]. A.F. Wells, Structural Inorganic Chemistry, 5th edition, Oxford University Press Inc., NY, 1984, p.286.

[266]. U. Buontempo, A. Di Cicco, A. Fillipponi, M. Nardone, P. Postorino, Determination of the I_2 bond-length distribution in liquid, solid and solution, by extended x-ray absorption fine structure spectroscopy, J. Chem. Phys., 107 (1997) 5720-5726.

[267]. U. Buontempo, A. Fillipponi D. Martinez-Garcia, P. Postorino, M. Mezouar, and J.P. Itie, Anomalous bond length expansion in liquid iodine at high pressure, Phys. Rev. Lett., 80 (1998) 1912-1915.

[268]. Y. Chatani and S. Okamura, Crystal structure of poly(ethylene oxide)—sodium iodide complex, Polymer, 28 (1987) 1815-1820.

[269]. M.O. Krause and J.H. Oliver, Natural widths of atomic K and L levels, Ka X-ray lines and several KLL auger lines, J. Phys. Chem. Ref. Data, 8 (1979), 329-338.

[270]. X. Hou, V. Hansen, A. Aldahan, G. Possnert, O.C. Lind, and G. Lujaniene, A review on speciation of iodine-129 in the environmental and biological samples, Analytica Chimica Acta, 632 (2009) 181-196.

[271]. A.F. Wells, Structural Inorganic Chemistry, 5th edition, Oxford University Press, New York, 1984, p. 396-399.

[272]. T. Bernstein, F.H. Herbstein, The crystal structure of ferricinium triiodide, $(C_5H_5)_2FeI_3$, Acta Cryst., B24 (1968) 1640-1645.

[273]. J. Zhou, Y. Yin, X. Zhou, A. N. Mansour, Experimental studies of mediator-enhanced polymer electrolyte supercapacitors, Electrochem. Solid-state Lett., 14 (2010) A25-A28.

[274]. Y. Yin, J. Zhou, A. N. Mansour, X. Zhou, Effect of NaI/I_2 mediators on properties of $PEO/LiAlO_2$ based all-solid-state supercapacitors, J. Power Sources, 196 (2011) 5997-6002.

[275]. M. Armand, Polymer solid electrolytes - an overview, Solid State Ionics, 9-10 (1983) 745-754.

[276]. T. Itoh, M. Ikeda, N. Hirata, Y. Moriya, M. Kubo, O. Yamamoto, Ionic conductivity of the hyperbranched polymer-lithium metal salt systems, J. Power Sources, 81-82 (1999) 824-829.

[277]. P. Majsztrik, A. Bocarsly, J. Benziger, Water permeation through Nafion membranes: the role of water activity, J. Phys. Chem. B, 112 (2008) 16280-16289.

[278]. E. Tsuchida, H. Ohno, K. Tsunemi, A mechanism of ionic conduction of poly (vinylidene fluoride)-lithium perchlorate hybrid films, Electrochimi. Acta, 28 (1983) 833-837.

[279]. R. Jiang, T. Huang, Y. Tang, J. Liu, L. Xue, J. Zhuang, A. Yu, Factors influencing MnO_2/multi-walled carbon nanotubes composite's electrochemical performance as supercapacitor electrode, Electrochimi. Acta, 54 (2009) 7173-7179.

[280]. G. Lota, K. Lota, E. Frackowiak, Nanotubes based composites rich in nitrogen for supercapacitor application, Electrochem. Commun., 9 (2007) 1828-1832.

[281]. G. M. Suppes, B.A. Deore, M.S. Freund, Porous conducting polymer/heteropolyoxometalate hybrid material for electrochemical supercapacitor applications, Langmuir, (2008) 1064-1069.

[282]. F. Cebeci, E. Sezer, A. SezaiSarac, A novel EDOT–nonylbithiazole–EDOT based comonomer as an active electrode material for supercapacitor applications, Electrochim. Acta, (2009) 6354-6360.

[283]. J. Lee, Y. Lee, W. Chae, Y. Sung, Enhanced ionic conductivity in $PEO\text{-}LiClO_4$ hybrid electrolyte by structural modification, J. Electroceram., 17 (2006) 941-944.

[284]. T. Ikeshoji, Fundamental analysis on a thermocell with a mixture of the soluble redox couple aqueous potassium ferrocyanide and potassium ferricyanide solution, J. Electroanal. Chem., 296 (1990) 19-36.

[285]. M. P. Allen, Introductionto molecular dynamics simulation published in Computational Soft Matter: From synthetic polymers to proteins, Lecture Notes, Norbert Attig, Kurt Binder,Helmut Grubmüller, Kurt Kremer (Eds.), John von Neumann Institute for Computing, J ¨ ulich, NIC Series, ISBN 3-00-012641-4, 2004, Vol.23, pp. 1-28.

[286]. A.Z. Weber, J. Newman, Transport in polymer-electrolyte membranes I. physical model, J. Electrochem. Soc., 150 (2003) A1008-A1015.

[287]. A. Z. Weber, J. Newman, Transport in polymer-electrolyte membranes II. mathematical model, J. Electrochem. Soc., 151 (2004) A311-A325.

[288]. X. Cheng, J. Zhang, Y. Tang, C. Song, J. Shen, D. Song, J. Zhang, Hydrogen crossover in high-temperature PEM fuel cells, J. Power Sources, 167 (2007) 25-31.

[289]. R.F. Mann, J.C. Amphlett, B.A. Peppley, C.P. Thurgood, Henry's Law and the solubilities of reactant gases in the modeling of PEM fuel cells, J. Power Sources, 161 (2006) 768-774.

[290]. M. Secanell, K. Karan, A. Suleman, N. Djilali, Multi-variable optimization of PEMFC cathodes using an agglomerate model, Electrochimica Acta, 52 (2007) 6318-6337.

[291]. X. Zhou, Degradation of Pt catalysts in PEFCs: A new perspective from molecular dynamic modeling, Electrochem. Solid-State Lett., 11 (2008) B59-B62.

[292]. Y. Wang, P. B. Balbuena, Roles of proton and electric field in the electroreduction of O_2 on Pt (111) surfaces: results of an *ab-initio* molecular dynamics study, J. Phys. Chem. B, 108 (2004) 4376-4384.

[293]. A. B. Anderson, Y. Cai, R. A. Sidik, D. B. Kang, Advancements in the local reaction center electron transfer theory and the transition state structure in the first step of oxygen reduction over platinum, J. Electroanal. Chem., 580 (2005) 17-22.

[294]. J. Xu, J. T. Yates, Terrace width effect on adsorbate vibrations: a comparison of Pt(335) and Pt(112) for chemisorption of CO, Surf. Sci., 327 (1995) 193-201.

[295]. R. R. Nazmutdinov, D. V. Glukhov, O.A. Petrii, G. A. Tsirlina, G. N. Botukhova, Contemporary understanding of the peroxodisulfate reduction at a mercury electrode, J. Electroanal. Chem., 552 (2003) 261-278.

[296]. Y. Wang, Y. Ye, K. Wu, Simultaneous observation of the triangular and honeycomb structures on highly oriented pyrolytic graphite at room temperature: An STM study, Surf. Sci., 600 (2006) 729-734.

[297]. H.-L. Sun, Q.-T. Shen, J.-F. Jia, Q.-Z. Zhang, Q.-K. Xue, Scanning tunneling microscopy study of superlattice domain boundaries on graphite surface, Surf. Sci., 542 (2003) 94-100.

[298]. S.L. Tang, A.J. McGie, A. Suna, Molecular-resolution imaging of insulating macromolecules with the scanning tunneling microscope via anon-tunneling, electric-field-induced mechanism, Phys. Rev. B, 47 (1993) 3850-3856.

[299]. S.M. Lindsay, O.F. Sankey, Y. Li, C. Herbst, Pressure and resonance effect in scanning tunneling micrscopy of molecular adsorbates, J. Phys. Chem., 94 (1990) 4655-4660.

[300]. J-Y. Yuan, Z. Shao, and C. Gao, Alternative method of imaging surface topologies of nonconducting bulk specimen by scanning tunneling microscopy, Phys. Rev. Lett., 67(7) (1991) 863-866.

[301]. K. Mautitz, R. Moore, State of understanding of Nafion, Chem. Rev., 104 (2004) 4535-4585.

[302]. M. Ludvigsson, J. Lindgren, J. Tegenfeldt, Crystallinity in cast Nafion, J. Electrochem. Soc., 147 (2000) 1303-1305.

[303]. D.L. Wood III, J. Chlistunoff, J. Majewski, R.L. Borup, Nafion structural phenomena at platinum and carbon interfaces, J. Am. Chem. Soc., 131 (2009) 18096-18104.

[304]. I. Kendrick, D. Kumari, A. Yakaboski, N. Dimakis, E.S. Smotkin, Elucidating the ionomer-electrified metal interface, J. Am. Chem. Soc., 132 (2010) 17611-17616.

[305]. Jyotirmayee Nanda,, P.K. Mahapatra, C.L. Roy, Transmission coefficient, resonant tunneling lifetime and traversal time in multibarrier semiconductor heterostructure, Physica B 383 (2006) 232-242.

[306]. M. Ohmukai, Triangular double barrier resonant tunneling, Mater. Sci. Eng. B, 116 (2005) 87-90.

[307]. J. Halbritter, On surface states at superconductor oxide interfaces, Solid State Commun., 34 (1980) 675-678.

[308]. J. Halbritter, On resonant tunnelling, Surface Science 122 (1982) 80-98.

Publication List

1. Juanjuan Zhou, Yijing Yin, Xiangyang Zhou, Azzam N. Mansour, Experimental Studies of Mediator-Enhanced Polymer Electrolyte Supercapacitors, Electrochemical & Solid-state Letters, 14 (2010) A25-A28.
2. Juanjuan Zhou (Corresponding author), Jinshu Cai, Sirui Cai, Xiangyang Zhou, Azzam N. Mansour, Development of all-solid-state mediator enhanced supercapacitors with a PVDF/LiTFS separator, Journal of Power Sources, 196 (2011) 10479-10483.
3. Yijing Yin, Juanjuan Zhou, Azzam N. Mansour, Xiangyang Zhou, Effect of NaI/I_2 mediators on properties of $PEO/LiAlO_2$ based all-solid-state supercapacitors, Journal of Power Sources, 196 (2011) 5997-6002.
4. Xiangyang Zhou, Yijing Yin, Zedong Wang, Juanjuan Zhou, Hao Huang, Azzam N. Mansour, James A. Zaykoski, Jeffery, J. Fedderly, Edward Balizer. "Effect of Hot Pressing on the Ionic Conductivity of the PEO/Li CF_3SO_3 based Electrolyte Membranes.", Solid State Ionics, 196 (2011) 18-24.
5. Xiangyang Zhou, Juanjuan Zhou, and Yijing Yin. "Atomistic Modeling in Study of Polymer Electrolyte Fuel Cells: A Review." Modern Aspects of Electrochemistry: Modeling and Diagnostics of Polymer Electrolyte Fuel Cells. Springer Publisher, Vol. 9.
6. Xiangyang Zhou, Juanjuan Zhou, Yijing Yin, and Azzam Mansour, "Development and Study of Mediator-Enhanced Polymer Electrolyte Supercapacitors", ECS Trans. 19 (30) (2009) 9.
7. Yijing Yin, Juanjuan Zhou, and Xiangyang Zhou, "Preparation and Characterization of Mediator Doped $PEO/LiAlO_2/SiO_2$ Solid Polymer Electrolyte", ECS Trans. 19 (30) (2009) 1.
8. Xiangyang Zhou, Juanjuan Zhou, Zedong Wang, Dwayne McDaniel, Weihua Zhang, and Richard Burton, "Identification and Validation of Analytical Chemistry Methods for Detecting Composite Surface Contamination and Moisture - Solid-State Electrochemical Sensor Study", ECS Trans. 19 (22) (2009) 7.
9. Juanjuan Zhou, Xiangyang Zhou, Hongtan Liu, Hybrid Atomistic Modeling of the Interface between Pt catalysts and Nafion Electrolyte, 218th ECS Meeting (2011)
10. Xiangyang Zhou, Juanjuan Zhou, Yijing Yin, Zedong Wang, Hao Huang, Azzam N. Mansour, Mediator Enhanced All-solid-state Supercapacitors, 218th ECS Meeting (2011)
11. Xiangyang Zhou, Juanjuan Zhou, Yijing Yin, Zedong Wang, Hao Huang, Azzam N. Mansour, Mediator-Enhanced Polymer Electrolyte Supercapacitors (MEPESCs), 44th Power Source Conference. June 14 –June 17, (2010), Las Vegas, NV.